NASA/CR—2001-210713

Linearized Unsteady Aerodynamic Analysis of the Acoustic Response to Wake/Blade-Row Interaction

Joseph M. Verdon
Pratt & Whitney, East Hartford, Connecticut

January 2001

The NASA STI Program Office . . . in Profile

Since its founding, NASA has been dedicated to the advancement of aeronautics and space science. The NASA Scientific and Technical Information (STI) Program Office plays a key part in helping NASA maintain this important role.

The NASA STI Program Office is operated by Langley Research Center, the Lead Center for NASA's scientific and technical information. The NASA STI Program Office provides access to the NASA STI Database, the largest collection of aeronautical and space science STI in the world. The Program Office is also NASA's institutional mechanism for disseminating the results of its research and development activities. These results are published by NASA in the NASA STI Report Series, which includes the following report types:

- TECHNICAL PUBLICATION. Reports of completed research or a major significant phase of research that present the results of NASA programs and include extensive data or theoretical analysis. Includes compilations of significant scientific and technical data and information deemed to be of continuing reference value. NASA's counterpart of peer-reviewed formal professional papers but has less stringent limitations on manuscript length and extent of graphic presentations.

- TECHNICAL MEMORANDUM. Scientific and technical findings that are preliminary or of specialized interest, e.g., quick release reports, working papers, and bibliographies that contain minimal annotation. Does not contain extensive analysis.

- CONTRACTOR REPORT. Scientific and technical findings by NASA-sponsored contractors and grantees.

- CONFERENCE PUBLICATION. Collected papers from scientific and technical conferences, symposia, seminars, or other meetings sponsored or cosponsored by NASA.

- SPECIAL PUBLICATION. Scientific, technical, or historical information from NASA programs, projects, and missions, often concerned with subjects having substantial public interest.

- TECHNICAL TRANSLATION. English-language translations of foreign scientific and technical material pertinent to NASA's mission.

Specialized services that complement the STI Program Office's diverse offerings include creating custom thesauri, building customized data bases, organizing and publishing research results . . . even providing videos.

For more information about the NASA STI Program Office, see the following:

- Access the NASA STI Program Home Page at ***http://www.sti.nasa.gov***

- E-mail your question via the Internet to help@sti.nasa.gov

- Fax your question to the NASA Access Help Desk at 301–621–0134

- Telephone the NASA Access Help Desk at 301–621–0390

- Write to:
  NASA Access Help Desk
  NASA Center for AeroSpace Information
  7121 Standard Drive
  Hanover, MD 21076

NASA/CR—2001-210713

Linearized Unsteady Aerodynamic Analysis of the Acoustic Response to Wake/Blade-Row Interaction

Joseph M. Verdon
Pratt & Whitney, East Hartford, Connecticut

Prepared under Contract NAS3–27727, Task Order 13, Subtask 3

National Aeronautics and
Space Administration

Glenn Research Center

January 2001

Acknowledgments

The author gratefully acknowledges the advice and assistance provided by D.L. Huff (NASA Program Manager) during the course of this effort. He is also indebted to: G. Podboy and L.J. Heidelberg (NASA Glenn) for providing rotor-exit flow and FEGV acoustic response data; E. Envia (NASA Glenn) for reviewing a preliminary version of this report; R.J. Neubert and D.A. Topol (Pratt & Whitney) for providing FEGV geometry and wake excitation computer files; and D.E. Edwards (Pratt & Whitney) for developing animations of the LINFLUX solutions.

Available from

NASA Center for Aerospace Information
7121 Standard Drive
Hanover, MD 21076
Price Code: A05

National Technical Information Service
5285 Port Royal Road
Springfield, VA 22100
Price Code: A05

Available electronically at http://gltrs.grc.nasa.gov/GLTRS

Linearized Unsteady Aerodynamic Analysis of the Acoustic Response to Wake/Blade-Row Interaction

Contents

Linearized Unsteady Aerodynamic Analysis of the Acoustic Response to Wake/Blade-Row Interaction

Joseph M. Verdon
Pratt & Whitney
400 Main Street
East Hartford, Connecticut 06108

Summary

The three-dimensional, linearized Euler analysis, LINFLUX, is being developed to provide a comprehensive and efficient unsteady aerodynamic scheme for predicting the aeroacoustic and aeroelastic responses of axial-flow turbomachinery blading. LINFLUX couples a near-field, implicit, wave-split, finite-volume solution to far-field acoustic eigensolutions, to predict the aerodynamic responses of a blade row to prescribed structural and aerodynamic excitations. It is applied herein to predict the acoustic responses of a fan exit guide vane (FEGV) to rotor wake excitations. The intent is to demonstrate and assess the LINFLUX analysis via application to realistic wake/blade-row interactions. Numerical results are given for the unsteady pressure responses of the FEGV, including the modal pressure responses at inlet and exit. In addition, predictions for the modal and total acoustic power levels at the FEGV exit are compared with measurements. The present results indicate that the LINFLUX analysis should be useful in the aeroacoustic design process, and for understanding the three-dimensional flow physics relevant to blade-row noise generation and propagation.

1. Introduction

The development of analyses to predict unsteady flows in turbomachines is motivated primarily by the need to predict the aeroelastic and aeroacoustic response characteristics of the blading. Accurate and efficient analyses are needed to determine the unsteady loads that act on the blades and the unsteady pressures that persist upstream and downstream of the blade row, for various sources of excitation. The latter include prescribed structural motions and/or aerodynamic disturbances at inlet and exit that carry energy towards the blade row. The computational resources required by nonlinear and viscous unsteady fluid-dynamic analyses continue to prohibit their use in detailed aeroelastic and aeroacoustic response studies. Therefore, approximate, e.g., linearized inviscid, analyses are needed to achieve efficient predictions of unsteady aerodynamic response phenomena.

Much attention has been given in recent years to the development of three-dimensional (3D) linearized Euler analyses [HL93, HCL94, Sre96, MV97, MG98, MV98]. Such analyses account for the effects of nonuniform inlet and exit conditions, real blade geometry, steady blade loading, and transonic phenomena, on blade-row, unsteady aerodynamic response. In particular, the 3D LINFLUX analysis [MV97, MV98, VMC99] couples a near-field, implicit, finite-volume analysis for the unsteady perturbation of a general nonlinear mean flow in the near field, to analytic/numeric, far-field analyses for the unsteady perturbations of the mean flows, upstream and downstream, that depend only on radius. The near-field analysis is based upon the high-resolution, wave-split, finite-volume scheme [WJS88], employed in the time-dependent, nonlinear fluid-dynamic analysis, TURBO [Jan89, JHW92, CW93]. The far-field analyses, which are coupled to the near-field, finite-volume analysis at the near-field, computational inflow and outflow boundaries, allow incoming external aerodynamic excitations to be prescribed, and outgoing response disturbances to pass through the computational boundaries without reflection.

A two-dimensional (2D) version of the LINFLUX analysis is reported in [MV95, VMK95] along with numerical results for subsonic and transonic unsteady flows through the 10th Standard Cascade [FV93]. Comparisons of the 2D LINFLUX results with those of the potential-based linearization, LINFLO [VC84, UV91, HV91], and the nonlinear Euler/Navier-Stokes analysis, NPHASE [HSR91, SLH+94], indicate that the former gives accurate response information for the various types of unsteady excitation.

The three-dimensional LINFLUX analysis is reported in [MV97, MV98, VMC99], and partially validated via result comparisons, with well-known 2D analyses, for benchmark unsteady flows. In particular, subsonic unsteady flows through a helical fan and a three-dimensional version of the 10th Standard Cascade (3D SC10), excited by prescribed blade motions, acoustic disturbances at inlet and exit, and vortical disturbances at inlet, have been studied. The helical fan and the 3D SC10 have high hub to tip ratios, and were subjected to highly two-dimensional unsteady excitations at low through moderate frequencies. Thus, the 3D LINFLUX results could be compared meaningfully with those of the 2D classical analysis of Smith [Smi72] for the helical fan, and those of the 2D LINFLO analysis for the 3D SC10. The LINFLUX pressure responses, at midspan, are in very good agreement with those of the earlier 2D analyses. Moreover, these responses show reasonable radial trends, and the amplitudes and axial eigenvalues of the propagating and/or least-damped modal acoustic responses in the far field are accurately predicted. More recently [PV00], LINFLUX results

for a standard computational aeroacoustics (CAA) configuration [Han99]; i.e., a flat-plate stator, with a hub-to-tip ratio of 0.5, excited by vortical excitations at inlet, were found to be in excellent agreement with the results of Namba's [Nam87] 3D classical linearized analysis.

The 3D LINFLUX analysis is being developed to serve as the unsteady aerodynamic component of an advanced design prediction system for fan noise. A fundamental source of such noise is the interaction between the wakes coming off the upstream rotor, or more generally, between the circumferential nonuniformities in the rotor exit flow, with the downstream fan exit guide vane (FEGV). Current aeroacoustic design systems rely on unsteady aerodynamic analyses that are based on classical linearized theory, either 3D analyses or 2D analyses applied on radial strips. Classical analyses do not account for many of the important features of real flows. For example, the only stator configuration that can be addressed by a classical 3D analysis is one in which the stator consists of flat-plate blades that are aligned with a uniform mean or steady inlet flow. Because of such limitations, the unsteady aerodynamic element has been regarded as the weakest component in current design systems for predicting fan-noise generation and propagation.

The LINFLUX analysis is being developed to overcome the limitations inherent to classical linearized theory. In the present effort, we have applied this analysis to a realistic fan configuration to demonstrate and assess its capabilities for aeroacoustic design applications. We consider unsteady flows through the fan exit guide vane (FEGV) of a NASA/PW 22 inch advanced ducted propulsor (ADP) [Neu97, Pod97], operating at low (approach) and high (take-off) power settings. The unsteady flows through the FEGV are excited by circumferential nonuniformities in the flow exiting the fan rotor, which are due primarily to the viscous wakes extending downstream from the rotor blades. The analytic wake excitation is based on measurements, taken downstream of the fan rotor, at NASA Glenn Research Center [Pod97]. A number of physical assumptions have also been introduced to provide an analytic wake excitation that is suitable for use with LINFLUX. LINFLUX is then applied to predict the unsteady aerodynamic responses of the FEGV to Fourier components, at multiples of the blade passing frequency (BPF), of the rotor wake excitations.

It should be noted that the application of LINFLUX to predict the unsteady aerodynamic response of a blade row to a wake excitation involves the use four major computer codes: TIGER [SS91], to generate a 3D H-grid; AWAKEN [TE99, Top00], to define analytic steady and unsteady inflow conditions based on measured or computed wake data; TURBO [Jan89, JHW92, CW93], to determine the steady background flow; and LINFLUX to determine the linearized unsteady flow. We will refer to this set of codes as the LINFLUX Prediction System, and provide instructions for running this system in [Ver00].

In this report, we describe the general unsteady aerodynamic problem for a blade row; the linearized unsteady aerodynamic equations, and the near- and far-field solution procedures that form the basis of the LINFLUX analysis; and the current wake-excitation model. We then proceed to give a detailed description of the application of LINFLUX to predict the rotor-wake/FEGV interactions in the NASA/PW 22 inch ADP. We will present numerical results for the steady and unsteady pressures and the unsteady velocity in the near field of the FEGV, and for the modal acoustic responses in the far field. Predicted results for the modal and total sound power levels at the FEGV exit will be compared with experimental measurements [Hei99].

2. Unsteady Flow through a Blade Row

We consider the general situation of time-dependent flow, of an inviscid perfect gas through a vibrating, rotor or stator, blade row (see Figure 1). The latter consists of N blades, which, in the case of a rotor, rotate about the duct axis at constant angular velocity $\mathbf{\Omega} = \Omega \mathbf{e}_\xi$, and operates within a stationary annular duct with hub and duct, or tip, radii of $r = r_H$ and $r = r_D$, respectively. In the absence of a vibratory motion, the blades are identical in shape, equally spaced around the rotor, and identical in orientation relative to an axisymmetric inlet flow.

We will analyze this flow in a reference frame that is fixed to the blade row, in terms of cylindrical $(r,\ \theta,\ \xi,\ t)$ and Cartesian $(x_1, x_2, x_3, t) = (\xi,\ r\sin\theta,\ -r\cos\theta, t)$ coordinates. Here ξ and r measure distance in the axial flow direction and radially outward from the duct axis, respectively, θ measures angular distance in the $\mathbf{e}_\xi \times \mathbf{e}_r = \mathbf{e}_\theta$ direction, which, for a rotor, is opposite to the direction of blade rotation, and $\mathbf{e}$ is a unit vector. We will also have occasion to examine a rotor flow in the stator or absolute frame, and a stator flow in the rotor or relative frame. Thus, when needed for clarity, we will use the superscripts abs or rel to indicate that a physical quantity is measured relative to a stationary or a rotating reference frame, respectively. Thus, for example, $\theta^{\text{abs}} = \theta^{\text{rel}} + \Omega t$.

To describe flows in which the fluid domain deforms with time, it is useful to consider two sets of independent variables, say $(\mathbf{x}, t)$ and $(\bar{\mathbf{x}}, t)$. The position vector $\mathbf{x}(\bar{\mathbf{x}}, t) = \bar{\mathbf{x}} + \boldsymbol{\mathcal{R}}(\bar{\mathbf{x}}, t)$ describes the instantaneous location, in the blade row frame of reference, of a moving field point, $\bar{\mathbf{x}}$ refers to the reference or mean position of this point, and $\boldsymbol{\mathcal{R}}(\bar{\mathbf{x}}, t)$ is the displacement of the point from its reference position. The displacement field, $\boldsymbol{\mathcal{R}}$, is prescribed so that the solution domain deforms with the vibratory motions of the blades and is rigid far from the blade row. If the blades do not vibrate, $\boldsymbol{\mathcal{R}}$ is simply set equal to zero.

In the present report, physical variables are, for the most part, given in dimensionless form. Lengths are scaled with respect to the reference length L^*_{Ref}, time with respect to the ratio $L^*_{\text{Ref}}/V^*_{\text{Ref}}$ where V^*_{Ref} is the reference flow speed, velocity with respect to V^*_{Ref}, density with respect to a reference density $\bar{\rho}^*_{\text{Ref}}$, pressure with respect to $\bar{\rho}^*_{\text{Ref}}(V^*_{\text{Ref}})^2$ and specific internal energy with respect to $(V^*_{\text{Ref}})^2$. Here, the superscript $*$ refers to a dimensional value of a flow variable. In LINFLUX, the reference length is taken to be the blade chord at midspan; the reference fluid density and flow speed, to be the inlet, temporally- and circumferentially-averaged density and relative (to the blade row) flow speed, at midspan, respectively.

For aeroelastic and aeroacoustic applications, we are usually interested in a restricted class of unsteady flows; those in which the unsteady fluctuations can be regarded as perturbations of a background flow that is steady in a reference frame that rotates with the blade row. Moreover, the steady background flows far upstream ($\xi \le \xi_-$) and far downstream ($\xi \ge \xi_+$) from the blade row can be assumed to consist of at most small steady perturbations from steady flows that depend only on radius. The time-dependent or unsteady fluctuations in these flows arise from temporally and circumferentially periodic unsteady excitations of small-amplitude, i.e., prescribed vibratory blade motions and prescribed aerodynamic disturbances at inlet and exit that travel towards the blade row.

For example, if the blades vibrate at reduced frequency, ω, as seen by an observer in the blade-row frame, and at constant interblade phase angle, σ, we can write

$$\mathcal{R}_{\mathrm{B}_n}(\bar{r}, \bar{\theta} + 2\pi n/N, \bar{\xi}, t) = \mathbf{T}_n Re\{\mathbf{R}_{\mathrm{B}}(\bar{r}, \bar{\theta}, \bar{\xi}) \exp[i(\omega t + n\sigma)]\}, \ \bar{\mathbf{x}} \text{ on } B \ . \qquad (2.1)$$

Here, $\mathcal{R}_{\mathrm{B}_n}$ is the displacement of a point on the nth moving blade surface from its mean position in the rotating frame; $\mathbf{T}_n$ is a rotation matrix, which relates a vector in the reference ($n = 0$) passage to its counterpart in the nth passage; $n = 0, 1, 2, \ldots, N-1$ is a blade index; $Re\{\ \}$ denotes the real part of $\{\ \}$; $\mathbf{R}_{\mathrm{B}}$ is the complex amplitude of the reference ($n = 0$) blade displacement; and B refers to the mean position of the reference blade. The interblade phase angle, σ, can be determined from the nodal diameter pattern of the unsteady disturbance. Thus, for the vibratory blade motion, described in equation (2.1), $\sigma = 2\pi N_{\mathrm{D}}/N$, where $|N_{\mathrm{D}}|$, is the number of nodal diameters, i.e., the the number of times the vibratory disturbance repeats around the wheel. The sign of N_{D} depends on the direction of rotation of the disturbance pattern. If the vibratory disturbance travels in the negative θ-direction, $N_{\mathrm{D}} > 0$. Thus, for a rotor, if the vibratory disturbance travels in the direction of blade rotation, $N_D > 0$.

The unsteady disturbances in the far upstream and far downstream regions are, in part, prescribed as a fluid dynamic excitation and, in part, depend upon the interaction between the fluid and the blading. Typically, an unsteady aerodynamic excitation is represented as a linear combination of fundamental disturbances. The fundamental disturbances are harmonic in time, at temporal frequency ω, and circumferentially, at angular wave number $\bar{m} = N_{\mathrm{D}} + mN \ , \ m = 0, \pm 1, \pm 2, \ldots \ .$ For example, if the underlying absolute mean or steady flow is uniform, the pressure associated with a fundamental acoustic excitation is of the form

$$\tilde{p}_{\mathrm{A}}^{\pm}(r, \theta, \xi, t) = Re\{a^{\pm} p^{\mathrm{R},\pm}(r) \exp[\chi^{\pm}\xi + i(\bar{m}\theta + \omega t)]\}, \quad \xi \lesseqgtr \xi_{\mp} \ . \qquad (2.2)$$

Here, $\tilde{p}_{\mathrm{A}}^{\pm}(\mathbf{x}, t)$ describes an incident pressure disturbance, i.e., a pressure disturbance that travels towards the blade row from far upstream ($\xi \leq \xi_-$) or far downstream ($\xi \geq \xi_+$). The quantities ω, $\bar{m} = N_{\mathrm{D}} + mN$ or $\sigma_m = 2\pi(N_D/N + m)$, and the disturbance amplitude, $a^{\pm}$, are prescribed; the radial mode shape, $p^{\mathrm{R},\pm}(r)$, and the axial exponential coefficient $\chi^{\pm} = \beta^{\pm} + i\kappa_{\xi}^{\pm}$, where β is the axial attenuation coefficient and κ_{ξ} is the axial wave number, are determined from the equations that govern the unsteady fluid motion in the far field.

3. Unsteady Aerodynamic Model

Nonlinear field equations that govern the unsteady flows, described in §2, are derived from the mass, momentum and energy conservation laws for inviscid flow and the thermodynamic relations for a perfect gas. These equations, when referenced to a coordinate frame that rotates with the blade row, at constant angular velocity $\mathbf{\Omega}$, can be written in integral form as

$$\frac{d}{dt}\int_{\mathcal{V}} \tilde{\mathbf{U}} d\mathcal{V} + \int_{\mathcal{A}} [\tilde{\mathbf{F}}_{x_j} - \tilde{\mathbf{U}}\dot{\mathcal{R}}_{x_j}] n_{x_j} d\mathcal{A} = \int_{\mathcal{V}} \tilde{\mathbf{S}} d\mathcal{V} \ . \tag{3.1}$$

Here, the symbol $\tilde{}$ indicates a time-dependent flow quantity, and $\mathcal{V}(t)$ is an arbitrary moving control volume, which is bounded by the control surface $\mathcal{A}(\mathbf{x}, t) = 0$. Also, $\dot{\boldsymbol{\mathcal{R}}}(\bar{\mathbf{x}}, t) = (\dot{\mathcal{R}}_{x_1}, \dot{\mathcal{R}}_{x_2}, \dot{\mathcal{R}}_{x_3})$ is the prescribed velocity of the moving field point at $\mathbf{x} = \bar{\mathbf{x}} + \boldsymbol{\mathcal{R}}(\bar{\mathbf{x}}, t)$, $\mathbf{n}$ is a unit vector normal to the surface, $\mathcal{A}$, and pointing outward from $\mathcal{V}$, and a summation over repeated indices is implied. The source term on the right-hand-side of (3.1) accounts for the rotation of the reference coordinate frame.

The state, $\tilde{\mathbf{U}}$, flux, $\tilde{\mathbf{F}}_{x_j}, j = 1, 2, 3$, and source term, $\tilde{\mathbf{S}}$, vectors in equation (3.1) are given by

$$\tilde{\mathbf{U}} = \begin{bmatrix} \tilde{\bar{\rho}} \\ \tilde{\bar{\rho}}\tilde{V}_{x_1} \\ \tilde{\bar{\rho}}\tilde{V}_{x_2} \\ \tilde{\bar{\rho}}\tilde{V}_{x_3} \\ \tilde{\bar{\rho}}\tilde{E}_T \end{bmatrix} \ , \ \tilde{\mathbf{F}}_{x_j}(\tilde{\mathbf{U}}) = \begin{bmatrix} \tilde{U}_{j+1} \\ \tilde{U}_{j+1}\tilde{U}_2/\tilde{U}_1 + \tilde{P}\delta_{1j} \\ \tilde{U}_{j+1}\tilde{U}_3/\tilde{U}_1 + \tilde{P}\delta_{2j} \\ \tilde{U}_{j+1}\tilde{U}_4/\tilde{U}_1 + \tilde{P}\delta_{3j} \\ \tilde{U}_{j+1}(\tilde{U}_5 + \tilde{P})/\tilde{U}_1 \end{bmatrix} \ , \ \tilde{\mathbf{S}}(\tilde{\mathbf{U}}, \mathbf{x}) = \begin{bmatrix} 0 \\ 0 \\ \Omega^2\tilde{U}_1 x_2 + 2\Omega\tilde{U}_4 \\ \Omega^2\tilde{U}_1 x_3 - 2\Omega\tilde{U}_3 \\ \Omega^2(\tilde{U}_3 x_2 + U_4 x_3) \end{bmatrix} . \tag{3.2}$$

Here, $\tilde{\bar{\rho}}$, $\tilde{\mathbf{V}}$, $\tilde{E}_T = \tilde{E} + \tilde{V}^2/2$ and $\tilde{P} = (\gamma - 1)\tilde{\bar{\rho}}\tilde{E} = (\gamma - 1)[\tilde{U}_5 - \tilde{U}_1^{-1}(\tilde{U}_2^2 + \tilde{U}_3^2 + \tilde{U}_4^2)/2]$ are the time-dependent fluid density, velocity, specific total internal energy, and pressure, respectively. The velocity and total internal energy are measured relative to the blade-row frame of reference.

We also require a differential form of the field equation (3.1), which applies at fixed locations ($\boldsymbol{\mathcal{R}} \equiv \mathbf{0}$) in the blade-row frame, to describe the unsteady flows far upstream ($\xi < \xi_-$) and far downstream ($\xi > \xi_+$) of the blade row. Expressed in terms of cylindrical coordinates, this equation has the form

$$\left.\frac{\partial \tilde{\mathbf{U}}^{\text{cyl}}}{\partial t}\right|_{\mathbf{x}} + r^{-1}\frac{\partial r\tilde{\mathbf{F}}_r}{\partial r} + r^{-1}\frac{\partial \tilde{\mathbf{F}}_\theta}{\partial \theta} + \frac{\partial \tilde{\mathbf{F}}_\xi}{\partial \xi} = \tilde{\mathbf{S}} \ . \tag{3.3}$$

The state and source-term vectors in (3.3) are given by

$$\tilde{\mathbf{U}}^{\text{cyl}} = \begin{Bmatrix} \tilde{\bar{\rho}} \\ \tilde{\bar{\rho}}\tilde{V}_r \\ \tilde{\bar{\rho}}\tilde{V}_\theta \\ \tilde{\bar{\rho}}\tilde{V}_\xi \\ \tilde{\bar{\rho}}\tilde{E}_T \end{Bmatrix} , \quad \tilde{\mathbf{S}} = r^{-1}\begin{Bmatrix} 0 \\ (\tilde{U}_3^{\text{cyl}})^2/\tilde{U}_1^{\text{cyl}} + \tilde{P} \\ -\tilde{U}_2^{\text{cyl}}\tilde{U}_3^{\text{cyl}}/\tilde{U}_1^{\text{cyl}} \\ 0 \\ 0 \end{Bmatrix} + \Omega\begin{Bmatrix} 0 \\ 2\tilde{U}_3^{\text{cyl}} + \tilde{U}_1^{\text{cyl}}\Omega r \\ -2\tilde{U}_2^{\text{cyl}} \\ 0 \\ \tilde{U}_2^{\text{cyl}}\Omega r \end{Bmatrix} . \tag{3.4}$$

The flux vectors $\tilde{\mathbf{F}}_r(\tilde{\mathbf{U}}^{\rm cyl})$, $\tilde{\mathbf{F}}_\theta(\tilde{\mathbf{U}}^{\rm cyl})$ and $\tilde{\mathbf{F}}_\xi(\tilde{\mathbf{U}}^{\rm cyl})$ and the pressure $P(\tilde{\mathbf{U}}^{\rm cyl})$ have functional forms similar to those indicated previously for $\tilde{\mathbf{F}}_{x_j}(\tilde{\mathbf{U}})$, $j = 1, 2, 3$, and $\tilde{P}(\tilde{\mathbf{U}})$.

The foregoing field equations must be supplemented by conditions on the unsteady flow at the blade surfaces, the duct walls, and the inflow ($\xi = \xi_-$) and outflow ($\xi = \xi_+$) boundaries of a near-field computational domain. Flow tangency conditions, i.e.,

$$(\tilde{\mathbf{V}} - \dot{\boldsymbol{\mathcal{R}}}) \cdot \mathbf{n} = 0 \quad \text{for} \quad \mathbf{x} \in \mathcal{B}_n \,, \quad r = r_H \quad \text{and} \quad r = r_D \,, \tag{3.5}$$

apply at the moving blade surfaces, $\mathcal{B}_n$, and at the stationary ($\dot{\boldsymbol{\mathcal{R}}} \equiv \mathbf{0}$) duct walls. In addition, temporally- and circumferentially-averaged values of the total pressure, the total temperature and the inlet flow angle are specified as functions of radius at the computational inflow boundary, and the circumferentially- and temporally-averaged static pressure is specified at the outflow boundary, consistent with radial equilibrium. Unsteady departures from these averaged flow conditions at inlet and exit that carry energy towards the blade row must be specified; those that carry energy away from the blade row must be determined as part of the solution for the unsteady flow.

3.1 Linearized Unsteady Aerodynamic Equations

Since the unsteady excitations are assumed to be of small amplitude (e.g., $|\boldsymbol{\mathcal{R}}_{B_n}| \sim \mathcal{O}(\epsilon) << 1$) and to occur at a single temporal frequency, ω, the unsteady component of the inviscid flow can be approximated as a first-order (in ϵ), or linear, harmonic perturbation of an underlying zeroth-order, nonlinear, background flow. The background flow is steady in the blade-row frame. This approximation offers several computational advantages. First, since the first-order unsteady flow properties have harmonic time-dependence, physical time dependence, can be removed from the resulting unsteady boundary-value problem. Second, as a consequence of our assumptions regarding rotor geometry, the inlet and exit mean-flow conditions, and the circumferential behaviors of the unsteady excitations, numerical resolutions of the steady and linearized unsteady flows can be limited to a single, extended, blade-passage region; i.e., a region of angular pitch $\Delta\theta = 2\pi/N$. Finally, the steady flows far from the blade row, depend only on radius. Therefore, approximate representations of the unsteady perturbations in the far field can be constructed, and matched to a computational near-field solution, to limit the axial extent of the near-field, computational domain.

To determine the zeroth- and first-order aerodynamic equations, we expand the unsteady state vector, $\tilde{\mathbf{U}}$, into an asymptotic series of the form [HC93]

$$\tilde{\mathbf{U}}[\mathbf{x}(\bar{\mathbf{x}}, t), t] = \mathbf{U}(\bar{\mathbf{x}}) + \tilde{\mathbf{u}}[\mathbf{x}(\bar{\mathbf{x}}, t), t] + \ldots = \mathbf{U}(\bar{\mathbf{x}}) + Re\{\mathbf{u}(\bar{\mathbf{x}}) \exp(i\omega t)\} + \ldots \,. \tag{3.6}$$

The column vectors $\mathbf{U}(\bar{\mathbf{x}})$ and $\tilde{\mathbf{u}}[\mathbf{x}(\bar{\mathbf{x}}, t), t]$ contain the conservation variables for the steady background flow at the mean position, $\bar{\mathbf{x}}$, of a moving field point and the first-order unsteady flow at the instantaneous position, $\mathbf{x} = \bar{\mathbf{x}} + \boldsymbol{\mathcal{R}}(\bar{\mathbf{x}}, t) = \bar{\mathbf{x}} + \mathrm{Re}\{\mathbf{R}(\bar{\mathbf{x}}) \exp(i\omega t)\}$, of this point, respectively. The components of the vector $\mathbf{u}$ are the complex amplitudes of the first-order unsteady conservation variables, i.e., $\mathbf{u}^T = [\rho \,,\, \bar{\rho} v_{x_1} + \rho V_{x_1} \,,\, \bar{\rho} v_{x_2} + \rho V_{x_2} \,,\, \bar{\rho} v_{x_3} + \rho V_{x_3} \,,\, \bar{\rho} e_T + \rho E_T]$ where $\bar{\rho}$, $\mathbf{V}$ and E_T and ρ, $\mathbf{v}$, and e_T are the steady and the complex amplitudes of the first-order, unsteady, primitive, flow variables. The unsteady flux $\tilde{\mathbf{F}}_{x_j}$ and source term,

$\tilde{\mathbf{S}}$, vectors are expanded into Taylor series about the mean flow state, $\mathbf{U}$, and the reference spatial location, $\bar{\mathbf{x}}$, i.e.,

$$\tilde{\mathbf{F}}_{x_j}(\tilde{\mathbf{U}}) = \mathbf{F}_{x_j}(\mathbf{U}) + \frac{\partial \mathbf{F}_{x_j}}{\partial \mathbf{U}}\tilde{\mathbf{u}} + \dots \quad \text{and} \quad \tilde{\mathbf{S}}(\tilde{\mathbf{U}}, \mathbf{x}) = \mathbf{S}(\mathbf{U}, \bar{\mathbf{x}}) + \frac{\partial \mathbf{S}}{\partial \mathbf{U}}\tilde{\mathbf{u}} + (\boldsymbol{\mathcal{R}} \cdot \boldsymbol{\nabla}_{\bar{\mathbf{x}}})\mathbf{S} + \dots . \tag{3.7}$$

The integral field equation (3.1) is expressed in terms of the moving control volume, $\mathcal{V}$, and the moving control surface, $\mathcal{A}$. The corresponding differential field equation would be expressed in terms of the moving spatial coordinate $\mathbf{x}$. However, because of the dependent variable expansion (3.6), it is more appropriate to express the steady and linearized unsteady equations in terms of the mean or steady-state quantities, $\bar{V}$, $\bar{A}$, and $\bar{\mathbf{x}}$. To within first-order in ϵ, the required spatial transformation relations are

$$d\mathcal{V} = (1 + \boldsymbol{\nabla}_{\bar{\mathbf{x}}} \cdot \boldsymbol{\mathcal{R}}) d\bar{V} + \dots , \quad \mathbf{n} d\mathcal{A} = \bar{\mathbf{n}} d\bar{A} + \Delta(\bar{\mathbf{n}} d\bar{A}) \exp(i\omega t) + \dots ,$$
and
$$\partial / \partial x_j = \partial / \partial \bar{x}_j - (\partial \mathcal{R}_{x_m} / \partial \bar{x}_j) \partial / \partial \bar{x}_m + \dots , \tag{3.8}$$

where $(\boldsymbol{\nabla}_{\bar{\mathbf{x}}} \cdot \boldsymbol{\mathcal{R}}) = \partial \mathcal{R}_m / \partial \bar{x}_m$, $\bar{\mathbf{n}}$ is the unit outward normal vector to the control surface $\bar{A}$, and $\Delta(\bar{\mathbf{n}} d\bar{A})$ is the complex amplitude of the first-harmonic component of $\mathbf{n} d\mathcal{A} - \bar{\mathbf{n}} d\bar{A}$. Finally, to within first order in ϵ, the temporal derivatives appearing in the nonlinear, time-dependent, integral and differential field equations transform according to

$$\frac{d}{dt}\int_{\bar{\mathcal{V}}}(\quad) d\mathcal{V} = \int_{\bar{V}} \left(\left.\frac{\partial(\quad)}{\partial t}\right|_{\bar{\mathbf{x}}} + (\quad)\boldsymbol{\nabla}_{\bar{\mathbf{x}}} \cdot \dot{\boldsymbol{\mathcal{R}}} \right) d\bar{V} + \dots \quad \text{and} \quad \left.\frac{\partial}{\partial t}\right|_{\mathbf{x}} = \left.\frac{\partial}{\partial t}\right|_{\bar{\mathbf{x}}} + \dot{\mathcal{R}}_{x_m} \frac{\partial}{\partial \bar{x}_m} + \dots . \tag{3.9}$$

The equations that govern the zeroth-order steady and the first-order unsteady flows are obtained by substituting the foregoing series expansions into the time-dependent, nonlinear, governing equations; equating terms of like power in ϵ; and neglecting terms of second and higher order in ϵ. This procedure leads to nonlinear and linear variable-coefficient equations, respectively, for the zeroth- and first-order flows.

The nonlinear, integral, field equation that governs the steady background flow is

$$\int_{\bar{A}} \mathbf{F}_{x_j} n_{x_j} d\bar{A} = \int_{\bar{V}} \mathbf{S} d\bar{V} . \tag{3.10}$$

In addition, the flow tangency conditions,

$$\mathbf{V} \cdot \mathbf{n} = 0 , \quad \text{for} \quad \bar{\mathbf{x}} \in B_n , \; r = r_H \text{ and } r = r_D \tag{3.11}$$

apply at the mean blade surfaces and the duct walls, and circumferential periodicity conditions; e.g.,

$$\bar{\rho}(\bar{r}, \bar{\theta} + 2\pi n/N, \bar{\xi}) = \bar{\rho}(\bar{r}, \bar{\theta}, \bar{\xi}) \quad \text{and} \quad \mathbf{V}(\bar{r}, \bar{\theta} + 2\pi n/N, \bar{\xi}) = \mathbf{T}_n \mathbf{V}(\bar{r}, \bar{\theta}, \bar{\xi}) \tag{3.12}$$

apply upstream and downstream of the blade row. Finally, circumferentially averaged values of the appropriate steady flow variables are specified as functions of radius at the inflow and outflow boundaries and circumferential harmonics of these variables are allowed to evolve to values that are consistent with a blade row operating within a long annular duct.

The linear equation that governs the first-harmonic unsteady perturbation is

$$i\omega\int_{\bar{V}}\mathbf{u}d\bar{V}+\int_{\bar{A}}\left(\frac{\partial\mathbf{F}_{x_j}}{\partial\mathbf{U}}\mathbf{u}\right)\bar{n}_{x_j}d\bar{A}-\int_{\bar{V}}\frac{\partial\mathbf{S}}{\partial\mathbf{U}}\mathbf{u}d\bar{V}=-\int_{\bar{V}}i\omega\left(\frac{\partial R_{x_m}}{\partial\bar{x}_m}\right)\mathbf{U}d\bar{V}$$
$$+\int_{\bar{A}}\left[i\omega R_{x_j}\mathbf{U}\bar{n}_{x_j}d\bar{A}-\mathbf{F}_{x_j}\Delta(\bar{\mathbf{n}}d\bar{A})\right]+\int_{\bar{V}}\frac{\partial}{\partial\bar{x}_j}(R_{x_j}\mathbf{S})d\bar{V}\ , \tag{3.13}$$

where the variable coefficients depend on the steady background flow, and the source terms depend upon this flow and the prescribed displacement field, $\mathbf{R}$.

Linearized flow tangency conditions, i.e.,

$$\mathbf{v}\cdot\bar{\mathbf{n}}=i\omega\mathbf{R}\cdot\bar{\mathbf{n}}+\mathbf{V}\cdot\boldsymbol{\nabla}(\mathbf{R}\cdot\bar{\mathbf{n}}),\ \text{for}\ \bar{\mathbf{x}}\in B_n\ ,\ r=r_H\ \text{and}\ r=r_D\ , \tag{3.14}$$

apply at the mean blade surfaces and at the duct walls, and phase-shifted, circumferential, periodicity conditions, e.g.,

$$\rho(\bar{r},\bar{\theta}+2\pi n/N\ ,\bar{\xi})=\rho(\bar{r},\bar{\theta},\bar{\xi})\quad\text{and}\quad\mathbf{v}(\bar{r},\bar{\theta}+2\pi n/N,\bar{\xi})=\mathbf{T}_n\mathbf{v}(\bar{r},\bar{\theta},\bar{\xi})\exp(in\sigma)\ , \tag{3.15}$$

apply upstream and downstream of the blade row. The far-field conditions imposed in the unsteady problem must allow for the prescription of external unsteady aerodynamic excitations and permit unsteady disturbances coming from within the solution domain to pass through the computational inlet (at $\xi=\xi_-$) and exit (at $\xi=\xi_+$) boundaries without reflection.

Differential field equations that describe the steady and the first-order unsteady flows at fixed points, $\mathbf{x}=\bar{\mathbf{x}}$, in the far upstream ($\xi<\xi_-$) or far downstream ($\xi>\xi_+$) regions, can be determined by applying the series expansions (3.6) and (3.7), with $\mathbf{R}\equiv\mathbf{0}$, to the nonlinear, time-dependent equation (3.3). We find that

$$r^{-1}\frac{\partial r\mathbf{F}_r}{\partial r}+r^{-1}\frac{\partial\mathbf{F}_\theta}{\partial\theta}+\frac{\partial\mathbf{F}_\xi}{\partial\xi}=\mathbf{S} \tag{3.16}$$

and

$$i\omega\mathbf{u}+r^{-1}\frac{\partial(r\mathbf{A}\mathbf{u})}{\partial r}+r^{-1}\frac{\partial\mathbf{B}\mathbf{u}}{\partial\theta}+\frac{\partial\mathbf{C}\mathbf{u}}{\partial\xi}-\mathbf{D}\mathbf{u}=0\ , \tag{3.17}$$

where $\mathbf{A}=\partial\mathbf{F}_r\ /\partial\mathbf{U}^{\text{cyl}}$, $\mathbf{B}=\partial\mathbf{F}_\theta\ /\partial\mathbf{U}^{\text{cyl}}$ and $\mathbf{C}=\partial\mathbf{F}_\xi\ /\partial\mathbf{U}^{\text{cyl}}$ are flux Jacobian matrices and $\mathbf{D}=\partial\mathbf{S}\ /\partial\mathbf{U}^{\text{cyl}}$ is the source-term Jacobian.

3.2 Solution Strategy

We require sequential solutions to the foregoing nonlinear steady and linear unsteady, boundary value problems, over a single, extended, blade-passage, solution domain, to predict the unsteady aerodynamic response of a blade row to a prescribed unsteady excitation. In the present study, we apply the nonlinear analysis, TURBO [JHW92], to determine the steady background flow, and then seek solutions to the linear unsteady problem by matching a wave-split, finite-volume analysis for the unsteady perturbation in the near field, i.e., in the region $\xi_-\le\xi\le\xi_+$, to approximate analytic/numeric descriptions of the unsteady perturbations

of the radially-dependent, steady background flows that exist in the regions far upstream ($\xi \leq \xi_-$) and far downstream ($\xi \geq \xi_+$) of the blade row.

For the near-field, finite-volume analysis, it is advantageous to regard the state vector $\mathbf{u}$ as pseudo time dependent, i.e., to set $\mathbf{u} = \mathbf{u}(\bar{\mathbf{x}}, \tau)$, where τ is the pseudo time variable, and add the term $\partial(\int_{\bar{V}} \mathbf{u} d\bar{V})/\partial\tau$ to the left-hand side of equation (3.13). This allows the use of a conventional time-marching algorithm to converge the solutions for the complex amplitudes of the first-order, unsteady, flow quantities, to constant values.

The complex amplitude of the displacement field, $\mathbf{R}(\bar{\mathbf{x}})$, must be prescribed over the entire solution domain. This field is defined so that the solution domain deforms with the blade motion (i.e., $\mathbf{R}(\bar{\mathbf{x}}) = \mathbf{R}_{\mathrm{B}_n}(\bar{\mathbf{x}})$ for $\bar{\mathbf{x}} \in \mathrm{B}_n$), slides along the hub and duct walls ($\mathbf{R}(\bar{\mathbf{x}}) \cdot \mathbf{e}_r = 0$ for $\bar{r} = r_H, r_D$), and remains rigid far from the blade row ($\mathbf{R}(\bar{\mathbf{x}}) \equiv \mathbf{0}$ for $\bar{\xi} \lesseqgtr \bar{\xi}_{\mp}$). In addition, $\mathbf{R}(\bar{\mathbf{x}})$ is prescribed along one blade-to-blade periodic boundary, and set at the other boundary, so as to satisfy phase-lagged periodicity, cf. (3.15). In the near field, $\mathbf{R}(\bar{\mathbf{x}})$ is determined, first, along the hub and duct walls, and then, in the interior of the computational domain as solutions of Laplace's equation, $\nabla^2_{\bar{\mathbf{x}}}\mathbf{R} = \mathbf{0}$, subject to the appropriate Dirichlet boundary conditions. For unsteady flows in which the blades are stationary in the blade-row frame, $\mathbf{R}$ is simply set equal to zero.

4. Near-Field Numerical Model

The numerical procedures used in LINFLUX to resolve the linearized unsteady flow in the near field, are based on those employed in the nonlinear analysis, TURBO [Jan89, JHW92, CW93]. Both analyses use a sheared H-mesh [SS91], which defines a curvilinear coordinate system, such that, there is a one-to-one correspondence between the points, $\bar{\mathbf{x}}$, in the physical domain and the points, $\boldsymbol{\alpha}$, in a rectangular computational domain, where the grid is uniform and orthogonal. The α_1, α_2 and α_3 computational coordinates, or the I, J, K computational mesh indices, correspond, generally, to the axial, radial and circumferential directions, respectively. Cell faces are surfaces of constant computational coordinate, with each cell bounded by the six surfaces: $\alpha_1 = I \mp 1/2$, $\alpha_2 = J \mp 1/2$ and $\alpha_3 = K \mp 1/2$.

4.1 Finite Volume Equations

If we let the symbol $\hat{}$ refer to a quantity expressed in terms of cell geometry, then a finite-volume spatial discretization of the pseudo time-dependent form of the linearized unsteady equation (3.13) can be written as

$$\frac{\partial \hat{\mathbf{u}}}{\partial \tau} = -i\omega\hat{\mathbf{u}} - \delta_j \hat{\mathbf{f}}_j + \frac{\partial \mathbf{S}}{\partial \mathbf{U}}\hat{\mathbf{u}} - i\omega(\Delta\vartheta)\mathbf{U} - \delta_j \hat{\mathbf{f}}_j^d + (\Delta\vartheta)\mathbf{S} + \bar{\vartheta}(\mathbf{R}\cdot\nabla_{\bar{\mathbf{x}}})\mathbf{S} = -\hat{\mathbf{r}} \ , \qquad (4.1)$$

where $\hat{\mathbf{u}} = \bar{\vartheta}\mathbf{u}$, $\hat{\mathbf{f}}_j = (\partial\hat{\mathbf{F}}_j/\partial\mathbf{U})\mathbf{u} = \bar{A}_{jk}(\partial\mathbf{F}_k/\partial\mathbf{U})\mathbf{u} = \bar{A}_{jk}\mathbf{f}_k$, and $\hat{\mathbf{f}}_j^d = -\dot{\vartheta}_j\mathbf{U} + a_{jk}\mathbf{F}_k$. Here, the quantities $\mathbf{u}$, $\mathbf{U}$, and $\mathbf{S}$ represent average values of the physical state and source term vectors over a mean cell volume; $\bar{\vartheta}$ is the mean cell volume; $\bar{A}_{jk}$ is the mean area of a constant α_j cell face projected in the $\bar{x}_k$ direction; the vectors $\hat{\mathbf{F}}_j$ and $\hat{\mathbf{f}}_j$ are the steady and unsteady fluxes, respectively, across a constant α_j cell face; $\hat{\mathbf{f}}_j^d$ is the unsteady flux associated with the displacement field, $\mathbf{R}$; and $\hat{\mathbf{r}}$ is the residual of the first-harmonic unsteady equation. The steady quantities $\bar{\vartheta}$, $\bar{A}_{jk}$, $\mathbf{U}$, $\mathbf{F}_j(\mathbf{U})$ and $\mathbf{S}(\mathbf{U},\bar{\mathbf{x}})$ and the unsteady displacement field, $\mathbf{R}$, are regarded as known for the linearized unsteady analysis.

The operator δ_j in equation (4.1) denotes the difference in the j-direction across adjacent cell interfaces, and the repeated j index implies summation over all computational coordinate directions. Thus, the terms $\delta_j\hat{\mathbf{f}}_j$ and $\delta_j\hat{\mathbf{f}}_j^d$ are the net unsteady fluxes through a cell due to the unsteady fluid motion, and the grid motion, respectively. The linearized perturbation equation contains source terms that are associated with changes in cell volume, cell face area, and cell radial location. These terms depend on known steady flow properties and the prescribed displacement field, $\mathbf{R}(\bar{\mathbf{x}})$. In evaluating the volume terms $\Delta\vartheta = \delta_j(\bar{A}_{jk}R_{x_k})$ and $\dot{\vartheta}_j = i\omega\bar{A}_{jk}R_{x_k}$, the R_{x_k} are taken to be the average displacements over a cell face. The perturbations in the cell face areas, a_{jk}, and in cell location are computed using the displacements of the cell vertices.

The unsteady field equation must be solved subject to conditions at the boundaries of the near-field computational domain. The flow tangency conditions at the blade surfaces and duct walls, cf. (3.14), are implemented using phantom cells inside a solid surface. The density and pressure in a phantom cell are defined by a first-order accurate reflection condition, and the phantom cell velocity is defined such that the velocity at the solid surface, which

is the average of the velocities in the phantom and the interior cells, satisfies the flow tangency condition, in a manner consistent with the finite volume discretization. Phase-shifted periodicity, cf. (3.12), is imposed along a passage boundary by taking advantage of grid periodicity in the blade-to-blade direction. Thus, we set $\mathbf{u}|_{I,J,K} = \mathbf{T}_{\pm 1}\mathbf{u}_{I,J,K\pm(NK-1)}\exp(\pm i\sigma)$ where NK denotes the number of blade-to-blade grid points, and the $\mathbf{T}_n$ matrix rotates the x_2 and x_3 components of the momentum vector through n blade passages. Finally, analytic/numeric far-field solutions are matched to the numerical near-field solution at the computational inflow and outflow boundaries, i.e., at $\xi = \xi_{\mp}$.

After replacing the pseudo time derivative in (4.1) by a first-order accurate, two-point, backward, difference expression, and expanding the residual, $\hat{\mathbf{r}}^{n+1}$, about the nth time level, we can write the discretized unsteady field equation as

$$\left(\hat{\Theta}\mathbf{I} + \frac{\partial \hat{\mathbf{r}}}{\partial \mathbf{u}}\right)\Delta\mathbf{u}^n = \left(\hat{\Theta} + i\omega\bar{\vartheta} - \bar{\vartheta}\frac{\partial \mathbf{S}}{\partial \mathbf{U}}\right)\Delta\mathbf{u}^n + \delta_j\left(\frac{\partial \hat{\mathbf{F}}_j}{\partial \mathbf{U}}\Delta\mathbf{u}^n\right) = -\hat{\mathbf{r}}^n \ . \tag{4.2}$$

In equation (4.2), the superscript n refers to the nth pseudo time level, $\hat{\Theta} = \bar{\vartheta}/\Delta\tau$, $\Delta\mathbf{u}^n = \mathbf{u}^{n+1} - \mathbf{u}^n$, $\hat{\mathbf{r}}$ is defined as in (4.1), and $\partial\hat{\mathbf{r}}/\partial\mathbf{u}$ is a constant, since the unsteady residual is a linear function of the state vector $\mathbf{u}$.

4.2 Evaluation of Flux Terms and Pseudo-Time Integration

To simplify the descriptions of the spatial discretizations, used to approximate the flux terms in equation (4.2), and the pseudo-time integration, used to solve this equation, we will consider a "one-dimensional" flow in which $\hat{\mathbf{F}}_j = \hat{\mathbf{F}}$ and $\hat{\mathbf{f}}_j = \hat{\mathbf{f}}$ are the steady and unsteady flux vectors in the $\alpha_j = \alpha$ coordinate direction. The subscript J refers to the cell volume bounded by the cell surfaces at $\alpha = J + 1/2$ and $\alpha = J - 1/2$.

Flux difference splitting is applied to evaluate the flux terms in equation (4.2). The flux, $\hat{\mathbf{f}}_{J+1/2}$, at the $J+1/2$ cell interface is evaluated in terms of the flux in the cell to the left (J) of the interface and the flux due to waves approaching the interface from the right. Thus,

$$\hat{\mathbf{f}}_{J+1/2} = \left(\frac{\partial \hat{\mathbf{F}}}{\partial \mathbf{U}}\mathbf{u}\right)_{J+1/2} \approx \hat{\mathbf{f}}(\mathbf{u}_J, \bar{A}_{J+1/2}) + \left.\frac{\partial \hat{\mathbf{F}}}{\partial \mathbf{U}}\right|^{-}_{\mathbf{U}^{\mathrm{Roe}}_{J+1/2}, \bar{A}_{J+1/2}} (\mathbf{u}_{J+1} - \mathbf{u}_J) \ , \tag{4.3}$$

where $\hat{\mathbf{f}}(\mathbf{u}_J, \bar{A}_{J+1/2})$ is a flux based on the state vector in the Jth cell and the mean area of the $J + 1/2$ cell interface, and the $(-)$ superscript on $\partial\hat{\mathbf{F}}/\partial\mathbf{U}$ indicates left traveling disturbances, which correspond to the negative eigenvalues of the flux Jacobian matrix. The flux Jacobian matrix $\partial\hat{\mathbf{F}}/\partial\mathbf{U}|_{\mathbf{U}^{\mathrm{Roe}}_{J+1/2}, \bar{A}_{J+1/2}}$ is evaluated in terms of the Roe-averaged [Roe81] intermediate state vector, $\mathbf{U}^{\mathrm{Roe}}_{J+1/2}$, and the area, $\bar{A}_{J+1/2}$.

The discrete approximation (4.3) is first-order accurate, since the interfacial fluxes are based only upon information from adjacent cells. Second order spatial accuracy is achieved by adding corrective fluxes, which bring in information from additional neighboring cells. In LINFLUX, the corrective perturbation flux at the $J + 1/2$ interface is comprised of right traveling waves at the upstream interface $(J - 1/2)$ of the Jth cell and left traveling waves

at the downstream interface $(J+3/2)$ of the $(J+1)$th cell. These waves are approximated using the Roe-averaged flux Jacobian matrix at the $J+1/2$ interface.

Once the interfacial fluxes have been computed, they are spatially differenced; i.e., $\delta\hat{\mathbf{f}}\Big|_J \approx \hat{\mathbf{f}}_{J+1/2} - \hat{\mathbf{f}}_{J-1/2}$, to compute the net flux terms that appear on the right- and left-hand sides of equation (4.2). A second-order discrete approximation is used to evaluate the net unsteady flux term that appears on the right-hand side of (4.2). The left-hand side flux term, $\delta[(\partial\hat{\mathbf{F}}/\partial\mathbf{U})\Delta\mathbf{u}]$ is evaluated using the first-order accurate approximation in (4.3).

The linearized unsteady equation (4.2) is discretized, as outlined above, leading to a system of linear algebraic equations. This system is solved, at each pseudo-time step, using a symmetric Gauss-Seidel (SGS) iteration procedure in which the left-hand side matrix is decomposed into diagonal and off-diagonal submatrices. Thus, we set

$$\left(\hat{\Theta}_J\mathbf{I} + \frac{\partial\hat{\mathbf{r}}}{\partial\mathbf{u}}\bigg|_{\mathbf{u}_J^n}\right)\Delta\mathbf{u}_J^n = \mathbf{D}_J\Delta\mathbf{u}_J^n - \mathbf{M}_{J-1}^{+}\Delta\mathbf{u}_{J-1}^n + \mathbf{M}_{J+1}^{-}\Delta\mathbf{u}_{J+1}^n = -\hat{\mathbf{r}}_J^n\,, \qquad (4.4)$$

where the $\mathbf{D}$ submatrix contains the diagonal elements of the original matrix, and the $\mathbf{M}^+$ and $\mathbf{M}^-$ submatrices contain the off-diagonal elements in the negative and positive computational coordinate directions, respectively.

Solutions to equation (4.4), which are coupled iteratively to analytic/numeric far-field solutions, are marched forward in pseudo-time until convergence is achieved, i.e., $||\hat{\mathbf{r}}^n|| \to 0$. The current LINFLUX implementation uses explicit surface boundary conditions. These are incorporated into the SGS iteration procedure, so that they are imposed in a semi-implicit manner. This treatment has been found to yield better convergence properties than a purely explicit implementation.

5. Unsteady Perturbations in the Far-Field

The unsteady solution must be extended into the regions far upstream ($\xi \leq \xi_-$) and far downstream ($\xi \geq \xi_+$) from the blade row. To meet this requirement, we will match approximate far-field solutions, determined from a reduced set of linearized unsteady equations, to the near-field finite-volume solution. The far-field solutions enable the prescription of unsteady aerodynamic disturbances that enter the computational domain (excitations), and the determination of the outgoing disturbances, including the outward propagating acoustic response disturbances.

We have assumed that, far from the blade row ($\xi \lesseqgtr \xi_\mp$), the inner, r_H, and outer, r_D, duct radii are constant, and the circumferentially-averaged, steady flow depends only on radius. Thus, it follows from the governing equations, that the steady velocity has axial and circumferential components, but no radial component, and $dP/dr = \bar{\rho}(V_\theta^{\rm abs})^2/r$. Under these conditions, the linearized unsteady field equation (3.17) reduces to

$$i\omega\mathbf{u} + r^{-1}\frac{\partial(r\mathbf{A}_2\mathbf{u})}{\partial r} + r^{-1}\mathbf{B}_2\frac{\partial \mathbf{u}}{\partial \theta} + \mathbf{C}_2\frac{\partial \mathbf{u}}{\partial \xi} - \mathbf{D}\mathbf{u} = \mathbf{0}\ . \tag{5.1}$$

Equation (5.1) describes the first-order unsteady perturbations far from the blade row. The subscript 2 on the Jacobian matrices in (5.1) indicates that they are evaluated at $U_2^{\rm cyl} = \bar{\rho}V_r = 0$; e.g., $\mathbf{A}_2 \equiv \partial\mathbf{F}_r/\partial\mathbf{U}^{\rm cyl}|_{U_2^{\rm cyl}=0}$.

If the absolute mean flow is uniform in the far field, analytic solutions to equation (5.1) can be determined [TS62, VTM82, VMK95]. Such solutions indicate that an arbitrary first-order unsteady aerodynamic perturbation can be represented as the sum of independent entropic, vortical and irrotational acoustic disturbances. The entropic and vortical disturbances are convected by the mean flow, and, if the axial mean flow is subsonic, modal acoustic disturbances propagate upstream and downstream, or attenuate with increasing axial distance from the blade row.

For nonuniform mean flows, the situation is much more complicated [Kou95, GA97, TA98]. In particular, for rotational, but isentropic, mean flows, the unsteady entropy is an independent convected disturbance, but the unsteady vorticity and pressure are coupled. As a result, nearly-convected, vorticity-dominated, modal disturbances, that contain pressure, and acoustic or pressure-dominated modal disturbances, that contain vorticity, occur. For nonisentropic and rotational mean flows no purely convected disturbance field will exist, because the entropic and vortical disturbances are coupled to the acoustic disturbances [Ker77].

It is difficult to determine the axial and radial behaviors of nearly-convected modal disturbances and very difficult to represent an arbitrary far-field disturbance in terms of series of acoustic and nearly convected modal disturbances. Therefore, to enable practical, three-dimensional, unsteady-flow calculations, some liberties must be taken in describing the unsteady perturbations in the far field.

In the present effort, these perturbations will be modeled as the sum of a finite series of acoustically-dominated modal disturbances and a "convected" or "rotational" disturbance field. Thus, we set $\mathbf{u} = \mathbf{u}_A + \mathbf{u}_C$, where the state vector $\mathbf{u}_A$ describes the modal acoustic

disturbances, and $\mathbf{u}_C$ describes the vortically and/or entropically dominated unsteady perturbation. The state vector $\mathbf{u}_C$ is prescribed at inlet ($\xi = \xi_-$) as an approximate solution to (5.1), and extrapolated or convected through the exit boundary ($\xi = \xi_+$) as a solution of the convection equation $\bar{D}\mathbf{u}_C/Dt = \mathbf{0}$. The axial and radial behaviors of the modal acoustic disturbances are determined by far-field eigenanalyses. The amplitudes of the incoming acoustic disturbances are prescribed; those of the outgoing acoustic disturbances are determined by coupling the near- and far-field solutions for the unsteady state vector $\mathbf{u}$.

5.1 Acoustic Eigensolutions

The acoustic disturbance is determined by substituting an assumed form for a modal disturbance, i.e., $\mathbf{u} = \mathbf{u}^{\mathrm{R}}_{mn}(r)\exp(\chi_{mn}\xi + i\bar{m}\theta)$, into the field equation (5.1), leading to a system of homogeneous ordinary differential equations of the form

$$i\omega\mathbf{I}\,\mathbf{u}^R_{mn} + r^{-1}\frac{d}{dr}\left(r\mathbf{A}_2\,\mathbf{u}^R_{mn}\right) + i\bar{m}r^{-1}\mathbf{B}_2\,\mathbf{u}^R_{mn} + \chi_{mn}\mathbf{C}_2\,\mathbf{u}^R_{mn} - \mathbf{D}_2\,\mathbf{u}^R_{mn} = \mathbf{0}\,. \tag{5.2}$$

After discretizing this system, and applying the duct wall boundary conditions $v_r = 0$ at $r = r_H$ and $r = r_D$, we obtain the matrix equation

$$(\mathbf{P} - \chi_{mn}\mathbf{C}_2)\,\mathbf{u}^R_{mn} = \mathbf{0}, \tag{5.3}$$

where $\mathbf{P} = -i\omega\mathbf{I} - \mathbf{L}(r, \mathbf{A}_2) - i\bar{m}r^{-1}\,\mathbf{B}_2 + \mathbf{D}_2$ and $\mathbf{L}(r, \mathbf{A}_2)$ is a finite difference approximation to $r^{-1}d(r\mathbf{A}_2\mathbf{u}^R_{mn})/dr$. The column vector $\mathbf{u}^R_{mn}$ in equation (5.3) contains an entry for each of the five conservation variables at each radial discretization point.

Equation (5.3) can be solved, using a standard linear algebra routine, to determine the axial eigenvalues, χ_{mn}, and the associated right eigenvectors, $\mathbf{u}^R_{mn}(r)$, of the modal, acoustic disturbances in the far-field. The left eigenvectors, $\mathbf{u}^L_{mn}$, are determined by solving the equation $(\mathbf{P} - \chi_{mn}\mathbf{C}_2)^H\mathbf{u}^L_{mn} = \mathbf{0}$, where the superscript H denotes the conjugate transpose. An orthonormal set of left eigenvectors can then be obtained by setting $(\mathbf{v}^L_{mn})^H = (\mathbf{u}^L_{mn})^H\mathbf{C}_2/[(\mathbf{u}^L_{mn})^H\mathbf{C}_2\mathbf{u}^R_{mn}]$.

The numerical solutions to (5.3) may contain spurious modes, which must be eliminated to yield a valid solution set. In addition, both acoustic and nearly convected disturbances can emerge as solutions to (5.3). The group velocity

$$V_{g,mn} = \frac{\partial\omega}{\partial\chi_{mn}} = \frac{\langle\mathbf{v}^L_{mn}, \mathbf{C}_2\mathbf{u}^R_{mn}\rangle}{\langle\mathbf{v}^L_{mn}, (\partial\mathbf{P}/\partial\omega)\,\mathbf{u}^R_{mn}\rangle}\,, \tag{5.4}$$

i.e., the axial velocity at which an unattenuated mnth modal disturbance carries energy, can be used to distinguish between such solutions. For example, nearly-convected disturbances travel downstream, without attenuation, at axial speeds slightly less than and slightly greater than the mean flow speed. If the axial mean flow is subsonic, acoustic disturbances travel both upstream and downstream. Since the modal nearly-convected disturbances are presumed to be included within the disturbance field represented by the state vector $\mathbf{u}_C$, they must be eliminated to determine a valid acoustic solution.

After the spurious and nearly-convected modes have been eliminated, the remaining eigen-disturbances can be combined to construct the acoustic state vector, $\mathbf{u}_A$. The latter

can be written in the form

$$\mathbf{u}_A(r,\theta,\xi) = \sum_{m=-M}^{M} \exp(i\bar{m}\theta) \sum_{\mu=0}^{M} u \left[a^{-}_{m\mu} \mathbf{u}^{R,-}_{m\mu}(r) \exp\left(\chi^{-}_{m\mu}\xi\right) + a^{+}_{m\mu} \mathbf{u}^{R,+}_{m\mu}(r) \exp\left(\chi^{+}_{m\mu}\xi\right) \right] , \tag{5.5}$$

to emphasize the distinction between upstream, denoted by the superscript $-$, and downstream, denoted by the superscript $+$, traveling waves. Here, M and Mu are positive integers; the index μ indicates the number of radial nodes or zero crossings in the μth radial mode; the $a^{\mp}_{m\mu}$ are the modal complex amplitudes; the $\mathbf{u}^{R,\mp}_{m\mu}(r)$ are right eigenvectors; and the $\chi^{\mp}_{m\mu} = \beta^{\mp}_{m\mu} + i\kappa^{\mp}_{\xi,m\mu}$ are axial eigenvalues.

The radial modes in (5.5) are ordered by their number of zero crossings. To determine if any of the lower order modes are missing, or if spurious modes have been kept, one can count the zero crossings in the kept modes. If there is one upstream and one downstream traveling mode for a each number of zero crossings, then it is likely that only the genuine modes have been retained.

The complex amplitudes, $a^{\mp}_{m\mu}$, of the outgoing modal disturbances are determined by taking inner products involving the $\mathbf{v}^{L,\mp}_{m\mu}$ and the near field state vector $\mathbf{u}$; i.e.,

$$\begin{aligned} a^{\mp}_{m\mu} &= \langle \mathbf{v}^{L,\mp}_{m\mu}, \frac{N}{2\pi} \int_{\theta}^{\theta+2\pi/N} \mathbf{u} \exp(-i\bar{m}\theta) d\theta \rangle \\ &= \frac{1}{r_D - r_H} \int_{r_H}^{r_D} (\mathbf{v}^{L,\mp}_{m\mu})^H \left\{ \frac{N}{2\pi} \int_{\theta}^{\theta+2\pi/N} \mathbf{u} \exp(-i\bar{m}\theta) d\theta \right\} dr \ . \end{aligned} \tag{5.6}$$

Thus, it is being assumed that the inner products $\langle \mathbf{v}^{L,\mp}_{m\mu}, \mathbf{u}_C \rangle$ are negligible; i.e., that the left eigenvectors of the acoustic disturbances are nearly orthogonal to the convected disturbance field.

The far field solutions must be applied in conjunction with a numerical near-field solution to determine the linearized unsteady flow. In the near field, the linearized unsteady governing equations are solved using the pseudo-time marching technique described in §4. After each iterative update of the near-field solution, the amplitudes of the outgoing acoustic modes, i.e., $a^{-}_{m\mu}$ at $\xi = \xi_-$ and $a^{+}_{m\mu}$ at $\xi = \xi_+$, are determined by taking inner products, cf. (5.6), using the near-field state vector, $\mathbf{u}$. At the downstream far-field boundary, the acoustic disturbance, $\mathbf{u}_A$, is subtracted from the total unsteady disturbance, $\mathbf{u}$ and the remainder, $\mathbf{u}_C = \mathbf{u} - \mathbf{u}_A$, is regarded as a convected disturbance; i.e., as a solution of the equation $\bar{D}\mathbf{u}_C/Dt \equiv 0$, to provide an update for $\mathbf{u}_C(r,\theta,\xi_+)$ at the outflow boundary. The new far-field solutions, which are based on the finite numbers of circumferential and radial acoustic modes that can be represented accurately on the near-field computational grid, are then used to supply the inflow and outflow information for the next near-field update.

5.2 Acoustic Response Parameters

It is desirable to introduce real parameters that provide useful descriptions of the unsteady aerodynamic response. For example, the work per cycle, which describes the work done by an airstream, on a blade, over one cycle of motion, is an important parameter in

blade flutter investigations. For aeroacoustic applications, the sound pressure and sound power levels provide convenient measures of the acoustic response far from a blade row. Expressions for evaluating these quantities are derived below.

Consider the first-order unsteady flow variables, $\tilde{a}(\mathbf{x},t) = \mathrm{Re}\{a(\mathbf{x})\exp(i\omega t)\}$ and $\tilde{b}(\mathbf{x},t) = \mathrm{Re}\{b(\mathbf{x})\exp(i\omega t)\}$. The time-mean value, $\langle\tilde{a}\tilde{b}\rangle$, of the product $\tilde{a}\tilde{b}$, is given by

$$\langle\tilde{a}\tilde{b}\rangle = (2\pi)^{-1}\int_0^{2\pi}\tilde{a}\tilde{b}d(\omega t) = (ab^* + a^*b)/4 = \mathrm{Re}\{ab^*/2\}\ , \tag{5.7}$$

where the superscript * indicates the complex conjugate. The area-averaged, time-mean value, $\langle\langle\tilde{a}\tilde{b}\rangle\rangle$, of $\tilde{a}\tilde{b}$ is given by

$$\langle\langle\tilde{a}\tilde{b}\rangle\rangle = A_D^{-1}\int_{A_D}\langle\tilde{a}\tilde{b}\rangle dA_D = \frac{1}{2}A_D^{-1}\mathrm{Re}\left\{\int_{r_H}^{r_D}\int_0^{2\pi}ab^*rd\theta dr\right\}\ . \tag{5.8}$$

If the flow variables $\tilde{a}$ and $\tilde{b}$ are associated with the far-field acoustic response of a blade row, then, it follows from (5.5) that the product ab^* can be expressed in the form

$$ab^* = \sum_{m=-\infty}^{\infty}\sum_{\mu=0}^{\infty}\sum_{n=-\infty}^{\infty}\sum_{\nu=0}^{\infty}a_{m\mu}a_{n\nu}^*\psi_{m\mu}^a(\psi_{n\nu}^b)^* \times \exp\left[i(\bar{m}-\bar{n})\theta + (\chi_{m\mu}+\chi_{n\nu}^*)\xi\right]\ , \tag{5.9}$$

where $a_{m\mu}$ and $a_{n\nu}$ are modal complex amplitudes and $\psi_{m\mu}^a(r)$ and $\psi_{n\nu}^b(r)$ are modal radial shape functions. After substituting (5.9) into (5.8), integrating with respect to θ, and restricting consideration to propagating acoustic response waves, we find that

$$\langle\langle\tilde{a}\tilde{b}\rangle\rangle = \pi A_D^{-1}\mathrm{Re}\left\{\sum_{m,\mu,\nu^{\mathrm{Prop}}}a_{m\mu}a_{m\nu}^*\exp\left[i(\kappa_{m\mu}-\kappa_{m\nu})\xi\right]\times\int_{r_H}^{r_D}\psi_{m\mu}^a\left(\psi_{m\nu}^b\right)^*rdr\right\}\ . \tag{5.10}$$

For acoustic perturbations of uniform absolute mean flows, the integrals in (5.10) are zero if $\mu \neq \nu$, since the radial shape functions are orthogonal. This is not true, in general, for the acoustic perturbations of arbitrary mean flows. However, if the modal integrals do not vanish for $\mu \neq \nu$, then $\langle\langle\tilde{a}\tilde{b}\rangle\rangle$ in (5.10) will be made up of terms that vary harmonically with ξ. In this case, we can determine the axial mean value of $\langle\langle\tilde{a}\tilde{b}\rangle\rangle$ as

$$\langle\langle\langle\tilde{a}\tilde{b}\rangle\rangle\rangle = \pi A_D^{-1}\mathrm{Re}\left\{\sum_{m,\mu^{\mathrm{prop}}}|a_{m\mu}|^2\int_{r_H}^{r_D}\psi_{m\mu}^a\left(\psi_{m\nu}^b\right)^*rdr\right\}\ . \tag{5.11}$$

Sound Pressure Level

If we set $\tilde{a}$ and $\tilde{b}$ both equal to the unsteady pressure, $\tilde{p}$, in the foregoing equations, then $\tilde{a}\tilde{b} = \tilde{p}^2$ is the square of the pressure, $\langle\tilde{a}\tilde{b}\rangle = \langle\tilde{p}^2\rangle$ is the mean-square pressure, $\langle\langle\tilde{a}\tilde{b}\rangle\rangle = \langle\langle\tilde{p}^2\rangle\rangle$ is the area-averaged, mean-square pressure, and

$$\langle\langle\langle\tilde{a}\tilde{b}\rangle\rangle\rangle = \langle\langle\langle\tilde{p}^2\rangle\rangle\rangle = \frac{1}{(r_D^2-r_H^2)}\sum_{m,\mu^{\mathrm{Prop}}}|a_{m\mu}|^2\int_{r_H}^{r_D}|\psi_{m\mu}|^2rdr \tag{5.12}$$

is the axial mean value of the area-averaged, mean-square pressure. The sound pressure level, SPL, of the acoustic response is based on $\langle\langle\langle\tilde{p}^2\rangle\rangle\rangle$ and defined as:

$$\mathrm{SPL} = 10\log_{10}\left(\frac{\langle\langle\langle\tilde{p}^2\rangle\rangle\rangle}{P_{\mathrm{Ref}}^2}\right), \tag{5.13}$$

where $P_{\mathrm{Ref}} = 2 \times 10^{-5}$ N/m^2 $= 4.17706 \times 10^{-7}$ lb$_\mathrm{f}$/ft^2.

Sound Power Level

If we set $a = \bar{\rho}^{-1}(\tilde{p} + \bar{\rho}V_x\tilde{v}_x)$ and $b = \bar{\rho}\tilde{v}_x + \tilde{\rho}V_x$, then $\tilde{a}\tilde{b}$ is the axial component of the acoustic energy flux, $\langle\tilde{a}\tilde{b}\rangle$ is the acoustic power or intensity, $\langle\langle\tilde{a}\tilde{b}\rangle\rangle$, is the area-averaged acoustic power, and

$$\langle\langle\langle\tilde{a}\tilde{b}\rangle\rangle\rangle = \pi A_D^{-1}\mathrm{Re}\left\{\sum_{m,\mu^{\mathrm{Prop}}} |a_{m\mu}|^2 \int_{r_H}^{r_D} \psi_{m\mu}^a (\psi_{m\mu}^b)^* r dr\right\} \tag{5.14}$$

is the axial mean value of the area-averaged acoustic power. The sound power level, PWL, of the acoustic response is defined by

$$\mathrm{PWL} = 10\log_{10}\left(\frac{A_D\langle\langle\langle\tilde{a}\tilde{b}\rangle\rangle\rangle}{\mathrm{PW}_{\mathrm{Ref}}}\right), \tag{5.15}$$

where $\mathrm{PW}_{\mathrm{Ref}} = 10^{-12}$ watts $= 0.737572 \times 10^{-12}$ ft$-$lb$_\mathrm{f}$/sec.

5.3 Wake Excitation Model

The wake-excitation model, currently used with LINFLUX, is based on classical, thin, viscous-layer concepts, and on the foregoing far-field analysis. Thus, it is assumed that the flow within each wake is parallel and changes in the pressure and density across each wake are negligible. In addition, a quasi-3D approximation is used to determine the axial behavior, at inlet, of the "convected" wake perturbation velocity.

Consider a reference rotating or stationary blade row, cf. Figure 2, which receives the flow exiting from an adjacent upstream row; i.e., a stator or a rotor, respectively. The upstream and reference blade rows rotate at constant angular velocity $\boldsymbol{\Omega}'$ and $\boldsymbol{\Omega}$. Therefore, the upstream blade row rotates at angular velocity $\boldsymbol{\Omega}' - \boldsymbol{\Omega} = \boldsymbol{\Omega}_R = \Omega_R\mathbf{e}_\xi$ relative to the reference array, where Ω_R is the absolute angular velocity of the rotor. Because the blade rows move relative to each other, any downstream, circumferential, flow nonuniformity produced by the upstream blade row; in particular, one due to the viscous blade wakes, will excite an unsteady flow through the reference row. Although the wake excitation is due to viscous effects, it is modeled here as an inviscid velocity perturbation at the inlet to the responding or reference blade row.

We will analyze the flow at the inlet to the reference blade row in terms of cylindrical coordinates (r, θ, ξ) and $(r, \theta' = \theta - \Omega_R t, \xi)$ attached to the reference and the upstream or excitation blade rows, respectively. Here, θ and θ' measure angular distance in the $\mathbf{e}_\xi \times \mathbf{e}_r = \mathbf{e}_\theta$ or clockwise direction, when viewed from upstream, and the radial unit vector $\mathbf{e}_r$ points

from hub to tip. We assume that in the absence of the reference blade row, the flow "far" downstream of the excitation blade row is steady in the r, θ', ξ coordinate frame, with relative velocity, $\tilde{\mathbf{V}}'(r, \theta', \xi)$, density, $\tilde{\rho}$, and the pressure $\tilde{P}$, given by

$$\begin{aligned} \tilde{\mathbf{V}}'(r, \theta', \xi) &= \mathbf{V}'(r) + \tilde{\mathbf{v}}^{\mathrm{R}}(r, \theta', \xi) + \dots \\ &= [V'(r) + \tilde{v}^{\mathrm{R}}(r, \theta', \xi)]\mathbf{e}_T(r) + \dots = \tilde{V}'(r, \theta', \xi)\mathbf{e}_T(r), \qquad (5.16) \\ \tilde{\rho}(r, \theta', \xi) &= \bar{\rho}(r) + \dots \quad \text{and} \quad \tilde{P}(r, \theta', \xi) = P(r) + \dots . \end{aligned}$$

Here $\mathbf{V}'$, $\bar{\rho}$ and P are circumferentially-averaged flow variables, $\tilde{\mathbf{v}}^{\mathrm{R}}(r, \theta, \xi)$ is the first-order velocity perturbation due to the wakes from the upstream blade row, the density and pressure fluctuations associated with this velocity perturbation are assumed to be negligible, and $\mathbf{e}_T(r)$ is a unit vector tangent to the cylinder r = constant and pointing in the far-downstream flow direction.

Thus, far downstream of the excitation blade row, the radial component of the total fluid velocity is negligible and the circumferentially-averaged fluid velocity, $\mathbf{V}'$, depends only on radius. The circumferentially-averaged flow is assumed to be a solution of the conservation equations; i.e., the nonlinear Euler equations, for steady inviscid flow. However, the wake perturbation will be modeled as an approximate solution of the linearized Euler equations. Note that, if the upstream blade row is a stator, $\boldsymbol{\Omega}' = \mathbf{0}$, $\mathbf{V}'$ is the absolute steady velocity, $\boldsymbol{\Omega} = -\Omega_R \mathbf{e}_\xi$, and $\mathbf{V}$ is the velocity relative to the reference rotor blade row. If the upstream blade row is a rotor, $\boldsymbol{\Omega}' = \Omega_R \mathbf{e}_\xi$, $\mathbf{V}'$ is the velocity relative to the rotor, $\boldsymbol{\Omega} = \mathbf{0}$, and $\mathbf{V}$ is the absolute fluid velocity. In both situations, $\boldsymbol{\Omega}' - \boldsymbol{\Omega} = \Omega_R \mathbf{e}_\xi$, where Ω_R is the absolute angular speed of the rotor. Also, the perturbation velocity, $\tilde{\mathbf{v}}^{\mathrm{R}}$, is invariant under a transformation from the r, θ', ξ frame to the r, θ, ξ frame.

The flow speed, $\tilde{V}' = \tilde{\mathbf{V}}' \cdot \mathbf{e}_T$, can be represented as a Fourier series in θ'; i.e.,

$$\tilde{V}'(r, \theta', \xi) = \sum_{n=-\infty}^{\infty} V'_n(r, \xi) \exp(-inN'\theta') = V'_0(r) + \sum_{n=1}^{\infty} \mathrm{Re}\{v_n^{\mathrm{R}}(r, \xi) \exp(-inN'\theta')\}, \quad (5.17)$$

where $N' > 0$ is the number of blades in the upstream blade row and

$$V'_n(r, \xi) = \frac{N'}{2\pi} \int_{\theta'}^{\theta'+2\pi/N'} \tilde{V}'(r, \theta', \xi) \exp(inN'\theta') d\theta', \quad n = 0, \pm 1, \pm 2, \dots . \qquad (5.18)$$

Here, $V'_0 = V'$ is the circumferentially-averaged flow speed far downstream of the excitation blade row, and $v_n^{\mathrm{R}}(r, \xi) = 2V'_n$, $n = 1, 2, \dots$, is the complex amplitude of the nth circumferential harmonic of the perturbation flow speed. The velocity $\tilde{\mathbf{V}}'$ can be determined experimentally or from a Navier-Stokes solution for the steady flow relative to the upstream blade row.

We assume that the Fourier components of the perturbation velocity, $\mathbf{v}_n^{\mathrm{R}} = v_n^{\mathrm{R}} \mathbf{e}_T$, vary harmonically with axial distance, i.e., $v_n^{\mathrm{R}}(r, \xi) = v_n^{\mathrm{R}}(r) \exp(in\kappa_\xi \xi)$. Then, the fundamental wave number of this "convected" velocity perturbation is given by

$$\boldsymbol{\kappa} = \kappa_T \mathbf{e}_T = (\kappa_\xi V_\xi - r^{-1} N' V'_\theta)\mathbf{e}_T / V' = 0 , \qquad (5.19)$$

where κ_T is the wave number in the relative flow direction.

The flow exiting from the upstream or excitation blade row enters the field of the reference blade row. In particular, the imposed velocity at the inlet to the reference blade row is

$$\tilde{\mathbf{V}} = \tilde{\mathbf{V}}' + \Omega_R \mathbf{e}_\xi \times \mathbf{r} = \mathbf{V}' + \Omega_R r \mathbf{e}_\theta + \tilde{\mathbf{v}}^{\mathrm{R}} + \ldots = \mathbf{V} + \tilde{\mathbf{v}}^{\mathrm{R}} + \ldots \ . \tag{5.20}$$

Thus, in terms of the coordinates r, θ, ξ fixed to the reference blade row, the steady and unsteady perturbation velocities at inlet are given by

$$\mathbf{V}(r) = V_\xi \mathbf{e}_\xi + (V'_\theta + \Omega_R r)\mathbf{e}_\theta = V_\xi \mathbf{e}_\xi + V_\theta \mathbf{e}_\theta \tag{5.21}$$

and

$$\tilde{\mathbf{v}}^{\mathrm{R}} = \sum_{n=1}^{\infty} \mathrm{Re}\{\mathbf{v}_n^{\mathrm{R}} \exp[in(\kappa_\xi \xi - N'\theta + N'\Omega_R t)]\} \ , \tag{5.22}$$

where

$$\tilde{\mathbf{v}}_n^{\mathrm{R}} = (v_n^{\mathrm{R}}/V')(V_\xi \mathbf{e}_\xi + V'_\theta \mathbf{e}_\theta) = (v_n^{\mathrm{R}}/V')[V_\xi \mathbf{e}_\xi + (V_\theta - \Omega_R r)\mathbf{e}_\theta] \ , \tag{5.23}$$

$N'\Omega_R = \omega$ is the fundamental excitation frequency in the frame of the reference blade row, and $\kappa_\xi = -(\omega - r^{-1}N'V_\theta)/V_\xi$ is the axial wave number of the fundamental wake excitation. The fundamental disturbance repeats N' times around the wheel and has an interblade phase angle, σ, of $-2\pi N'/N$, where N is the number of blades in the reference blade row.

At each radial station, the first-order velocity perturbation in (5.22) satisfies the linearized, inviscid, conservation equations for mass, axial and circumferential momenta, and energy. However, it does not conserve radial momentum, unless the absolute steady background flow is uniform. Thus, for a nonuniform, absolute mean flow, it is, at best, only a convenient, and hopefully useful, approximate solution to the fluid-dynamic equations governing the linearized inviscid flow through the reference blade row.

6. ADP Rotor-Wake/FEGV Interactions

We have applied the LINFLUX analysis to predict unsteady flows through the fan exit guide vane (FEGV) of the NASA/PW, 22 inch, advanced ducted propulsor (ADP). These flows are excited by circumferential nonuniformities in the flow exiting the fan rotor, which are due primarily to the viscous wakes extending downstream from the rotor blades. We will consider two ADP power settings; a low power or approach setting and a high power or take-off setting, and apply LINFLUX to predict the unsteady aerodynamic responses of the FEGV to Fourier components, at multiples of the blade passing frequency (BPF), of the rotor wake excitation.

A schematic of the advanced ducted propulsor is shown in Figure 3. The fan consists of 18 blades which rotate clockwise, when viewed from upstream, about the duct axis. The radius of the fan is 11 in and the nominal blade chord, measured over the outer span, is 3.5 in. The fan exit guide vane , cf. Figure 4, is placed at an axial distance from the rotor-tip trailing edge to the stator-tip leading edge of 5.3 in. It consists of 45 blades, which are twisted, bowed, flared at the tip, and have rounded leading and trailing edges. The FEGV resides in an aft duct of variable inner and outer radii. The chord, c^*, and axial chord, c^*_{ax}, of the stator vanes, at midspan, are 1.666 in and 1.625 in, respectively. The chord is the reference length used in non-dimensionalizing the TURBO and LINFLUX variables. It is taken to be the linear distance between the vane leading- and trailing-edge points, at midspan.

Measurements of the rotor exit flow, with the stator moved well aft of its design position, were taken at NASA Glenn Research Center [Pod97]. Circumferentially-averaged values of the absolute total temperature and absolute total pressure were determined at 10 radial stations in an axial measurement plane located 3.720 in downstream of the rotor-tip trailing edge. In addition, LDV measurements of the rotor exit velocity were taken at 29 radial and 51 circumferential locations in an axial plane located 2.650 in downstream of the rotor-tip trailing edge. This data has been post-processsed to provide analytical inflow conditions for the TURBO and LINFLUX, steady and linearized unsteady flow calculations. The measured velocity field downstream of the fan, for the low power setting, cf. Figure 5, shows strong nonuniformities in the rotor exit flow due to rotor-wake and duct-wall phenomena.

6.1 FEGV Geometry and Computational Grid

To enable the application of the TURBO and LINFLUX analyses, we have introduced several geometric modifications to the actual FEGV configuration. In particular, a wedge-shaped, trailing-edge sections, approximately 0.2 in long, have been added to the original vanes, so that, the analytical vanes close in sharp trailing edges. This modification is needed to eliminate time-dependent, trailing-edge separations from the TURBO predictions for the nonlinear background flow; thereby allowing the TURBO calculations to converge to a steady solution. In addition, we have modified the aft-duct geometry, to provide a duct with inlet and exit sections of constant inner and outer radii, in accordance with the assumptions used in developing the steady and unsteady far-field analyses.

The computational domain prescribed for the TURBO and LINFLUX, FEGV calculations extends axially 1.593 in upstream and 3.407 in downstream from a blade leading edge

at midspan. The constant radii duct sections at inlet and exit extend almost to the blade row and have inner and outer radii of $r_H^* = 5.810$ in and $r_D^* = 11.410$ in at inlet; and of $r_H^* = 6.426$ and $r_D^* = 11.288$ in at exit. In terms of the dimensionless coordinates used in the TURBO and LINFLUX calculations; i.e. $\xi = \xi^*/c^*$ and $r = r^*/c^*$, the key axial coordinates are $\xi = -0.956$ at the computational inlet boundary, $\xi = 0$ at the midspan leading-edge point, $\xi = 0.975$ at the midspan blunt trailing-edge point, $\xi = 1.085$ at the midspan sharp trailing-edge point, and $\xi = 2.045$ at the computational exit boundary. The inner and outer radii, $r = r^*/c^*$, are 3.487 and 6.849 for the inlet duct section, and $r_H = 3.857$ and $r_D = 6.776$ for the exit section. The axial plane at which the total temperature and total pressures were measured occurs at $\xi = -0.948$; that at which the velocity measurements were taken, at $\xi = \xi_E = -1.591$.

The TIGER grid generator [SS91] has been used to define a three-dimensional H-grid, for the FEGV steady and unsteady flow calculations. The numerical results, reported herein, were determined on an H-grid, consisting of 173 axial, 25 radial, and 41 tangential surfaces (165,120 cells). This grid extends axially from $\xi = -0.956$ to $\xi = 2.045$ with 67 axial grid surfaces positioned upstream of the blade row, 75 intersecting the modified blade surfaces and 31 positioned downstream of the blade row. Axial grid surfaces are clustered near the blade leading and trailing edges; circumferential surfaces, near the blade suction and pressure surfaces; and radial surfaces, near the blade tip.

Four radial stations, which we will refer to as reference stations, of the H-grid used for the FEGV calculations are shown in Figure 6. The reference radial stations occur near the tip, near seventy five percent span, near midspan, and near the hub. The LINFLUX near-field, finite-volume solutions, computed on this grid, are coupled to far-field acoustic eigensolutions, which have been determined on a radial grid consisting of 36 points clustered near the hub and duct walls. For the unsteady flows under consideration, the unsteady wake excitations are prescribed at inlet, and convected and/or nearly convected disturbances are numerically convected through the computational outflow boundary.

6.2 Rotor-Exit/Stator-Inlet Conditions

As in §5, we assume that the flow downstream of the fan can be represented as the sum of a circumferentially-averaged steady relative flow, in which the flow variables vary only with radius, and a first-order perturbation, in which the velocity is aligned with the relative mean flow velocity and the density and pressure are negligible. Moreover, in an attempt to prescribe an excitation that is an approximate solution of the unsteady equations, we require that the perturbation velocity satisfy a two-dimensional convection equation at each radial station. Thus, the absolute steady and unsteady velocities, cf. equations (5.21) and (5.22), at the stator inlet have the form

$$\mathbf{V}^{\text{abs}} = V^{\text{rel}}\mathbf{e}_T + \Omega r \mathbf{e}_\theta = V_\xi \mathbf{e}_\xi + (V_\theta^{\text{rel}} + \Omega r)\mathbf{e}_\theta \tag{6.1}$$

and

$$\tilde{\mathbf{v}}^{\text{R}} = \tilde{v}^{\text{R}}\mathbf{e}_T = \sum_{n=1}^{\infty} \text{Re}\left\{v_n^{\text{R}}\mathbf{e}_T \exp[in(\kappa_\xi \xi - N_B\theta^{\text{abs}} + N_B\Omega t)]\right\}, \tag{6.2}$$

respectively. The superscripts abs and rel refer to quantities measured in the stator and rotor frames, respectively, $\omega^{\text{abs}} = N_B\Omega$, $\kappa_\xi = -(\omega^{\text{abs}} - r^{-1}N_B V_\theta^{\text{abs}})/V_\xi$ and $\sigma = -2\pi N_B/N_V$

are the (reduced) frequency, axial wave number and interblade phase angle, respectively, of the fundamental or 1 BPF wake excitation, N_B and N_V are the numbers of rotor blades and stator vanes, respectively, and Ω is the angular speed of the rotor. The flow velocities $V^{\rm rel}$ and $v_n^{\rm R}$, $n = 1, 2, \ldots$, can be determined by a Fourier analysis of the rotor exit velocity, cf. (5.17) and (5.18). The state vector, $\tilde{\mathbf{u}}_C$ for this quasi-3D, rotor-wake excitation; i.e., $(\tilde{\mathbf{u}}_C)^T = \bar{\rho}[0,\ 0,\ \tilde{v}_\theta^{\rm R},\ \tilde{v}_\xi^{\rm R}, V_\theta^{\rm abs}\tilde{v}_\theta^{\rm R} + V_\xi v_\xi^{\rm R}]$, describes a first-order perturbation in which mass, axial and circumferential momenta, and energy are conserved, but radial momentum is not conserved, unless $\mathbf{V}^{\rm abs}$ is uniform.

Analytic Inflow Conditions

The inflow conditions for the FEGV, steady and unsteady calculations; i.e., the radial distributions of the circumferentially-averaged, absolute, total temperature, $T_T^{\rm abs}$, total pressure, $P_T^{\rm abs}$, and tangential flow angle, $\Omega^{\rm abs} = \tan^{-1}\left(V_\theta^{\rm abs}/V_\xi\right)$, and the complex amplitudes, $v_n^R(r)$, of the wake perturbation velocity, are determined by post-processing the NASA data for the rotor exit flow. Post-processing is required to avoid inlet conditions that lead to separation in the TURBO solution; remove axial vorticity phenomena at the duct walls and provide a more or less classical wake excitation that can be accommodated by LINFLUX; and to account for the diffusion of the viscous wakes as they are convected downstream.

The analytic inlet, total temperature and total pressure distributions are obtained by fitting cubic polynomials to the NASA data; the analytic flow angle distribution, by fitting a linear curve for $r_H < r \leq r_M$ and continuing this into a quadratic curve for $r_M \leq r < r_D$, where r_M is the approximate radial location at which $\Omega^{\rm abs}$ reaches a minimum. The fitting coefficients are adjusted to avoid inflow angles that lead to separation in the TURBO solution.

The analytic wake excitation has been derived from the NASA velocity data in the following manner. First, the measured wake velocity perturbation is determined by subtracting the circumferentially-averaged values of the measured, relative velocity from the actual relative velocity. Since the radial velocity was not measured, and is assumed to be zero, this yields a velocity perturbation with components, that are parallel, $\tilde{v}_T$, and normal, $\tilde{v}_N$, to the circumferentially-averaged, relative velocity at the velocity measurement plane, $\xi = \xi_E$. The normal component of the wake perturbation velocity is generally found to be small. Thus, in keeping with the assumptions used in developing the LINFLUX wake-excitation model, only the parallel component of the measured perturbation velocity is used to construct the analytic wake excitation velocity.

In current wake-excitation models [MG84, TE99, Top00], the wakes are assumed to be identical from blade to blade. At each radial station, the perturbation velocity, $\tilde{v}_T(N)$, in a single wake, is assumed to be symmetric relative to a wake centerline at $N = 0$. The velocity distribution, $\tilde{v}_T(N)$, is described in terms of the wake-edge, $\tilde{v}_{T,e}$, and centerline, $\tilde{v}_{T,\rm min}$, velocities and a shape function, $f(N)$. In the present study, a symmetric, hyperbolic secant, velocity profile has been fitted to the NASA data for $\tilde{v}_T(r, \theta, \xi_E)$ to provide an analytic description of the wake excitation velocity at each radial station. In addition, the radial and circumferential distributions of the fitted wake velocity are modified near the duct walls to remove splitter and end wall effects (cf. Figure 5), and provide a more or less classical wake excitation from hub to tip. The fitted wake perturbation velocity is assumed to act in the direction of the analytic, rather than the measured, relative mean velocity.

Finally, the diffusion of the viscous wakes, as they approach the FEGV must be taken into account. Based on the fitted velocity profiles, the wake velocity defect, $\tilde{v}_{T,e} - \tilde{v}_{T,\min}$, and half-width at the measurement plane are determined as functions of radius. Empirical relations [MG84] are then applied to describe the effects of viscous diffusion on the behavior of the wake velocity defect and half-width, and hence, on that of the wake velocity distribution, with increasing streamwise distance downstream of the rotor. The viscous wake velocity profiles at some reference axial plane, taken here to be the FEGV, midspan, leading-edge plane, are then used to determine the Fourier coefficients, v_n^R, of an equivalent inviscid wake-excitation at the FEGV, computational, inlet plane. Thus, the Fourier components of the inviscid wake excitation that are prescribed, at inlet, to LINFLUX, are based on an empirically determined, viscous, rotor-wake, velocity distribution at the FEGV, midspan, leading-edge plane. This viscous velocity distribution is, in turn, based on the measurements taken downstream of the rotor at NASA.

Numerical Results

At this point, we have described the analytic FEGV vane and duct geometries, the grid used for the steady and unsteady flow calculations, and the manner in which the analytic inflow conditions were determined from the NASA data. We will proceed to present numerical results in §7 and §8 that describe the flows through the FEGV at the low and high ADP power settings. AWAKEN results will be given for the circumferentially-averaged inflow conditions, the rotor-wake excitation velocity at the FEGV leading edge, and the Fourier components of this velocity. TURBO predictions will be given for the steady pressure field and the steady vane-surface pressure distributions. Finally, LINFLUX results will be given for the imaginary components of the unsteady velocity and pressure fields; the real and imaginary unsteady vane-surface pressure distributions; the axial eigenvalues of far-field acoustic disturbances; the radial shapes of the propagating acoustic response modes; and the modal and total, sound pressure and sound power levels of the acoustic responses at inlet and exit. The predicted sound power levels at exit will be compared with measured data.

The component codes of the LINFLUX Prediction System use different forms of the flow variables. As a result, the rotor-exit/FEGV inflow conditions are reported below, in terms of the dimensional flow variables used in AWAKEN. The steady and unsteady flows through the FEGV are, for the most part, described in terms of the non-dimensional flow variables, discussed in §2 of this report, and used in the LINFLUX output routines. Steady inflow and outflow results are also reported in terms of the non-dimensional variables used in TURBO.

For the low power setting, unsteady response predictions have been determined for rotor-wake excitations at 1, 2, and 3 times the blade passing frequency. However, the results for the 3 BPF excitation are inaccurate. They are included here for the sake of completeness and for possible future reference. Unsteady results at the high power setting are given for 1 and 2 BPF wake excitations. In this case, a converged LINFLUX solution could not be determined for the 3 BPF excitation. The TURBO and LINFLUX calculations have been performed on the $173 \times 25 \times 41$ near-field mesh, shown in Figure 6. The LINFLUX far-field analysis was performed on a 36 point radial mesh. The TURBO calculations required several days of CPU time on an IBM 3CT workstation to converge to an attached, low-loss, steady solution. Typically, the LINFLUX calculations required 20 CPU hours on the same machine to converge to an unsteady solution.

7. Numerical Results: Approach Power Setting

At the low power setting, the fan of the ADP rotates at an angular speed of 5,425 rpm and the mass flow rate through the FEGV is 45.2 lb_m/sec. Radial distributions of the measured and analytic, absolute, total temperature, T_T^{abs}, total pressure, P_T^{abs}, and tangential flow angle, $\Omega^{abs} = \tan^{-1}\left(V_\theta^{abs}/V_\xi\right)$, at the rotor exit (stator inlet) are shown in Figure 7. The analytic distributions are used as inlet conditions for the TURBO calculation of the steady background flow through the FEGV. Note that, in the tip region, the analytic inflow angles have been set deliberately at values less than those measured, so that the TURBO analysis will yield an attached steady-flow solution. The analytic exit-plane static pressure at the hub is determined by adjusting the prescribed value of this pressure, by trial and error, until the analytical and experimental mass-flow rates are the same.

Although the inflow values of T_T^{abs} and P_T^{abs}, prescribed for the TURBO calculation, are in excellent agreement with the corresponding experimental data, and the values of Ω^{abs} are in good agreement, there are differences between the calculated and the measured mean flow velocities. The circumferentially-averaged, measured, relative and absolute velocities at the rotor exit (stator inlet) are shown in Figure 8, along with the values determined from the TURBO steady flow solution. The differences between the measured and calculated steady inflow velocities are due, in part, to the differences between the measured and prescribed values of Ω^{abs}. However, the attempt to model the measured viscous flow by an analytical inviscid flow at the same mass flow rate is probably a more important contributor.

Circumferential distributions, over 3 rotor passages, of the analytic, rotor-wake, velocity perturbation, $\tilde{\mathbf{v}}^R = \tilde{v}^R \mathbf{e}_T$, at the midspan leading-edge plane of the stator, as determined from the NASA data and the post-processing steps outlined in §6, are shown in Figure 9. In this figure, θ_G is the angular gap of the rotor and, for clarity, the velocity profiles at each radius are offset by $r/r_D \times 10^3$. The curves in Figure 9 indicate only the behavior of the magnitude of the tangential perturbation velocity, but there are also strong radial changes in the direction, $\mathbf{e}_T$, of this velocity, as indicated by the solid curve for Ω^{rel} in Figure 8. The circumferential location at which the minimum wake velocity occurs, also varies significantly along the span. The velocity profiles in Figure 9 indicate that the wake velocity defect and half-width are relatively large near the hub and tip, and much smaller over the blade midspan region. Some of this behavior could be due to endwall and splitter effects that are still present in the post-processed wake velocity data.

Radial distributions of the amplitude, $|v_n^R|$, and phase, $\arg(v_n^R)$, of the first five Fourier components of the analytic wake excitation at the stator leading edge are shown in Figure 10. The amplitudes of the Fourier excitations decrease with increasing circumferential mode number, n. Also, the amplitude of the first harmonic excitation shows a strong radial dependence, varying from approximately 25 ft/sec at the hub, to 10 ft/sec at midspan, to 27 ft/sec at the tip. The higher harmonics show much smaller variations in amplitude. In particular, the amplitude of the 2 BPF excitation varies from 7 to 10 ft/sec over the span; that of the 3 BPF excitation, from 3 to 5 ft/sec. Large radial variations in phase also occur; e.g., a phase angle variation of approximately 160 deg for the first harmonic, 360 deg for the second harmonic, and 520 deg for the third harmonic.

7.1 Steady Background Flow

The steady flow through the FEGV, for the low power setting, has been determined by applying the TURBO 3D Euler analysis on the computational grid illustrated in Figure 6. The radial distributions of absolute total temperature, absolute total pressure and absolute flow angle, indicated by the solid curves in Figure 7, are prescribed at the computational inlet plane, located at $\xi = \xi_- = -0.956$, and the static pressure at the hub is specified at exit, $\xi = \xi_+ = 2.045$, such that the calculated mass-flow rate matched that measured in the NASA Glenn experiment. The computed results indicate that the isentropic, absolute, Mach number at inlet increases from 0.240 at the hub ($r = 0.509 r_D$) to a maximum of 0.346 at $r = 0.827 r_D$, and decreases from 0.346 to 0.309 at the tip. At the exit, this Mach number increases from 0.151 at the hub ($r = 0.569 r_D$) to a maximum of 0.318 at $r = 0.866 r_D$, and decreases from 0.318 to 0.294 at the tip.

Selected results from the TURBO calculation are given in Figure 8 and in Figures 11 through 13. The steady pressure field is shown, at the four reference spanwise stations, in Figure 11. The pressure is nearly constant at the computational inlet and exit boundaries, and the steady pressure gradients, generated by the flow through the FEGV, die out within short axial distances from the blade row. Because of steady blade loading, there is a small pressure rise across the FEGV. The steady pressure distributions over the suction and pressure surfaces of a modified vane, i.e., the original vane with a wedge-shaped trailing-edge section added, are shown in Figure 12. The pressure distributions indicate an increase in blade loading from the hub to approximately 75% span. There are flow overspeeds, just downstream of the vane leading edge, at the J =16 and J =22 stations, leading to peak Mach numbers of 0.499 and 0.435, respectively, on suction surface of each vane. Aft of the leading-edge region, peak isentropic Mach numbers of approximately 0.359, 0.469, 0.469 and 0.440 occur in the vicinity of $\xi = 0.25 c_{ax}$ at the J = 4, 10, 16 and 22 radial stations, respectively.

Radial distributions of the steady density, pressure, and velocity at the computational inlet and exit planes of the FEGV are shown in Figure 13. To separate the curves in Figure 13, the results are reported in terms of the non-dimensional flow variables, used in the TURBO code. Thus, the density is scaled by the reference density, $\rho^*_{\text{Ref}} = 0.0764$ $\text{lb}_\text{m}/\text{ft}^3$; pressure, by the reference pressure, $P^*_{\text{Ref}} = 2,116.2$ $\text{lb}_\text{f}/\text{ft}^2$; and velocity by the reference sound speed $A^*_{\text{Ref}} = 1,116.8$ ft/sec. The reference density and sound speed are determined from the reference pressure and temperature, $T^*_{\text{Ref}} = 519$ °R, using the perfect gas relations.

The results in Figure 13 indicate that the steady pressure and density are nearly constant over the inlet and exit planes, and there is a slight rise in these state variables across the blade row. The axial velocities at inlet and exit have different radial distributions, with a greater radial variation occurring in the axial velocity at exit. The circumferential velocity distributions indicate that the steady flow at inlet has appreciable swirl, with the swirl velocity varying from $0.163 A^*_{\text{Ref}}$ at the hub to $0.208 A^*_{\text{Ref}}$ at $r = 0.746 r_D$. The FEGV essentially removes this swirl, leading to a nearly axial exit flow. Finally, the inlet flow has, by prescription, zero radial velocity, but the exit flow has a small radial velocity component.

7.2 Unsteady Response Predictions

We have determined the unsteady aerodynamic responses of the FEGV, for the ADP operating at the low power setting, to rotor wake excitations at 1, 2, and 3 BPF. These excitations occur at reduced frequencies, $\omega = nN_B\Omega$, of 3.703, 7.406 and 11.109, respectively, and interblade phase angles, $\sigma = -2\pi nN_B/N_V$, of -144 deg, -288 deg and -432 deg. They repeat nN_B times around the wheel and travel toward the FEGV and in the direction of rotor rotation. In addition to occurring at moderate to high reduced frequencies, the wake excitations are highly dependent on radius. These features lead to rather complicated three-dimensional aerodynamic responses. The FEGV unsteady response predictions for the low ADP power setting are given in Figures 14 through 28.

The LINFLUX far-field eigenanalysis determines the axial and radial behaviors of the modal acoustic disturbances far upstream and far downstream of the FEGV. These behaviors depend upon the underlying steady background flows at inlet and exit, the excitation frequency and interblade angle, and the circumferential angular wave numbers, $\bar{m} = -nN_B + mN_V$, of the modal unsteady responses; but, not on the type, amplitude, or radial behavior of the unsteady excitation. In the present effort, the far-field eigenanalysis has been applied to determine the axial eigenvalues and radial shapes of the lowest, radial-order, acoustic modes in the $m = -2, -1, 0, 1, 2$ circumferential modes, for the 1 BPF excitation, and in the $m = -3, ..., 3$ circumferential modes, for the 2 and 3 BPF excitations. Although Some modes can be missed or filtered out by the far-field analysis, usually, such modes are highly attenuated and have little impact on the overall unsteady solution.

We indicate the axial eigenvalues of both acoustic excitations and acoustic responses in our eigenvalue plots. At inlet, the upstream propagating or decaying disturbances are acoustic responses, and the downstream propagating or decaying disturbances are acoustic excitations. At exit, the reverse is true. For the present application to wake/blade-row interactions, the amplitudes of the modal acoustic excitations are set to zero. The amplitudes of the modal acoustic responses are determined by the coupling of the LINFLUX near- and far-field solutions.

1 BPF Wake Excitation

The axial eigenvalues of the modal acoustic disturbances in the far-field of the FEGV for the 1 BPF excitation are shown in Figure 14, where we have indicated the circumferential, m, and radial, μ, mode orders of the the least-damped acoustic response disturbances. For the 1 BPF excitation, all acoustic response modes attenuate. Moreover, because of the swirl in the steady background flow at inlet, there are differences between the axial wave numbers of the attenuating disturbances that occur in different circumferential modes. At 1 BPF, the least-damped response modes at inlet and exit occur at $m, \mu = 0, 0$. These repeat eighteen times around the wheel; travel in the direction of rotor rotation ($\bar{m} = -nN_B + mN_V = -18$); have no radial nodes ($\mu = 0$); and attenuate with increasing distance from the FEGV. The axial eigenvalues of the upstream and downstream traveling 0,0 acoustic responses are $\chi^-_{0,0} = 2.924 + 0.209i$ and $\chi^+_{0,0} = -2.786 + 0.443i$.

The FEGV unsteady velocity and pressure fields resulting from the 1 BPF wake excitation are shown in Figures 15 and 16, respectively. Because plots of the real and imaginary

components of the unsteady field variables indicate similar physical phenomena, only the imaginary components of the unsteady velocity, $Im\{\mathbf{v}\}$, and pressure, $Im\{p\}$, will be depicted in this report. The unsteady velocity vectors, in Figure 15, have been obtained by multiplying the predicted velocities by a scale factor of 12. The velocities at the computational inlet plane are , in general, due to the prescribed wake excitation and the acoustic response of the FEGV. However, for the 1 BPF excitation, the pressure response diminishes strongly with increasing axial distance from the blade row. Thus, the velocity at the inlet plane in Figure 15 is almost entirely due to the wake excitation. The 1 BPF unsteady velocity field shows a strong response at the leading-edge of each blade, and a change in the unsteady flow into one dominated by counter-rotating vortical eddies, in which the flow speeds are low, as it proceeds through the stator blade row.

As noted, the excitation at 1 BPF produces attenuating acoustic responses upstream and downstream of the FEGV. This is clearly indicated by the pressure contours plotted in Figure 16, where the small pressure variations at the computational inlet and exit boundaries are due to acoustic responses that die out with increasing distance from the blade row. The pressure amplitudes of the least-damped 0,0 acoustic responses, at the computational inlet and exit boundaries, are 0.00140 and 0.000689, respectively. The average pressure at the FEGV inlet is 6.101. Thus, the unsteady pressure amplitude of 0.0014 is only 0.023% of the average inlet pressure. The next strongest mode, in terms of amplitude, at inlet is the 1,0 mode, with amplitude 0.00106. The next strongest at exit is the 0,2 mode, which has an amplitude of 0.000181. However, the inlet 1,0 and the exit 0,2 modal responses are more highly damped than the inlet and exit, 0,1, response modes.

The far-field pressures are the response quantities of primary interest in blade-row aeroacoustic response studies. However, we also present surface-pressure response predictions to assist in demonstrating the capabilities and accuracy of the LINFLUX analysis and to provide additional response information, that can be tested experimentally. The unsteady surface pressure distributions acting on the reference or zeroth FEGV blade for the 1 BPF wake excitation are shown, at the J = 4, 10, 16, and 22 radial stations, in Figure 17. Here, the surface pressure responses are given for the modified FEGV blades, which extend from the blade leading edge near $\xi = 0$ to the sharp trailing edge near $\xi = 1.11 c_{ax}$. The trailing edge of the original (blunt-edged) blade occurs near $\xi = c_{ax}$. Since the amplitude, direction and phase of the 1 BPF wake-velocity vary significantly from hub to tip, and this excitation occurs at a moderate reduced frequency, it is difficult to discern any simple radial trends from the surface pressure responses.

2 BPF Wake Excitation

As indicated by the axial eigenvalues, plotted in Figure 18, the 2 BPF wake excitation generates propagating acoustic responses upstream and downstream of the blade row. In particular, three response modes, the 1,0, 1,1, and 1,2 modes, propagate upstream and two, the 1,0 and 1,1 modes, propagate downstream. The axial wave numbers of the 1,0 , 1,1 and 1,2 upstream propagating modes, which travel against the incoming steady flow, are 3.387, 2.862 and 2.049, respectively. Those of the 1,0 and 1,1 downstream propagating modes, which travel with the exiting mean flow, are -1.378 and -0.760. The least-damped upstream, 1,3, and downstream, 1,2, attenuating acoustic responses, at 2 BPF, have axial eigenvalues $\chi^{-}_{1,3} = 1.631 + 0.765i$ and $\chi^{+}_{1,2} = -1.117 + 0.702i$.

The imaginary components of the unsteady velocity and pressure resulting from the 2 BPF excitation are shown in Figures 19 and 20, respectively. To obtain the results in Figure 19, a scale factor of 30 was applied to the predicted velocities. The velocity distribution along the computational inflow boundary consists primarily of the prescribed wake-excitation velocity, but there is also a contribution from the velocity associated with the propagating acoustic response. Again, there are high velocity responses at the leading edge of each vane and a counter-rotating, small-eddy, flow structure extending downstream from the vane leading-edge plane.

The pressure contours in Figure 20 show pressure variations in the vicinities of the computational inflow and outflow boundaries that are due to propagating acoustic response waves. The persistence of such waves is clearly indicated upstream, at the 94% spanwise station, and downstream, at the four reference spanwise stations. A spurious pressure behavior also occurs near the inlet boundary, which is probably due to the errors associated with imposing a wake excitation that is only an approximate solution of the governing unsteady aerodynamic equations. The predictions indicate complicated acoustic responses, both upstream and downstream of the blade row. In addition to the complex radial behavior and the relatively high reduced frequency of the wake excitation, the modal acoustic responses also introduce strong radial gradients.

For the 2 BPF excitation, the amplitudes of the upstream propagating 1,0, 1,1 and 1,2 acoustic response modes at inlet are 0.000775, 0.000177, and 0.00221, and the least-damped 1,3 mode has an amplitude of 0.000830. Thus, the 1,2 mode occurs at the highest amplitude, and this is 0.036% of the average inlet pressure. At exit, the propagating 1,0 and 1,1 modes have amplitudes of 0.00193 and 0.00157, and the least-damped (1,2) mode has an amplitude of 0.000921. There is no clearly dominant acoustic mode at the computational inlet or exit boundaries. In addition, the modes that contribute to the pressure responses at inlet and exit have strong radial variations. Such features make it difficult to provide a simple or convenient interpretation of the far-field acoustic responses, based on contours plotted in Figure 20. An additional complication is introduced by the spurious pressure behavior at inlet. Note that the pressure contour levels for the 2 BPF excitation, in Figure 20, are much lower than those for the 1 BPF excitation, in Figure 16. The 1 BPF excitation produces a stronger unsteady pressure response near the blades, but no sound in the far field. Therefore, the 2 BPF excitation is the more important one aero-acoustically, because it produces pressure responses that persist far from the blade row.

The real and imaginary unsteady surface-pressure responses to the 2 BPF wake excitation are shown in Figure 21. Note that the (ordinate) scale used to plot the surface-pressure response for the 2 BPF excitation is roughly one-fifth of that used for the 1 BPF excitation. The real and imaginary surface pressure responses to the highly three-dimensional 2 BPF wake excitation show no discernable simple trend, but, instead, a relatively complicated radial behavior.

The radial shapes of the propagating acoustic response modes, produced by the 2 BPF excitation, are shown in Figure 22. The propagating response disturbances all occur in the $m = 1$ circumferential mode, i.e., at $\bar{m} = -2N_B + N_V = 9$ or $\sigma = 2\pi\bar{m}/N_V = 72$ deg. Hence, they repeat nine times around the stator blade row, and travel circumferentially counter to the direction of rotor rotation. The propagating modes, including those at $\mu = 0$, all show strong spanwise pressure variations.

We have determined the sound pressure and sound power levels of the 2 BPF acoustic responses. The predicted sound pressure levels, in dB, for the 1,0, 1,1 and 1,2 acoustic response modes at inlet are 110.4, 97.0 and 117.0, respectively. Those for the 1,0 and 1,2 response modes at exit are 117.6 and 115.7. The total sound pressure levels at inlet and exit are 117.9 and 119.8, respectively. The predicted modal and total sound power levels are given in Figure 22, along with the measured power levels (in parentheses), at exit [Hei99]. Considering the various approximations made at this stage of the development of the LINFLUX Prediction System, particularly those associated with modeling the wake excitation, the level of agreement between the predicted and measured data is encouraging. It is also interesting to note that pressure responses at relatively small amplitudes; i.e., at amplitudes that are much less than 0.1% of the average inlet pressure, result in sound power and sound pressure levels on the order of 115 dB.

3 BPF Wake Excitation

As mentioned previously, the 3 BPF response predictiions are not accurate. They are included here for future reference, and because they illustrate important capabilities and limitations of the LINFLUX code. The 3 BPF wake excitation produces an unsteady aerodynamic response in which, as indicated in Figure 23, four acoustic response modes, the 1,0, 1,1, 1,2 and 1,3 modes, propagate upstream and downstream of the FEGV. The axial wave numbers of the 1,0, 1,1, 1,2 and 1,3 upstream propagating modes are 4.441, 3.846, 3.190 and 2.009, respectively; those of the corresponding downstream propagating modes are -2.574, -2.372, -1.782 and -0.369. The least-damped, upstream and downstream, attenuating responses at 3 BPF have axial eigenvalues of $\chi^{-}_{1,4} = 2.252 + 0.924i$ and $\chi^{+}_{2,0} = -4.347 + 1.276i$. A damped 1,4 mode was not captured by the downstream far-field analysis.

The unsteady velocity field associated with the 3 BPF rotor-wake/FEGV interaction is shown in Figure 24, where the predicted velocities have been multiplied by a scale factor of 75. The velocities at the inlet plane are due primarily to the prescribed wake excitation, but departures from the prescribed velocities, due to the response of the FEGV, are evident from the from the behavior of the velocity vectors in the vicinity of the inlet plane. Downstream of the vane leading edge the unsteady flow speeds become quite small, and the velocity vectors are indicative of an unsteady flow that is dominated by counter-rotating, vortical eddies.

The unsteady pressure field generated by the 3 BPF wake/FEGV interaction is depicted in Figure 25. The contours in Figure 25 indicate a very complicated acoustic response upstream of the FEGV, and a spurious response near the computational inlet boundary. There is, however, a well-defined propagating acoustic response downstream of the blade row. The 3 BPF wake excitation varies strongly with radius. It also occurs at a high frequency and at small amplitude. Thus, prescribing this excitation, in terms of a quasi-3D wake model, probably leads to errors that are significant relative to the true aerodynamic response of the FEGV. Such errors are especially severe near the inflow boundary.

The far-field acoustic eigensolutions, i.e., the axial eigenvalues and radial mode shapes, depend upon the frequency and circumferential wave number of the unsteady excitation, but not on the amplitude or radial content of this excitation. The latter do, however, impact the amplitudes of the modal acoustic responses. The LINFLUX predictions indicate that the amplitudes of the upstream propagating 1,0, 1,1, 1,2 and 1,3 modal acoustic responses at

inlet are 0.000505, 0.000278, and 0.000369, and 0.000712, respectively. The strongest damped mode; i.e., the 0,2 mode, has an amplitude of 0.000151. Surprizingly high amplitudes are predicted for the more heavily damped modes, which, again, indicates error in the unsteady solution. At exit, the propagating 1,0, 1,1, 1,2 and 1,3 modes have amplitudes of 0.000207, 0.0000607, 0.000370 and 0.000122, and the damped modes are quite weak. There are no clearly dominant acoustic modes at inlet or exit. The inlet, 1,3 response occurs at the highest amplitude, and this is only 0.012% of the average inlet pressure. Thus, the modes that contribute to the pressure responses at inlet and exit occur at small amplitude, have strong radial variations, and reach their maximum amplitudes at different radial locations.

The unsteady surface-pressure responses of the FEGV to the 3 BPF wake excitation are shown in Figure 26. The real and imaginary surface pressure responses to this highly three-dimensional, excitation show relatively complex radial and axial variations. Note that the pressure (ordinate) scale in Figure 26 is approximately 20% of that used for the 2 BPF surface-pressure response (Figure 21), and only 4% of that used for the 1 BPF response (Figure 17).

The radial shapes of the propagating acoustic response modes, at inlet and exit, for the 3 BPF excitation are shown in Figures 27 and 28, respectively. The propagating modes at 3 BPF occur at an angular wave number of $\bar{m} = -3N_B + N_V = -9$. Hence, as in the 2 BPF case, the model acoustic responses repeat nine times around the wheel; but, the responses at 3 BPF travel in, rather than counter to, the direction of rotor rotation. This difference in the propagation behaviors of the 2 and 3 BPF acoustic responses is also indicated by the orientations of the downstream pressure contours , in Figures 20 and 25.

The predicted sound pressure levels, in dB, for the inlet 1,0, 1,1, 1,2 and 1,3 response modes are 105.5, 100.5, 102.6, and 107.0. Those for the 1,0, 1,1, 1,2 and 1,3 response modes modes at exit are 99.1, 86.4, 101.5 and 92.1, respectively. The total sound pressure levels at inlet and exit are 110.6 and 103.0, respectively. Modal and total, sound power level predictions, for the acoustic responses at inlet and exit, are given in Figures 27 and 28. For the 3 BPF excitation, the predicted sound power levels at exit differ substantially from the measured values [Hei99], which are given in parentheses in Figure 28. It should be noted that a downstream propagating 1,3 response at exit was not detected in the experiment. It is also important to mention that the validity of the experimental results for the 3 BPF excitation is in question.

8. Numerical Results: Take-off Power Setting

We proceed to consider the steady and unsteady flows through the FEGV for the ADP operating at the high power setting. At this setting, the fan rotates at 8,750 rpm and the mass flow rate through the FEGV is 72.8 lb_m/sec. The radial distributions of the measured and analytic, absolute, total temperature, T_T^{abs}, total pressure, P_T^{abs}, and tangential flow angle, $\Omega^{abs} = \tan^{-1}\left(V_\theta^{abs}/V_\xi\right)$, at the rotor exit (stator inlet) are shown in Figure 29. The analytic distributions are prescribed at inlet for the TURBO steady-flow calculation. We did not try to improve the agreement between the analytic and measured values of Ω^{abs} , as this would entail a more detailed curve-fitting procedure, and some additional patience to ensure that TURBO converged to a low-loss, attached, steady solution.

The inflow values of T_T^{abs} and P_T^{abs}, prescribed for the TURBO calculation, are higher than those prescribed at the low power setting, and they are in very good agreement with the measured data. The values of Ω^{abs} are higher over the outer 50% span of the blading, and they are in fair agreement with the data. As indicated in Figure 30, there are differences, particularly near the hub, between the measured and the calculated mean flow velocities. These are due, in part, to the differences between the measured and prescribed values of Ω^{abs}, and to representing the measured viscous flow by an analytic inviscid flow at the same mass flow rate.

Circumferential distributions, over 3 rotor passages, of the analytic, rotor-wake, velocity perturbation, $\tilde{\mathbf{v}}^R = \tilde{v}^R \mathbf{e}_T$, at the midspan leading-edge plane of the stator, are shown in Figure 31. These distributions were determined by post-processing the NASA data for the high power setting. The curves in Figure 31, which are offset by $r/r_D \times 10^3$, describe the behavior of the coefficient, $\tilde{v}^R$, of the wake perturbation velocity. There are also radial variations in the direction, $\mathbf{e}_T$, of this velocity, as indicated by the solid curve for Ω^{rel} in Figure 30. The circumferential location at which the minimum wake velocity occurs, also varies significantly along the span. The velocity profiles in Figure 31 indicate that the wake velocity defect and half-width are relatively large near the hub and tip, and much smaller over the blade midspan region. Also, the wake excitation, at the high power setting, is much stronger than that, depicted in Figure 9, for the low power setting.

Radial distributions of the amplitude, $|v_n^R|$, and phase, $\arg(v_n^R)$, of the first four Fourier components of the analytic wake excitation velocity, at the stator leading edge, are shown in Figure 32. Again, the amplitudes of the Fourier excitations decrease with increasing circumferential mode number, n. Also, the amplitude of the first harmonic excitation shows a strong radial variation over the span, varying from approximately 40 ft/sec at the hub, to 19 ft/sec at midspan, to 33 ft/sec at the tip. The second harmonic varies from 8 ft/sec at the hub to 17 ft/sec at the tip. Large phase variations also occur; e.g., a phase variation of approximately 210 deg for the first harmonic and approximately 420 deg for the second harmonic.

8.1 Steady Background Flow

The steady flow through the fan exit guide vane, for the high power setting, has been calculated by applying the TURBO analysis on the computational grid illustrated in Figure 6.

The radial distributions of absolute total temperature, absolute total pressure and absolute flow angle, indicated by the solid curves in Figure 29, are prescribed at the computational inlet plane, located at $\xi = \xi_- = -0.956$, and the static pressure at the hub is specified, by trial and error, at the exit, $\xi = \xi_+ = 2.045$, such that the calculated mass-flow rate matched that measured in the NASA Glenn experiment. The computed results indicate that the absolute, isentropic, Mach number at inlet increases from 0.306 at the hub ($r = 0.509 r_D$) to 0.569 at $r = 0.847 r_D$, and decreases from 0.569 to 0.517 at the tip. At exit, the isentropic Mach number increases from 0.144 at the hub ($r = 0.569 r_D$) to 0.519 at $r = 0.898 r_D$, and decreases from 0.519 to 0.488 at the tip.

Results from the TURBO calculation are given in Figure 30 and in Figures 33 through 35. The steady pressure field, at the four reference radial stations, is shown in Figure 33, and has characteristics similar to those indicated in Figure 11 for the low power setting. In particular, the steady pressure is nearly constant at the computational inlet and exit boundaries, the pressure variations generated by the FEGV die out within short axial distances from the blade row, and, because of blade loading, there is a small pressure rise across the FEGV.

Steady pressure distributions over the suction and pressure surfaces of the modified vane, i.e., the original vane with a wedge-shaped trailing-edge section added, are shown in Figure 34. These indicate an increase in vane loading from hub to tip. There are flow overspeeds on the suction surface at J =16 and J = 22, leading to peak Mach numbers of 0.989 and 1.130, respectively, just aft of the leading edge. Downstream of the leading-edge region, the peak isentropic Mach numbers at the reference radial stations are approximately 0.516, 0.776, 0.815 and 0.767 at J = 4, 10, 16 and 22, respectively. The axial locations at which these peak Mach numbers occur, generally lie in the vicinity of $\xi = 0.2 c_{\text{ax}}$.

Radial distributions of the steady density, pressure, and velocity, at inlet and exit, are shown in Figure 35. Here, the flow variables are scaled according to the TURBO non-dimensionalization. Thus, the density is scaled by the reference density, $\rho^*_{\text{Ref}} = 0.0764\ \text{lb}_\text{m}/\text{ft}^3$; pressure, by the reference pressure, $P^*_{\text{Ref}} = 2,116.2\ \text{lb}_\text{f}/\text{ft}^2$; and velocity by the reference sound speed $A^*_{\text{Ref}} = 1,116.8$ ft/sec. The pressures and densities at inlet and exit for the high power setting are slightly higher than those for the low power setting, cf. Figure 13; whereas, the inlet axial and circumferential velocities and the exit axial velocities are significantly higher.

The results in Figure 35 indicate that the steady pressure and density are nearly constant at inlet and exit, and there is a slight rise in pressure and density across the blade row. The axial velocities at inlet and exit have different radial distributions, and show strong radial variations, particularly in the axial velocity at exit. The circumferential velocity distributions indicate that the steady inlet flow has a strong swirl. The FEGV removes this swirl, leading to an nearly axial exit flow. Finally, the inlet flow has, by prescription, zero radial velocity, but the exit flow has a small radial velocity component.

8.2 Unsteady Response Predictions

We have determined the unsteady aerodynamic responses of the FEGV, for the ADP operating at the high power or take-off setting, to rotor wake excitations at 1 and 2 BPF. These excitations occur at reduced frequencies, $\omega = n N_B \Omega$, of 3.677 and 7.355, respectively, and interblade phase angles, $\sigma = -2\pi n N_B / N_V$, of -144 deg and -288 deg. Thus, the 1 and 2

BPF wake excitations, at the high power setting, occur at reduced frequencies similar to and interblade phase angles identical to those for the 1 and 2 BPF excitations at the low power setting. These excitations repeat nN_B times around the wheel and travel axially toward the FEGV and circumferentially in the direction of rotor rotation. The wake excitations are highly dependent on radius, as indicated by the curves depicted in Figure 32.

The LINFLUX unsteady response calculations were performed on the 173 x 25 x 41 mesh, shown in Figure 6, and a 36 point, radial, far-field mesh. The far-field eigenanalysis was applied to determine the lowest-order radial acoustic modes in the $m = -2, -1, 0, 1, 2$ circumferential modes, for the 1 BPF excitation, and in the $m = -3, ..., 3$ circumferential modes, for the 2 BPF excitation. The LINFLUX results for the 1 and 2 BPF excitations at the ADP high-power setting are given in Figures 36 through 45. We have also constructed animations of these results, which are described below.

1 BPF Wake Excitation

The axial eigenvalues of the modal acoustic disturbances in the far field, for the 1 BPF excitation, are shown in Figure 36, where we have labeled the circumferential, m, and radial, μ, mode orders of the least-damped acoustic response disturbances. Because of swirl in the steady background flow, the axial wave numbers of the attenuating disturbances in the various circumferential modes, differ. For the 1 BPF excitation, all acoustic response modes attenuate. The least-damped response modes are the 1,0 mode upstream, with $\chi^-_{1,0} = 2.225 + 1.799i$, and the 0,0 mode downstream, with $\chi^+_{0,0} = -2.082 + 1.420i$. Thus, at inlet, the least-damped, 1,0 acoustic response mode repeats twenty seven times around the wheel; travels counter to the direction of rotor rotation ($\bar{m} = -N_B + N_V = 27$); has no radial nodes ($\mu = 0$); and attenuates with increasing axial distance upstream from the FEGV. At exit, the least-damped, 0,0 mode repeats eighteen times around the wheel; travels in the direction of rotor rotation ($\bar{m} = -N_B = -18$); has no radial nodes ($\mu = 0$); and also attenuates with increasing axial distance downstream from the FEGV.

The imaginary components of the FEGV unsteady velocity, $Im\{\mathbf{v}\}$, and pressure, $Im\{p\}$, fields, resulting from the 1 BPF wake excitation, are shown in Figures 37 and 38, respectively. The velocity vectors, depicted in Figure 37, have been obtained by multiplying the predicted velocities by a scale factor of 10. The velocities at the computational inlet plane consist, in general, of the prescribed incoming wake velocity perturbation and a velocity associated with the unsteady pressure response of the FEGV. In this case, although the 1 BPF pressure response attenuates with increasing axial distance from the blade row, it still provides a small contribution to the unsteady velocity at the inlet plane. The unsteady velocity field, depicted in Figure 37, shows a strong response at the leading-edge of each blade. Downstream of the blade leading edges, the velocity amplitudes diminish with axial distance, and the unsteady flow is dominated by counter-rotating, vortical eddies.

The excitation at 1 BPF produces attenuating acoustic responses upstream and downstream of the FEGV. Thus, the pressure variations near the computational inlet and exit boundaries, depicted in Figure 38, are due to acoustic responses that die out with increasing axial distance from the blade row. The amplitudes of the least-damped 1,0 and 0,0 acoustic response modes, at the computational inlet and exit boundaries, are 0.00372 and 0.00242, respectively. The next strongest mode at inlet is the 0,0 mode, with an amplitude

of 0.000583. The next strongest mode at exit is the 0,2 mode, which has an amplitude of 0.000438. However, the exit 0,2 response is more highly damped than the exit 0,1 response. The average steady pressure at the FEGV inlet plane is 2.325. Thus, the unsteady pressure amplitude of 0.00372 is 0.16% of the average inlet pressure.

The unsteady blade-surface pressure distributions resulting from the 1 BPF wake excitation are shown in Figure 39. The surface pressure responses are given for the modified FEGV blades, which extend from the blade leading edge near $\xi = 0$ to the sharp trailing edge near $\xi = 1.11 c_{ax}$. The trailing edge of the original (blunt-edged) blade occurs near $\xi = c_{ax}$. Since the amplitude and phase of the 1 BPF wake excitation vary significantly from hub to tip, cf. Figure 32, and this excitation occurs at a moderate reduced frequency, the surface-pressure response exhibits a relatively complicated spanwise behavior. A disconcerting feature of the results, given in Figure 39, are the large pressure gradients predicted in the tip-region on the blade suction surface, near the trailing edge. This behavior could be due to numerical losses in the steady solution resulting from the prescription of high tip inflow angles.

2 BPF Wake Excitation

The eigensolutions for the 2 BPF excitation, cf. Figure 40, indicate that four modal acoustic responses, the 1,0, 1,1, 1,2 and 1,3 responses, propagate upstream and downstream of the FEGV. The axial wave numbers of the 1,0, 1,1, 1,2 and 1,3 upstream propagating modes at inlet are 7.884, 7.347, 6.705 and 5.909, respectively. Those of the 1,0, 1,1 1,2 and 1,3 downstream propagating modes at exit are -2.434, -2.289, -1.736 and -0.645. Of the captured modes, the least-damped upstream and downstream attenuating responses have axial eigenvalues $\chi^{-}_{2,0} = 3.992 + 3.417i$ and $\chi^{+}_{1,4} = -1.548 + 2.009i$. An attenuating 1,4 mode was not determined by the upstream far-field analysis. Because of the higher mean flow speeds, there are more propagating modes in response to the 2 BPF excitation at the high power setting, than at the low power setting. Also, the axial wave number of the response in a given propagating mode has a higher magnitude.

The imaginary components of the unsteady velocity and pressure resulting from the 2 BPF excitation are shown in Figures 41 and 42. A scale factor of 25 was applied to the predicted velocity, to provide the results given in Figure 41. The velocity distribution along the computational inflow boundary consists of the prescribed wake-excitation velocity, along with a contribution from the velocity associated with the propagating pressure or acoustic response of the FEGV. Again, there are large velocity responses at the leading edge of each vane, particularly near the tip, and the unsteady flow becomes dominated by counter-rotating, vortical eddies as it proceeds through the blade row.

The unsteady pressure responses, depicted in Figure 42, to the 2 BPF wake excitation clearly indicates propagating acoustic responses in the far field of the FEGV. The amplitudes of the upstream propagating 1,0, 1,1, 1,2 and 1,3 acoustic response modes at inlet are 0.00180, 0.000869, 0.00231 and 0.000756. The least-damped captured mode, i.e., the 2,0 mode, has an amplitude of 0.000302 at the computational inflow boundary. The strongest damped mode at inlet is the 0,1 mode, which has an amplitude of 0.000444. At exit, the propagating 1,0, 1,1, 1,2 and 1,3 modes have amplitudes of 0.00281, 0.00223, 0.00246 and 0.00149. The strongest, and least-damped, mode at exit is the 1,4 mode, which has an amplitude of 0.000132. Here,

the exit 1,0 mode occurs at the highest amplitude, and this is 0.12% of the average inlet pressure. There is no clearly dominant acoustic response mode in either the upstream or the downstream regions of the flow. In addition, the modes that contribute to the pressure responses at inlet and exit have large radial variations and reach maximum amplitudes at different radial locations. Such features make it difficult to analyze the acoustic responses of the FEGV, based only on the pressure contours plotted in Figure 42.

The unsteady surface-pressure responses of the FEGV to the 2 BPF wake excitation are shown in Figure 43. The real and imaginary, surface-pressure responses show very complicated radial behaviors. They also show spurious chordwise variations, along the suction surface, near the tip and near the trailing edge, which are indicative of error in the unsteady solution. Again, this spurious behavior may be due to the numerical losses associated with the high, tip, inflow angles prescribed for the TURBO steady-flow calculation.

The radial shapes of the propagating acoustic response modes for the 2 BPF excitation are shown in Figures 44 and 45. The propagating response disturbances occur in the $m = 1$ circumferential mode, i.e., at $\bar{m} = -2N_B + N_V = 9$ or $\sigma_1 = 2\pi\bar{m}/N_V = 72\,\text{deg}$. Hence, they repeat nine times around the wheel and travel circumferentially counter to the direction of rotor rotation. Each of the propagating modes, including those at $\mu = 0$, show strong spanwise pressure variations.

The predicted sound pressure levels, in dB, for the 1,0, 1,1, 1,2 and 1,3 acoustic responses at inlet are 124.8, 119.2, 127.2 and 117.4, respectively. Those for the 1,0, 1,1, 1,2 and 1,3 acoustic responses at exit are 127.4, 126.5, 126.6 and 122.4. The total response sound pressure levels, at inlet and exit are 129.9 dB and 132.1 dB, respectively. The predicted modal and total sound power levels of the acoustic responses at inlet and exit, and, in parentheses, the measured [Hei99] sound power levels of the responses at exit, are given in Figures 44 and 45. The agreement between the analytical and the experimental results for the exit sound power levels is excellent. However, considering the various approximations made at this stage of the development of the LINFLUX Prediction System, this level of agreement must be regarded as somewhat fortuitous. Again, acoustic responses at small amplitudes produce significant sound power and sound pressure levels. At the high power setting, 2 BPF acoustic response amplitudes at approximately 0.1% of the average inlet pressure, produce sound pressure and sound power levels on the order of 120 dB.

Animations

We have constructed animations to illustrate the time-dependent behaviors of the LINFLUX solutions for the 1 and 2 BPF rotor-wake/FEGV interactions, at the high ADP power setting. The animations include a 3D view of the unsteady blade-surface pressures over the entire FEGV, and 2D radial views of the axial velocity and pressure at the 94% spanwise station, over 4 blade passages.

For the 1 BPF excitation, the 3D animation shows an unsteady surface-pressure response, that travels from blade to blade, counter to the direction of rotor rotation. Pressure disturbances at high amplitude occur on the suction surfaces of the blades, near the tip, and travel upstream along the blade surface. On the pressure surface, a high-amplitude response occurs in the middle of the blade, travels outward to the tip, and then upstream to the leading edge.

The 2D axial-velocity animation shows well-defined rotor-wakes that extend from the computational inlet plane to the FEGV leading-edge plane. The wake excitation repeats 18

times around the wheel, and travels circumferentially in the direction of rotor rotation and axially towards the FEGV. Downstream of the FEGV leading-edge plane, the axial velocity perturbations have a very complicated behavior, which depends on the interaction between the prescribed excitation and the FEGV. Within the blade passages, these disturbances show strong blade-to-blade motions that are associated with the unsteady pressure response of the FEGV. Aft of the leading-edge plane, the axial velocity disturbances travel downstream, essentially, in the axial flow direction.

The 1 BPF pressure animation indicates high amplitude pressure variations within each blade passage. These emanate from the blade suction surfaces, and travel into the passage and upstream. Upstream of the FEGV, the pressure disturbances travel counter to the direction of rotor rotation and away from the blade row. Downstream, the pressure disturbances travel in the direction of rotor rotation and, seemingly, towards the blade row. In both regions, the pressure disturbances attenuate with increasing axial distance from the blading.

For the 2 BPF excitation, the 3D animation shows an unsteady surface-pressure response that travels circumferentially, counter to the direction of rotor rotation. On both the blade suction and pressure surfaces, the pressure disturbances travel from trailing to leading edge and from hub to tip.

The 2D, axial velocity animation indicates well-defined rotor wakes from the inlet plane to the vane leading-edge plane. The wake excitation repeats 36 times around the wheel, and travels in the direction of rotor rotation and towards the blade row. This excitation breaks down aft of the vane leading-edge plane, where the axial velocity perturbations become weaker and less organized, and travel downstream, essentially in the axial direction. The 2 BPF, time-dependent, axial-velocity perturbation indicates a much smaller blade-to-blade movement, than that indicated for the 1 BPF excitation.

The 2 BPF, unsteady pressure animation shows strong pressure activity at the blade surfaces and a complicated pressure behavior within the blade passages, where the pressure disturbances generally travel upstream. The behavior of the pressure perturbations changes rather abruptly to that typical of far-field pressure responses just upstream of the FEGV leading-edge plane and just downstream of the trailing-edge plane. The outward propagating pressure responses upstream and downstream of the blade row are strong and well defined. They travel circumferentially counter to the direction of rotor rotation, and axially, away from the blade row. The direction of propagation of the upstream disturbance is at a small angle, measured clockwise, from the negative axial direction, that of the downstream disturbance, is at an angle of roughly 45 deg, measured counter-clockwise, from the positive axial direction.

9. Concluding Remarks

The LINFLUX analysis is being developed to serve as the unsteady aerodynamic component of advanced, aeroacoustic and aeroelastic, design prediction systems for turbomachines. It is based on the linearized Euler equations, an implicit, wave-split, finite-volume analysis to determine the unsteady flow in the near field of a blade row, and eigenanalyses to determine the unsteady flows in the far field. The near- and far-field solutions are coupled at the inflow and outflow boundaries of the near-field domain. To date, the theoretical effort has focused on developing the unsteady aerodynamic model and the near- and far-field solution procedures; implementing these into two- and three-dimensional, unsteady-flow codes; validating these codes for benchmark unsteady flows; and, under the present effort, demonstrating the 3D code, for aeroacoustic design, via application to realistic wake/blade-row interactions.

As noted previously, the application of LINFLUX to predict the unsteady aerodynamic response of a blade row to a wake excitation involves the use of four codes: TIGER, to generate a 3D H-grid; AWAKEN, to define steady and unsteady inflow conditions; TURBO, to determine the steady background flow; and LINFLUX to determine the unsteady flow. Under the present effort, we have applied this system of codes to predict steady and unsteady flows through the exit guide vane of a NASA/PW advanced ducted propulsor. The unsteady flows are excited by circumferential nonuniformities in the flow exiting the fan rotor, which are due primarily to the rotor wakes. We have considered two ADP power settings, a low power or approach setting and a high power or take-off setting, and have applied LINFLUX to predict the aerodynamic responses of the FEGV to Fourier components, at multiples of the blade passing frequency, of the rotor wake excitations. The latter are based on velocity measurements, taken, in an axial plane, downstream of the rotor, at NASA Glenn Research Center.

A number of liberties were taken in modeling the actual rotor-wake/FEGV interaction, including geometric changes to the vanes and the aft duct, and modifications to the circumferentially-averaged, measured, rotor-exit flow. The major approximations are those associated with modeling the wake excitation. The circumferential wake velocity distributions have been modified in an attempt to remove endwall phenomena and provide a more or less classical wake excitation from hub to tip. In addition, empirical correlations have been applied to estimate the strength and circumferential distribution of the viscous wake excitation at the FEGV midspan leading-edge plane, based on the velocity measurements taken upstream. The estimated velocity distribution at this reference axial plane is used to determine the complex amplitudes of the Fourier wake excitations that are input, at inlet, to the inviscid LINFLUX code. Finally, a quasi-3D or strip-theory approximation has been employed, in which, at each radial station, the inlet wake velocity perturbation is assumed to be an axially and circumferentially convected disturbance that carries no pressure or density.

We have presented numerical results that describe the flows through the FEGV. These include AWAKEN results for the steady inflow conditions and the wake-excitation velocity; TURBO predictions for the steady background flow; and LINFLUX predictions for the near-field unsteady velocity and pressure, the modal acoustic responses at inlet and exit, and the modal and total, sound pressure and sound power, levels in the far field. Unsteady response predictions, for the low power setting, have been determined for rotor-wake excitations at

1, 2, and 3 BPF. However, the 3 BPF results are not accurate. Unsteady predictions, for the high power setting, have been determined for wake excitations at 1 and 2 BPF. In this case, a converged LINFLUX solution could not be determined for the 3 BPF excitation. The difficulties at 3 BPF are believed to be due to the errors associated with representing the highly radially dependent 3 BPF wake disturbances in a quasi-3D manner.

The steady background flows and the Fourier wake excitations vary significantly with radius. Also, the 1 and 2 BPF excitations occur at sufficiently high frequencies that they produce propagating or lightly attenuated acoustic responses that are highly dependent on radius. These features make it difficult to assess the LINFLUX solutions, particularly in the absence of any previous analytical results or detailed near-field response data. The results for the 1 and 2 BPF excitations, at both power settings, indicate complicated three-dimensional, fluid-dynamic, response phenomena. However, for the most part, these results appear to be very reasonable.

The LINFLUX predictions, for the two power settings, indicate that the 1 BPF wake excitations produce attenuating acoustic responses, upstream and downstream of the FEGV and, hence, no sound far from the blade row. The 2 BPF excitations produce propagating acoustic responses, in both far-field regions, that carry energy away from the blade row. The 2 BPF excitations occur at similar reduced frequencies. However, the steady flow speeds are higher and the wake excitations are stronger at the high power setting. As a result, more propagating response modes occur at this setting. These travel away from the blade row at higher axial wave numbers, and they produce higher sound levels. At the low power setting, three modal responses propagate upstream and two propagate downstream. At the high setting, four modal responses propagate upstream and four propagate downstream. The propagating acoustic responses at 2 BPF repeat nine times around the wheel, and travel counter to the direction of the rotor rotation and away from the blade row.

The propagating modes all have strong radial variations and significant sound power levels. In particular, at the low power setting, the 2 BPF excitation produces an acoustic response at exit having a predicted total sound power level of 111.8 dB. The sound power levels of the 1,0 and 1,1 modal responses are 110.5 and 106.0 dB. The corresponding measured values are 114.8, 110.4 and 112.8 dB, respectively. At the high power setting, the 2 BPF excitation produces a predicted total sound power level of 125 dB at exit. The predicted sound power levels for the exit 1,0, 1,1, 1,2 and 1,3 propagating acoustic responses are 121.1, 120.4, 119.2 and 112.5 dB respectively. The corresponding measured power levels are 126.0, 122.1, 121.4, 119.4 and 110.1 dB, respectively. The 2 BPF excitations produce acoustic response amplitudes that are on the order of only 0.1% of the average inlet pressure, but such responses produce acoustic power levels on the order of 110 to 120 dB. With the exception of those for the 1,1 mode at the low power setting, the predicted and measured modal sound power levels at exit are in excellent agreement. However, although very encouraging, this level of agreement must be regarded as somewhat fortuitious, because of the various approximations made in applying LINFLUX, particularly those associated with modeling the wake excitation.

Animations of the the LINFLUX axial-velocity solutions, for the the 1 and 2 BPF wake excitations at the high power setting, indicate well defined wake excitations extending from the computational inflow boundary to just upstream of the FEGV midspan leading-edge plane. Downstream of this axial plane, the wake excitations break down and the axial

velocity perturbations exhibit very complicated behaviors. Within the blade passages, the axial-velocity disturbances show strong blade-to-blade motions. Aft of the blade row, weaker, less-organized, axial velocity perturbations travel downstream, essentially in the mean-flow (axial) direction. The 1 BPF pressure animation shows attenuating pressure responses that travel counter to the direction of rotor rotation, upstream of the FEGV, and in the direction of rotor rotation, downstream. The 2 BPF pressure animation indicates strong, well-defined, propagating pressure responses upstream and downstream of the FEGV. These travel counter to the direction of rotor rotation and away from the blade row.

Based upon the validation studies conducted to date and the present application to fan-wake/FEGV interactions, it appears that the 3D LINFLUX analysis will be a useful prediction capability for determining the unsteady pressure responses of blade rows to the various sources of unsteady excitation. Therefore, it should be a valuable resource for aeroacoustic design, and for understanding the flow physics associated with blade-row noise generation. The results given in this report are based on an early application of the LINFLUX Prediction System to realistic wake/blade-row interactions. It is anticipated that solutions will improve as experience is gained in using the various codes. More importantly, with further development, the computational resources required by the TURBO and LINFLUX analyses will decrease, and various aspects of the unsteady flow model will be improved.

The major limitations, associated with applying the present version of LINFLUX to wake/blade-row interactions, are those related to the wake excitation model. At present, hub and duct phenomena are ignored, the effects of viscous diffusion are modeled empirically, and the wake excitation, at inlet, is represented as a quasi-3D, convected, velocity disturbance. Future work should be focused on improving these aspects of the wake/blade-row interaction analysis. Improved representations of the excitation could be achieved by having sufficient experimental or computational data on the rotor-exit flow to accurately specify the thermodynamic properties and the axial behavior of the wake excitation at the stator inlet. In addition, although it would entail a major effort, a viscous version of LINFLUX would enable the effects of wake diffusion to be accommodated within the unsteady aerodynamic analysis.

Several computational issues should also be investigated to improve the performance of the LINFLUX code. These include improvements to the far-field eigenanalysis to ensure that all important acoustic response modes are captured. It would also be of value to develop a far-field analysis for variable radii ducts. Finally, the development of a parallel version of LINFLUX would allow the grids, needed to resolve unsteady flows at high subsonic Mach numbers and/or high excitation frequencies, to be readily accommodated.

References

[CW93] J. P. Chen and D. L. Whitfield, *Navier-Stokes Calculations for the Unsteady Flowfield of Multi-stage Turbomachinery*, Paper 93-0676, AIAA 31st Aerospace Sciences Meeting and Exhibit, Reno, Nevada, January 11–14, 1993.

[FV93] T. H. Fransson and J. M. Verdon, *Standard Configurations for Unsteady Flow through Vibrating Axial-Flow Turbomachine Cascades*, Unsteady Aerodynamics, Aeroacoustics and Aeroelasticity of Turbomachines and Propellers, edited by H. M. Atassi, Springer-Verlag, New York, 1993, pp. 859–889.

[GA97] V. V. Golubev and H. M. Atassi, *Acoustic-Vorticity Modes in an Annular Duct with Mean Vortical Swirling Flow*, Paper 97–1695–CP, 3rd Joint CEAS/AIAA Aeroacoustics Conference (18th AIAA Aeroacoustics Conference), Atlanta, Georgia, May 12-14, 1997.

[Han99] D. B. Hanson, June 1999, unpublished document.

[HC93] K. C. Hall and W. S. Clark, *Linearized Euler Predictions of Unsteady Aerodynamic Loads in Cascades*, AIAA Journal **31** (1993), no. 3, 540–550.

[HCL94] K. C. Hall, W. S. Clark, and C. B. Lorence, *A Linearized Euler Analysis of Unsteady Transonic Flows in Turbomachinery*, Transactions of the ASME: Journal of Turbomachinery **116** (1994), no. 3, 477–488.

[Hei99] L. J. Heidelberg, June 1999, personal communication.

[HL93] K. C. Hall and C. B. Lorence, *Calculation of Three-Dimensional Unsteady Flows in Turbomachinery Using the Linearized Harmonic Euler Equations*, Transactions of the ASME: Journal of Turbomachinery **115** (1993), no. 4, 800–809.

[HSR91] D. L. Huff, T. W. Swafford, and T. S. R. Reddy, *Euler Flow Predictions for an Oscillating Cascade Using a High Resolution Wave-Split Scheme*, Paper 91–GT–198, ASME International Gas Turbine and Aeroengine Congress and Exposition, Orlando, Florida, June 3–6, 1991.

[HV91] K. C. Hall and J. M. Verdon, *Gust Response Analysis for Cascades Operating in Nonuniform Mean Flows*, AIAA Journal **29** (1991), no. 9, 1463–1471.

[Jan89] J. M. Janus, *Advanced 3-D CFD Algorithm for Turbomachinery*, Ph.D. thesis, Mississippi State University, Mississippi State, Mississippi, May 1989.

[JHW92] J. M. Janus, H. Z. Horstman, and D. L. Whitfield, *Unsteady Flowfield Simulation of Ducted Prop-Fan Configurations*, Paper 92–0521, AIAA 30th Aerospace Sciences Meeting and Exhibit, Reno, Nevada, January 6-9, 1992.

[Ker77] J. L. Kerrebrock, *Small Disturbances in Turbomachine Annuli with Swirl*, AIAA Journal **15** (1977), no. 6, 794–803.

[Kou95] K. A. Kousen, *Eigenmode Analysis of Ducted Flows with Radially Dependent Axial and Swirl Components*, Paper 95–160–CP, First Joint CEAS/AIAA Aeroacoustics Conference (16th AIAA Aeroacoustics Conference), Munich, Germany, June 12-15, 1995.

[MG84] R. K. Majjigi and P. R Gliebe, *Development of a Rotor Wake/Vortex Model*, NASA CR 174849, June 1984.

[MG98] J. G. Marshall and M. B. Giles, *Some Applications of a Time-Linearized Euler Method to Flutter & Forced Response in Turbomachinery*, Unsteady Aerodynamics and Aeroelasticity of Turbomachines, edited by T. H. Fransson, Kluwer Academic Publishers, 1998, pp. 225–240.

[MV95] M. D. Montgomery and J. M. Verdon, *A Linearized Unsteady Euler Analysis for Turbomachinery Blade Rows Using an Implicit Wave-Split Scheme*, Unsteady Aerodynamics and Aeroelasticity of Turbomachines, edited by Y. Tanida and M. Namba, Elsevier, Amsterdam, 1995, pp. 143–160.

[MV97] M. D. Montgomery and J. M. Verdon, *A 3D Linearized Unsteady Euler Analysis for Turbomachinery Blade Rows*, NASA CR 4770, prepared under Contract NAS3–26618 for NASA Lewis Research Center, March 1997.

[MV98] M. D. Montgomery and J. M. Verdon, *A 3D Linearized Unsteady Euler Analysis for Turbomachinery Blade Rows, Part 1: Aerodynamic and Numerical Formulations; Part 2: Unsteady Aerodynamic Response Predictions*, Unsteady Aerodynamics and Aeroelasticity of Turbomachines, edited by T. H. Fransson, Kluwer Academic Publishers, 1998, pp. 427–464.

[Nam87] M. Namba, *Three Dimensional Flows*, AGARD Manual on Aeroelasticity in Axial-Flow Turbomachines, *Vol. 1*, Unsteady Turbomachinery Aerodynamics, edited by M. F. Platzer and F. O. Carta, AGARD AG–298, March 1987.

[Neu97] R. J. Neubert, April 1997, personal communication.

[Pod97] G. Podboy, May 1997, personal communication.

[PV00] D. Prasad and J. M. Verdon, April 2000, unpublished notes.

[Roe81] P. L. Roe, *Approximate Riemann Solvers, Parameter Vectors and Difference Schemes*, Journal of Computational Physics **43** (1981), 357–372.

[SLH+94] T. W. Swafford, D. H. Loe, D. L. Huff, D. H. Huddleston, and T. S. R. Reddy, *The Evolution of NPHASE: Euler/Navier-Stokes Computations of Unsteady Two-Dimensional Cascade Flow Fields*, Paper 94–1834, AIAA 12th Applied Aerodynamics Conference, Colorado Springs, Colorado, June 20–23, 1994.

[Smi72] S. N. Smith, *Discrete Frequency Sound Generation in Axial Flow Turbomachines*, R&M 3709, British Aeronautical Research Council, London, England, UK, March 1972.

[Sre96] K. Sreenivas, *Linearized Euler Analysis of Turbomachinery*, Ph.D. thesis, Mississippi State University, December 1996.

[SS91] B. K. Soni and M. H. Shih, *TIGER: Turbomachinery Interactive Grid GenERation*, Proceedings of the Third International Conference on Numerical Grid Generation in CFD, Barcelona, Spain, June 1991.

[TA98] C. K. W. Tam and L. Auriault, *The Wave Modes in Ducted Swirling Flows*, Journal of Fluid Mechanics **371** (1998), 1–20.

[TE99] D. A. Topol and W. Eversman, *TFaNS Tone Fan Noise Design/Prediction System, Vol. II: User's Manual*, NASA CR 1999-208883, March 1999.

[Top00] D. A. Topol, *Technical Documentation for the AWAKEN Wake/Turbulence Postprocessor*, NASA CR, to be published, 2000.

[TS62] J. M. Tyler and T. G. Sofrin, *Axial Flow Compressor Noise Studies*, SAE Transactions **70** (1962), 309–332.

[UV91] W. J. Usab, Jr. and J. M. Verdon, *Advances in the Numerical Analysis of Linearized Unsteady Cascade Flows*, Transactions of the ASME: Journal of Turbomachinery **113** (1991), no. 4, 633–643.

[VC84] J. M. Verdon and J. R. Caspar, *A Linearized Unsteady Aerodynamic Analysis for Transonic Cascades*, Journal of Fluid Mechanics **149** (1984), 403–429.

[Ver00] J. M. Verdon, *User Instructions for the LINFLUX prediction System*, NASA CR, to be published, 2000.

[VMC99] J. M. Verdon, M. D. Montgomery, and H. A. Chuang, *Development of a Linearized Unsteady Euler Analysis with Application to Wake/Blade-Row Interactions*, NASA CR 1999–208879, March 1999.

[VMK95] J. M. Verdon, M. D. Montgomery, and K. A. Kousen, *Development of a Linearized Unsteady Euler Analysis for Turbomachinery Blade Rows*, NASA CR 4677, June 1995.

[VTM82] C. S. Ventres, M. A. Theobald, and W. D. Mark, *Turbofan Noise Generation, Volume 1: Analysis*, NASA CR 167952, July 1982.

[WJS88] D.L. Whitfield, J.M. Janus, and L.B. Simpson, *Implicit Finite Volume High Resolution Wave Split Scheme for Solving the Unsteady Three-Dimensional Euler and Navier-Stokes Equations on Stationary or Dynamic Grids*, Report MSSU–EIRS–ASE–88–2, Mississippi State Engineering and Industrial Research Station, 1988.

List of Figures

Figure 18: Axial eigenvalues, $\chi = \beta + i\kappa_\xi$, of acoustic disturbances far upstream and far downstream of the FEGV operating at the low power (approach) setting and subjected to an unsteady excitation at 2 BPF ($\omega = 7.406$ and $\sigma = -288.0\,\text{deg}$).

Figure 19: Imaginary component of unsteady velocity at four radial stations (scale factor = 30) for the FEGV operating at the low power setting and subjected to the 2 BPF wake excitation.

Figure 20: Imaginary component of unsteady pressure at four radial stations for the FEGV operating at the low power setting and subjected to the 2 BPF wake excitation.

Figure 21: Unsteady surface-pressure distributions at four radial stations for the FEGV operating at the low power setting and subjected to the 2 BPF wake excitation.

Figure 22: Radial pressure modes and modal and total sound power levels of the propagating acoustic responses in the far field of the FEGV operating at the low power (approach) setting and subjected to the 2 BPF ($\omega = 7.406$ and $\sigma = -288.0\,\text{deg}$) wake excitation.

Figure 23: Axial eigenvalues, $\chi = \beta + i\kappa_\xi$, of acoustic disturbances far upstream and far downstream of the FEGV operating at the low power (approach) setting and subjected to an unsteady excitation at 3 BPF ($\omega = 11.109$ and $\sigma = -432.0\,\text{deg}$).

Figure 24: Imaginary component of the unsteady velocity at four radial stations (scale factor = 75) for the FEGV operating at the low power setting and subjected to the 3 BPF wake excitation.

Figure 25: Imaginary component of the unsteady pressure at four radial stations for the FEGV operating at the low power setting and subjected to the 3 BPF wake excitation.

Figure 26: Unsteady surface-pressure distributions at four radial stations for the FEGV operating at the low power setting and subjected to the 3 BPF wake excitation.

Figure 27: Radial pressure modes and modal and total sound power levels for the propagating acoustic responses far upstream of the FEGV operating at the low power (approach) setting and subjected to the 3 BPF ($\omega = 11.109$ and $\sigma = -432.0\,\text{deg}$) wake excitation.

Figure 28: Radial pressure modes and modal and total sound power levels for the propagating acoustic responses far downstream of FEGV operating at the low power (approach) setting and subjected to the 3 BPF ($\omega = 11.109$ and $\sigma = -432.0\,\text{deg}$) wake excitation.

Figure 29: Steady flow properties far upstream of the FEGV operating at the high power (take-off) setting.

Figure 30; Absolute and relative steady velocities at the rotor exit (FEGV inlet) for the high power setting.

Figure 31: Analytic, rotor-wake, tangential velocity perturbation at the FEGV midspan leading-edge plane ($\xi = 0$) for the high power (take-off) setting.

Figure 32; Fourier components of the analytic, rotor-wake, excitation velocity, $\tilde{v}^{R}$, for the high power setting.

Figure 33; Steady pressure field at four radial stations for the FEGV operating at the high power setting.

Figure 34: Steady surface-pressure distributions at four radial stations for the FEGV operating at the high power setting.

Figure 35: Steady flow properties at the computational inlet and exit planes for the FEGV operating at the high power setting.

Figure 36: Axial eigenvalues, $\chi = \beta + i\kappa_{\xi}$, of acoustic disturbances far upstream and far downstream of the FEGV operating at the high power (take-off) setting and subjected to an unsteady excitation at 1 BPF ($\omega = 3.677$ and $\sigma = -144.0\,\mathrm{deg}$)

Figure 37: Imaginary component of the unsteady velocity at four radial stations (scale factor = 10) for the FEGV operating at the high power setting and subjected to the 1 BPF wake excitation.

Figure 38: Imaginary component of the unsteady pressure at four radial stations for the FEGV operating at the high power setting and subjected to the 1 BPF wake excitation.

Figure 39: Unsteady surface-pressure distributions at four radial stations for the FEGV operating at the high power setting and subjected to the 1 BPF wake excitation.

Figure 40: Axial eigenvalues, $\chi = \beta + i\kappa_{\xi}$, of acoustic disturbances far upstream and far downstream of the FEGV operating at the high power (take-off) setting and subjected to an unsteady excitation at 2 BPF ($\omega = 7.355$ and $\sigma = -288.0\,\mathrm{deg}$).

Figure 41: Imaginary component of the unsteady velocity at four radial stations (scale factor = 25) for the FEGV operating at the high power setting and subjected to the 2 BPF wake excitation.

Figure 42: Imaginary component of the unsteady pressure at four radial stations for the FEGV operating at the high power setting and subjected to the 2 BPF wake excitation.

Figure 43: Unsteady surface-pressure distributions at four radial stations for the FEGV operating at the high power setting and subjected to the 2 BPF wake excitation.

Figure 44: Radial pressure modes and modal and total sound power levels for the propagating acoustic responses far upstream of the FEGV operating at the high power (take-off) setting and subjected to the 2 BPF ($\omega = 7.355$ and $\sigma = -288.0\,\mathrm{deg}$) wake excitation.

Figure 45: Radial pressure modes and modal and total sound power levels for the propagating acoustic responses far downstream of the FEGV operating at the high power (take-off) setting and subjected to the 2 BPF ($\omega = 7.355$ and $\sigma = -288.0\,\mathrm{deg}$) wake excitation.

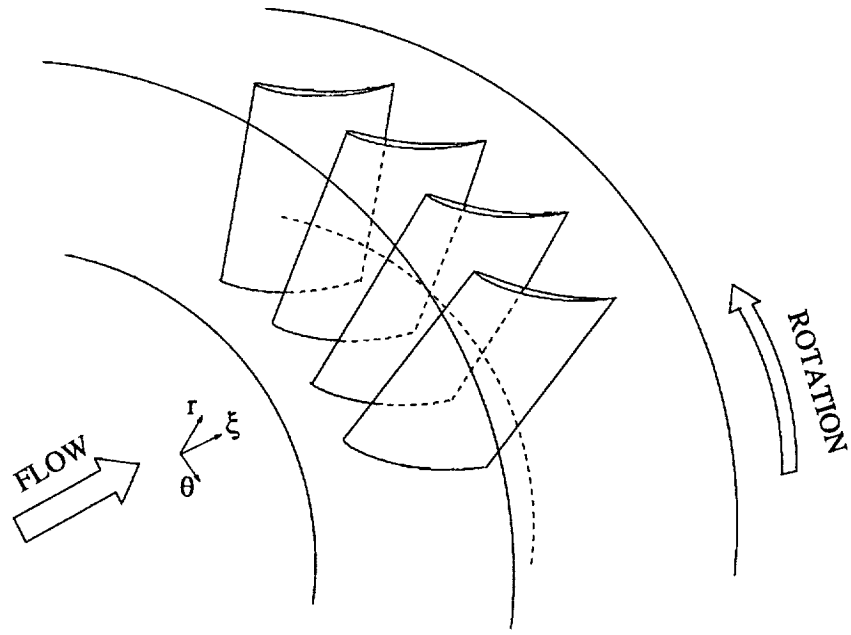

Figure 1: Rotating axial compressor blade row operating within an annular duct.

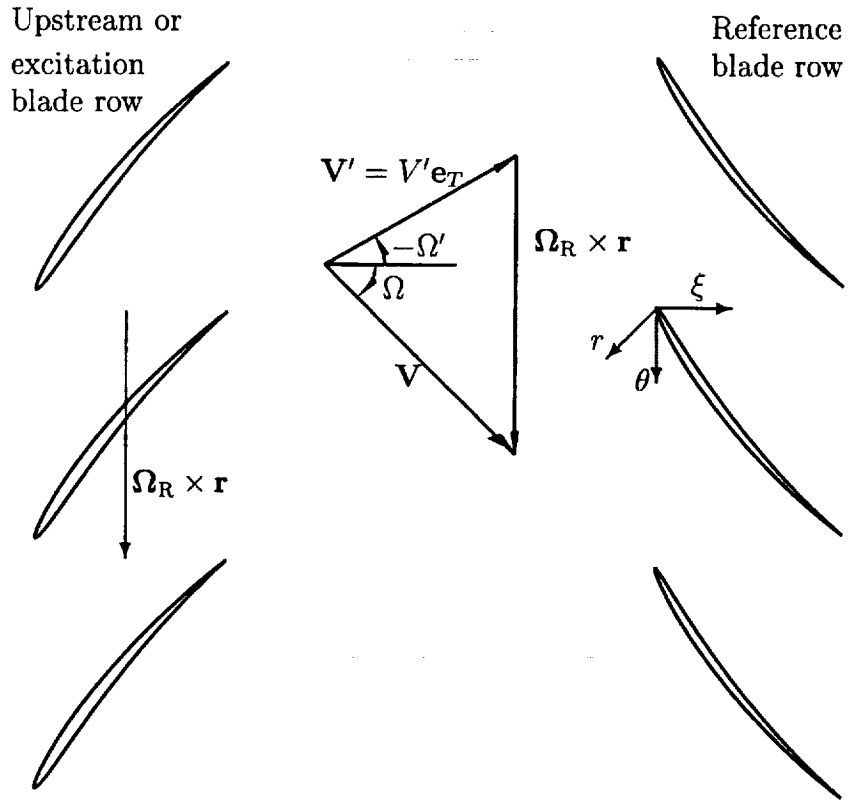

Figure 2: Nomenclature for wake/blade-row interaction.

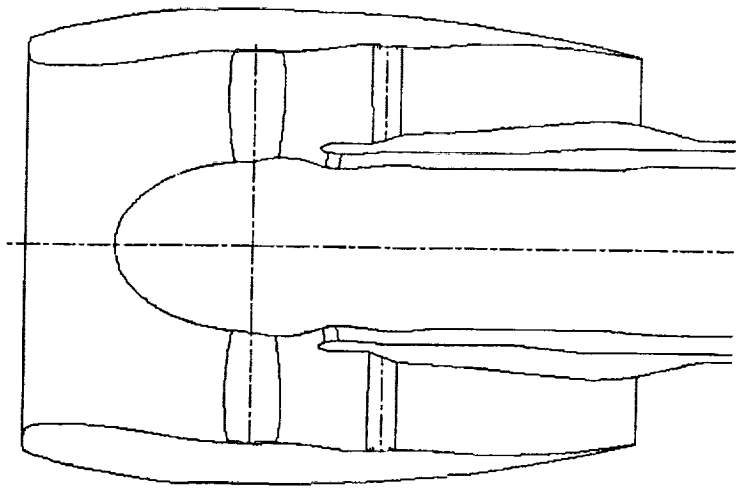

Figure 3: Schematic of the PW/NASA 22 inch advanced ducted propulsor (ADP).

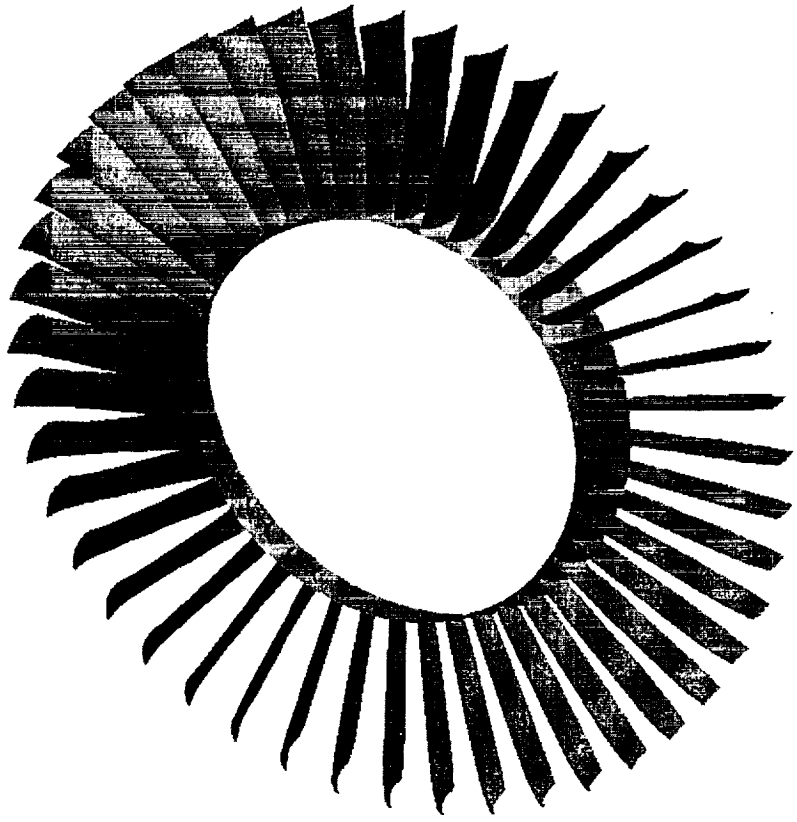

Figure 4: Fan exit guide vane (FEGV) of the 22 inch ADP.

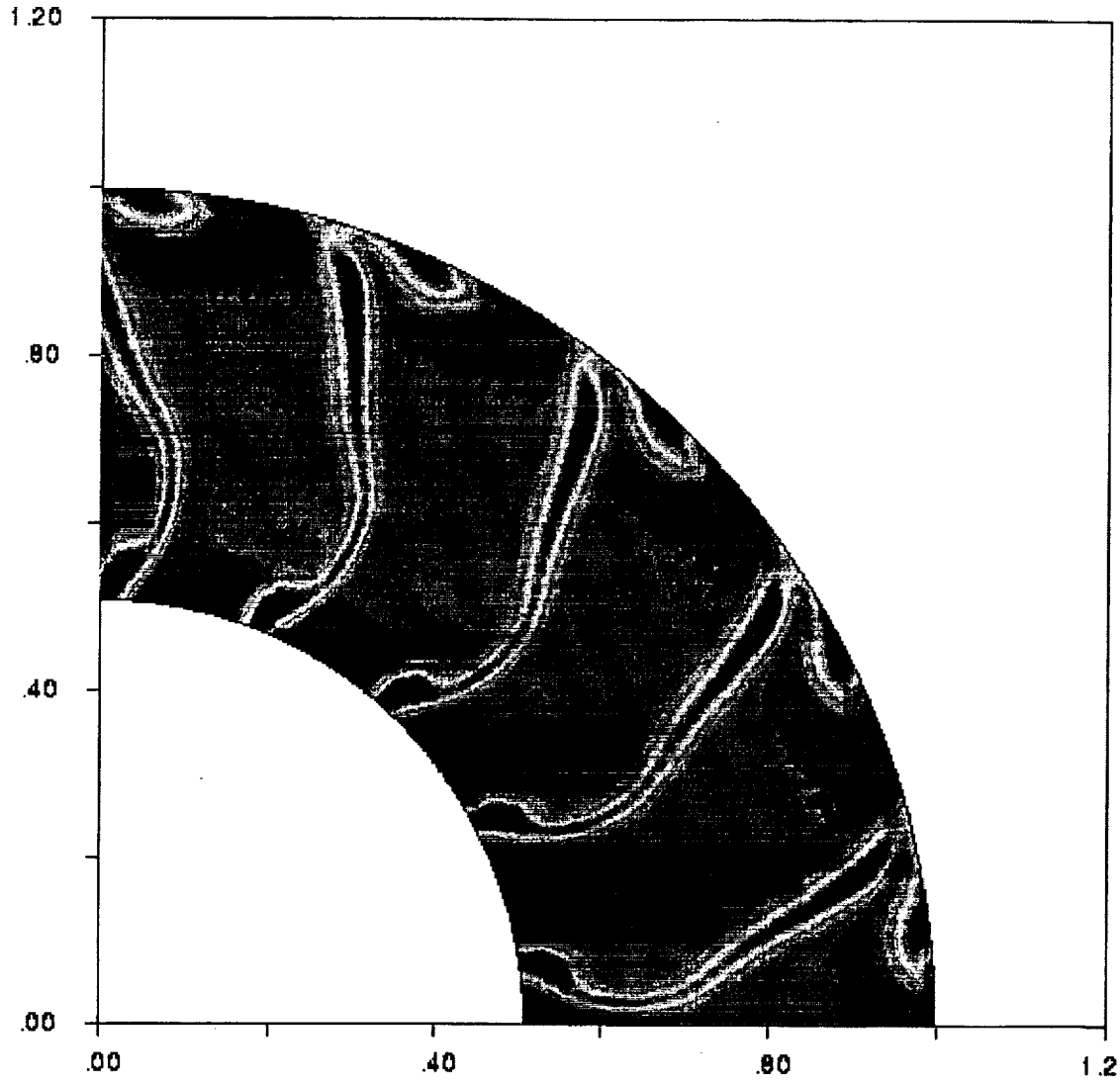

Figure 5: Measured, rotor-exit (FEGV-inlet) flow for the low power setting.

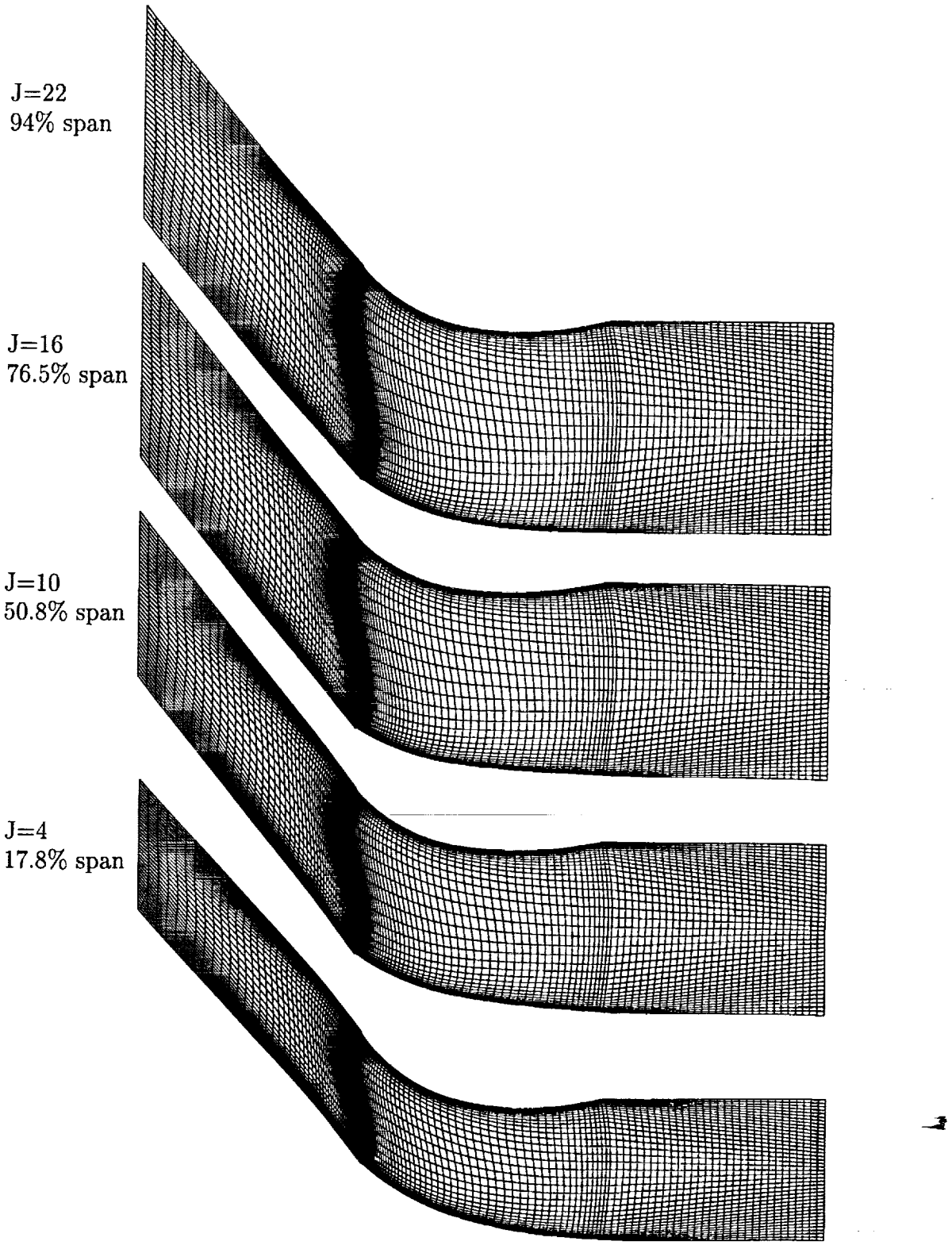

Figure 6: FEGV computational grid at 4 radial stations.

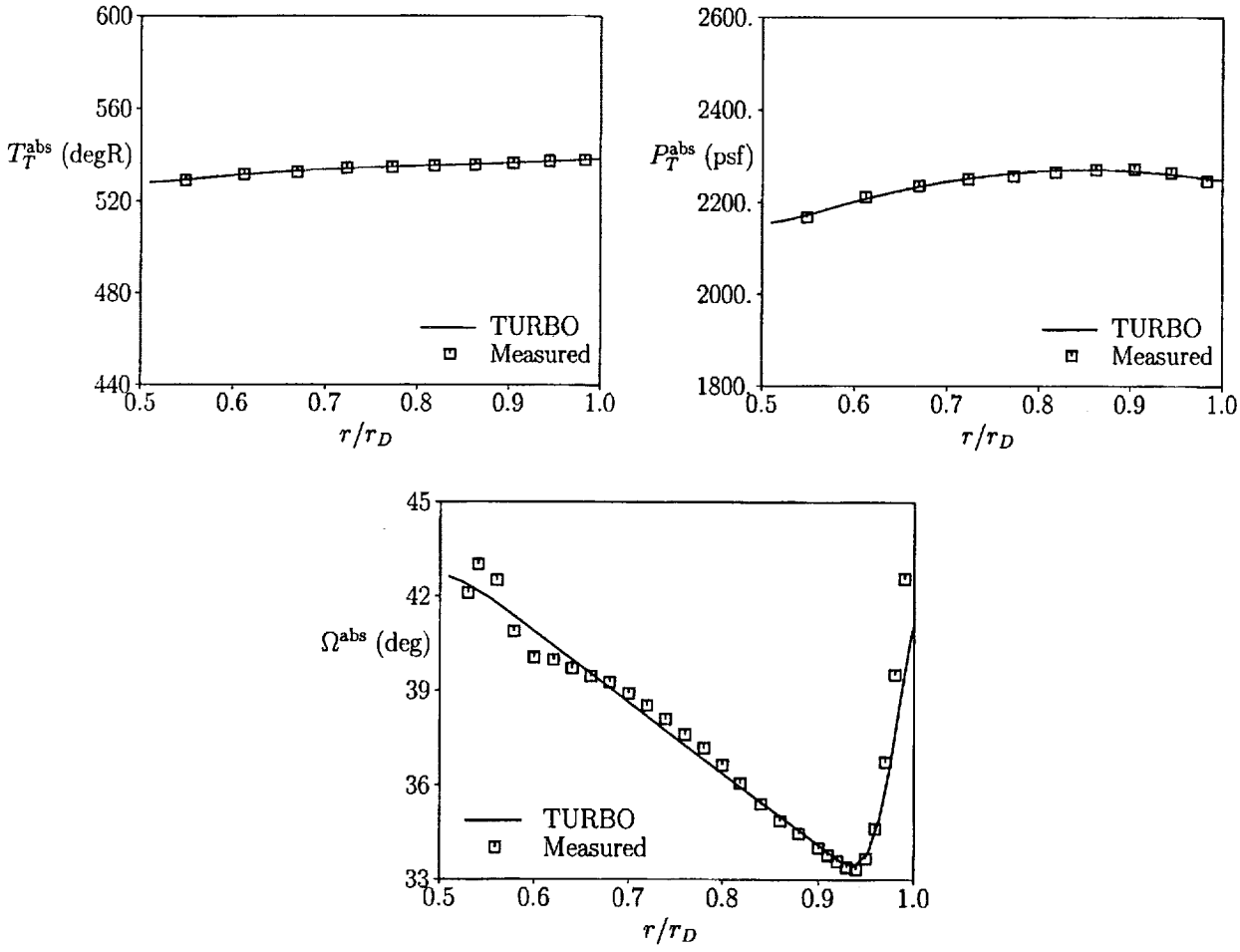

Figure 7: Steady flow properties far upstream of the FEGV operating at the low power (approach) setting.

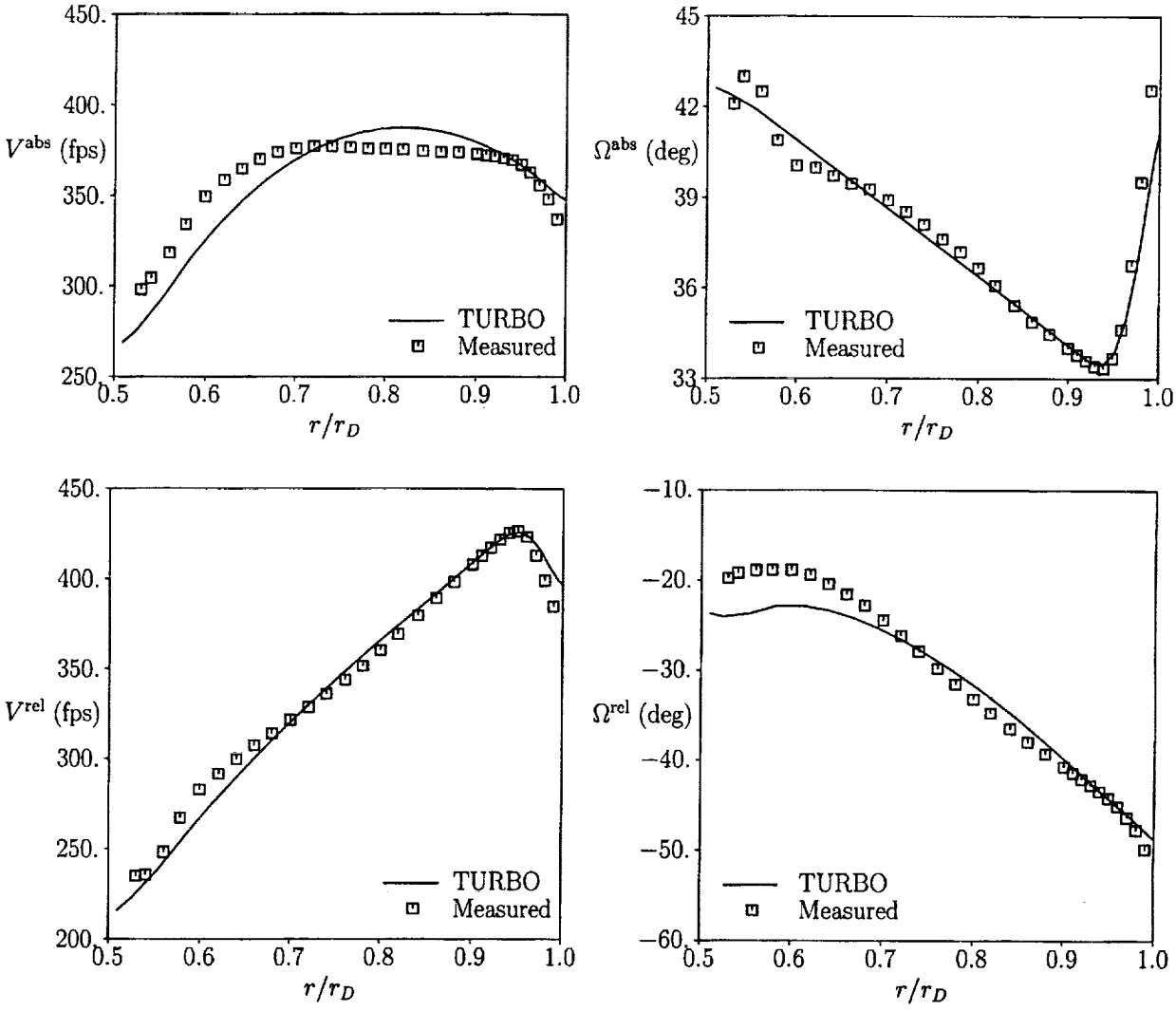

Figure 8: Absolute and relative steady velocities at the rotor exit (FEGV inlet) for the low power setting.

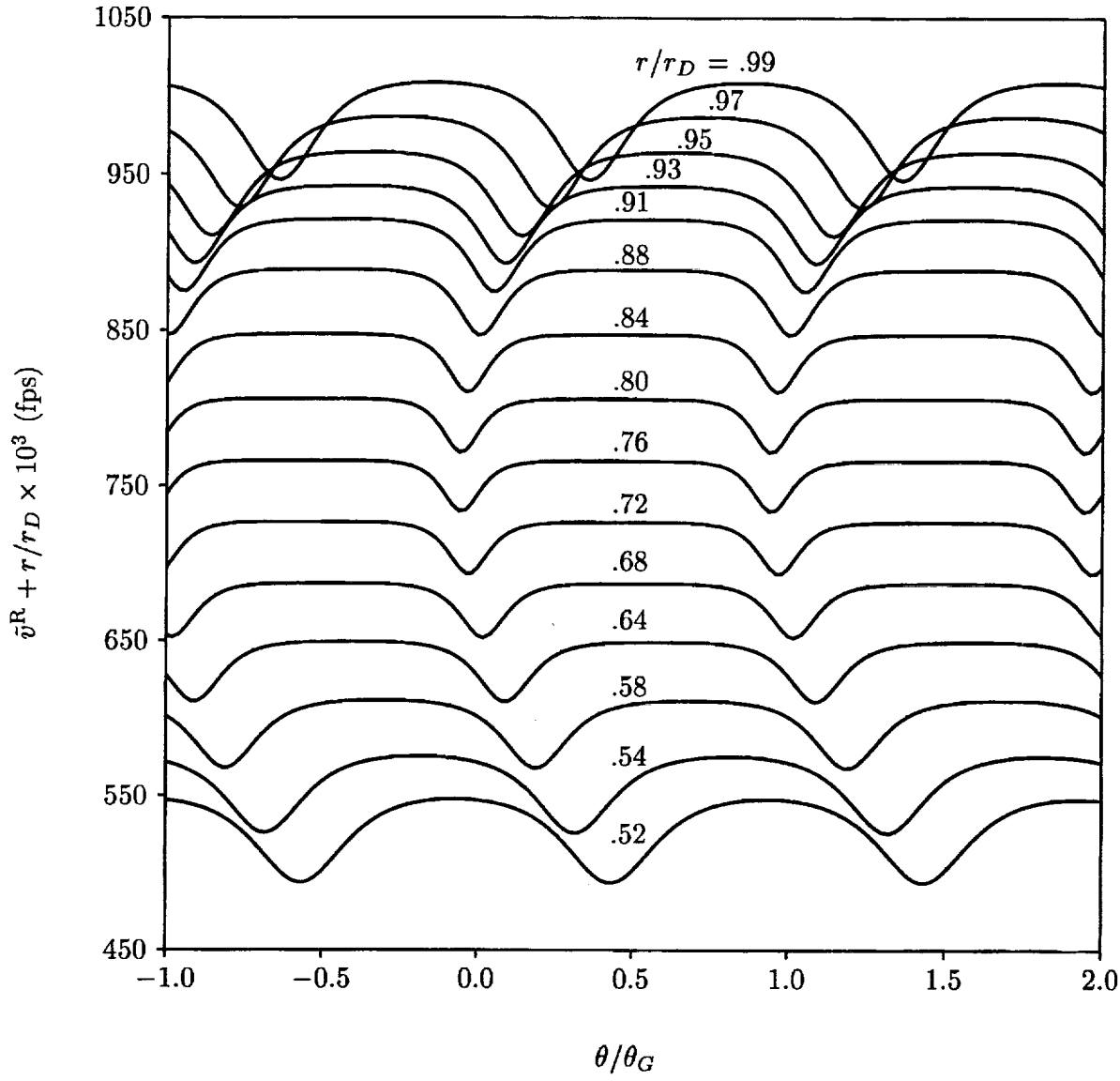

Figure 9: Analytic, rotor-wake, tangential velocity perturbation at the FEGV midspan leading-edge plane ($\xi = 0$) for the low power (approach) setting.

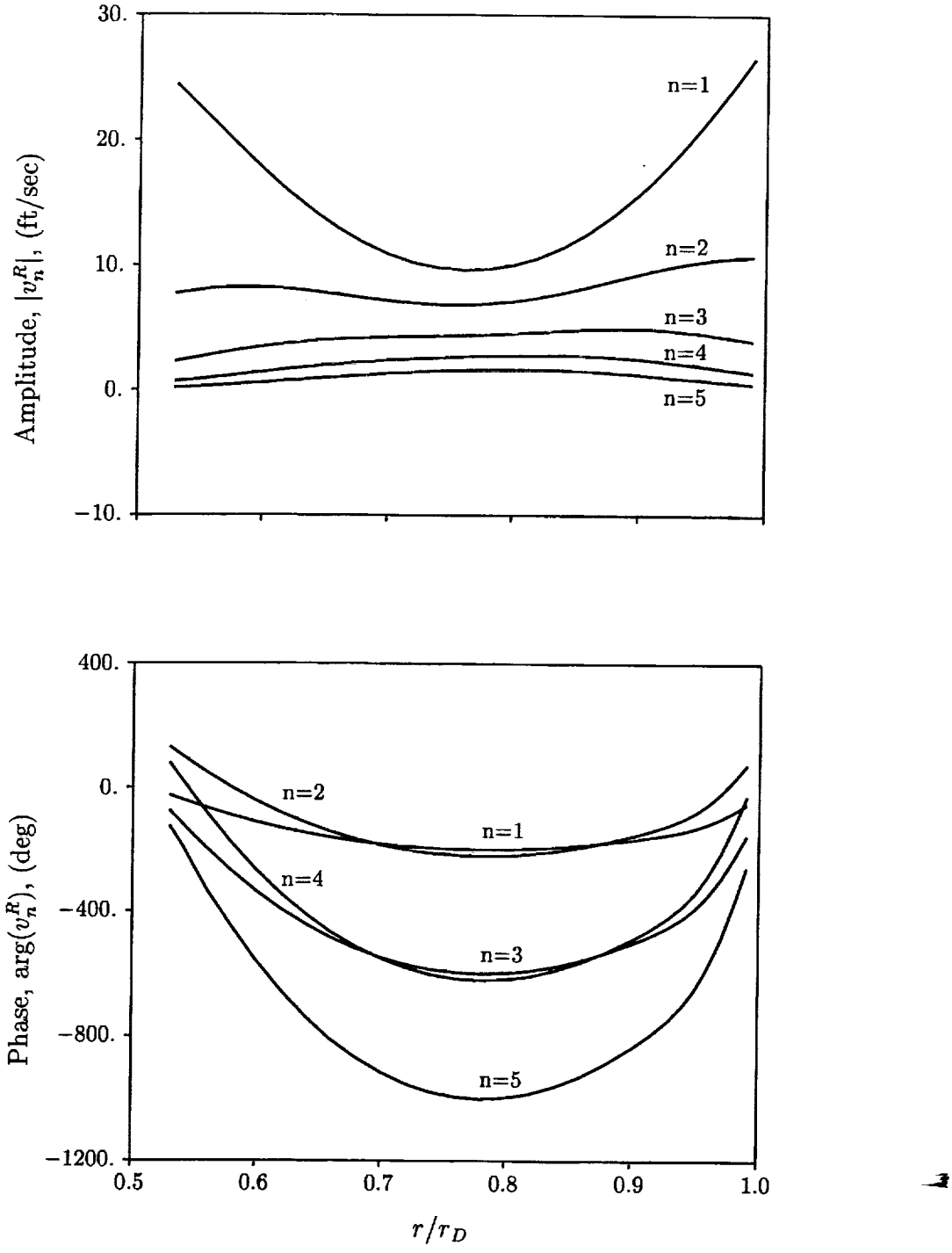

Figure 10: Fourier components of the analytic, rotor-wake excitation velocity, $\tilde{v}^{\mathrm{R}}$, for the low power setting.

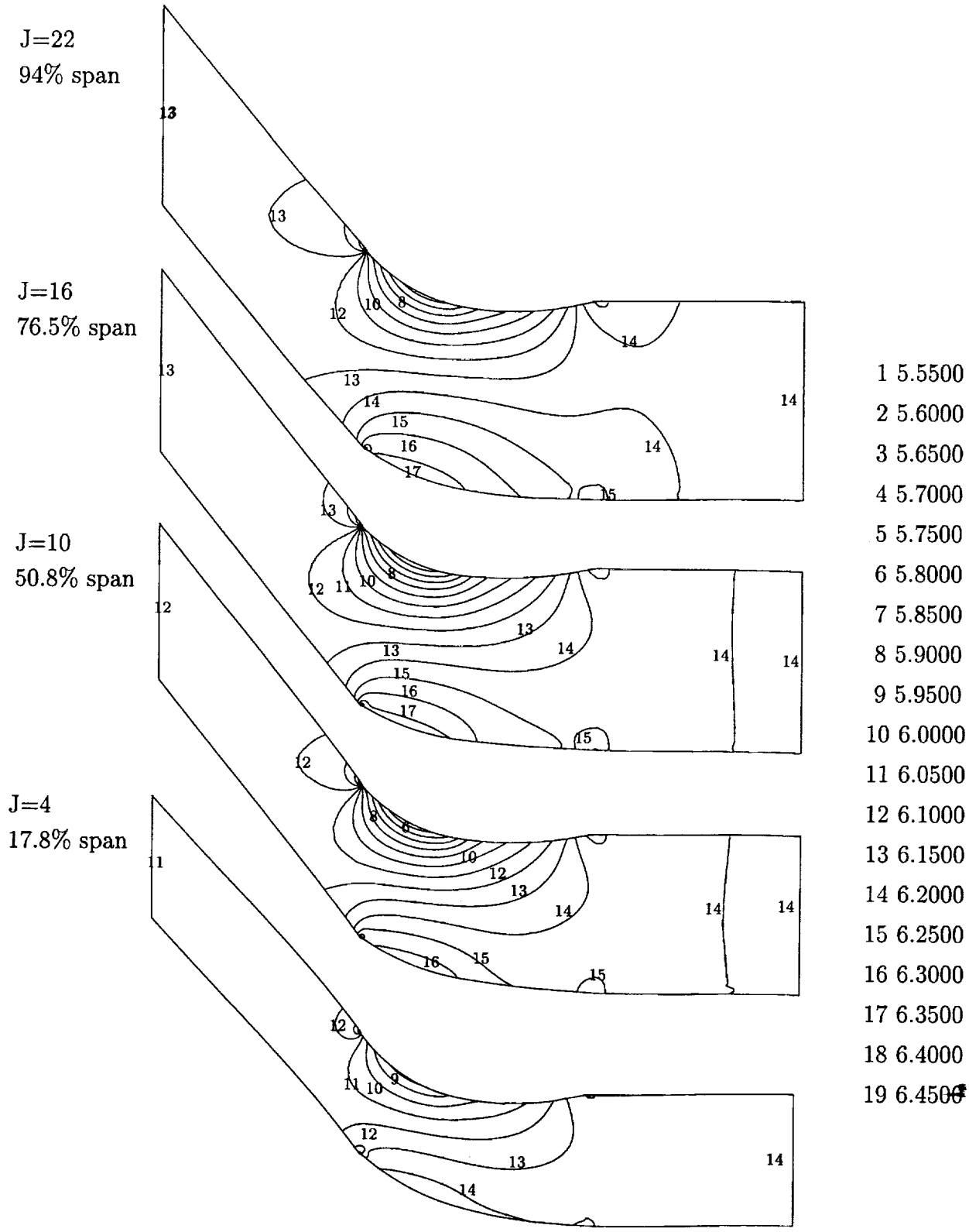

Figure 11: Steady pressure field at four radial stations for the FEGV operating at the low power setting.

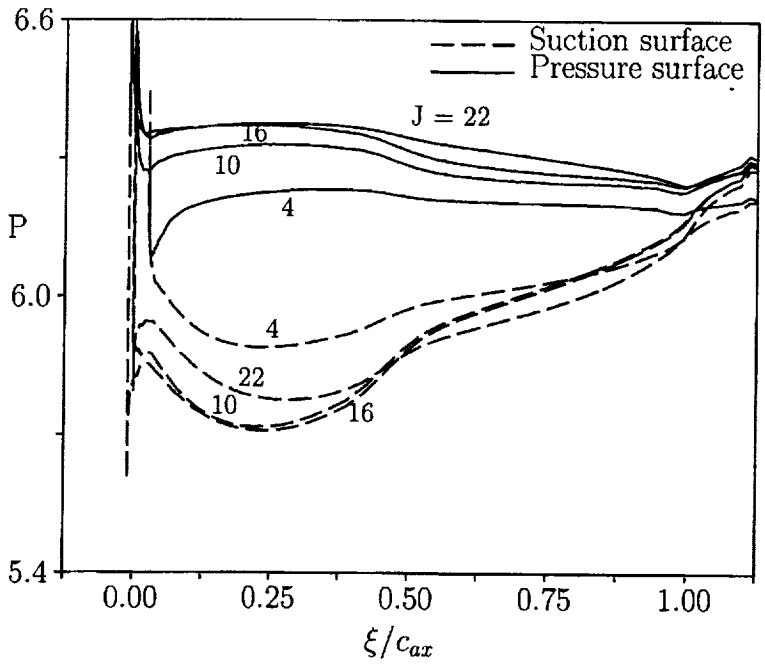

Figure 12: Steady surface-pressure distributions at four radial stations for the FEGV operating at the low power setting.

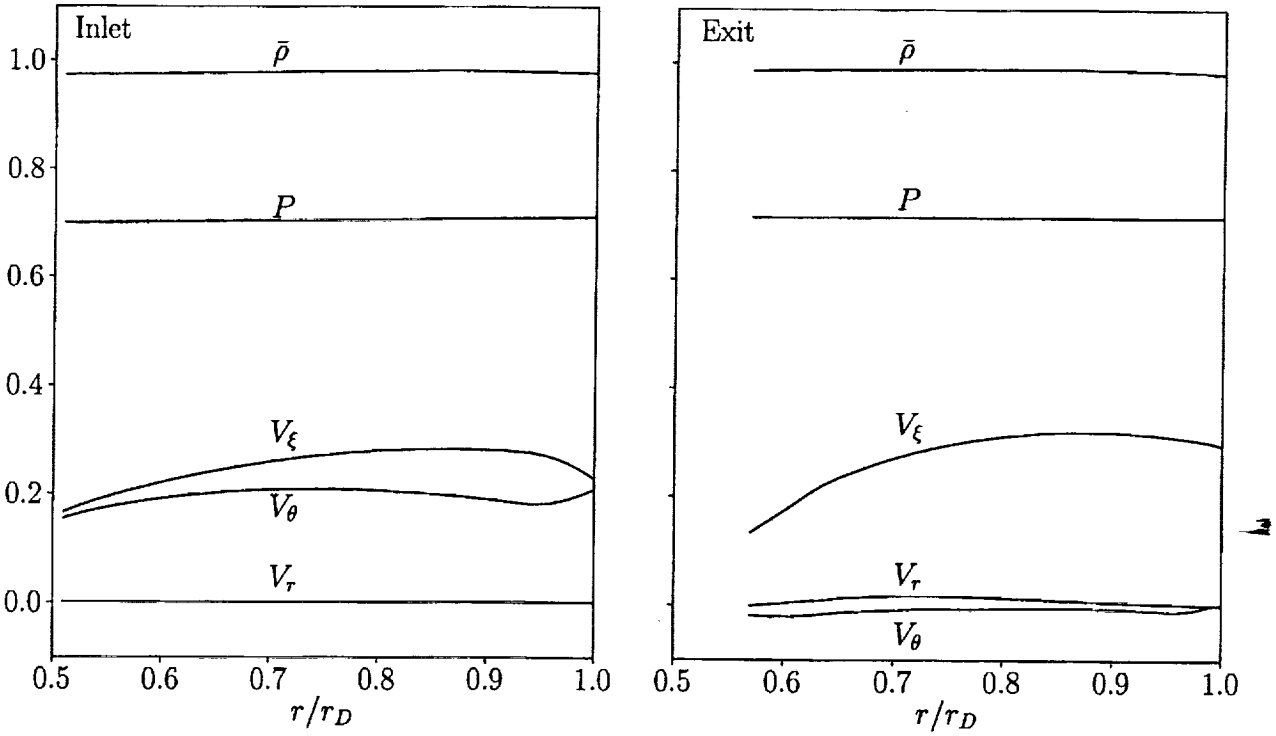

Figure 13: Steady flow properties at the computational inlet and exit planes for the FEGV operating at the low power setting.

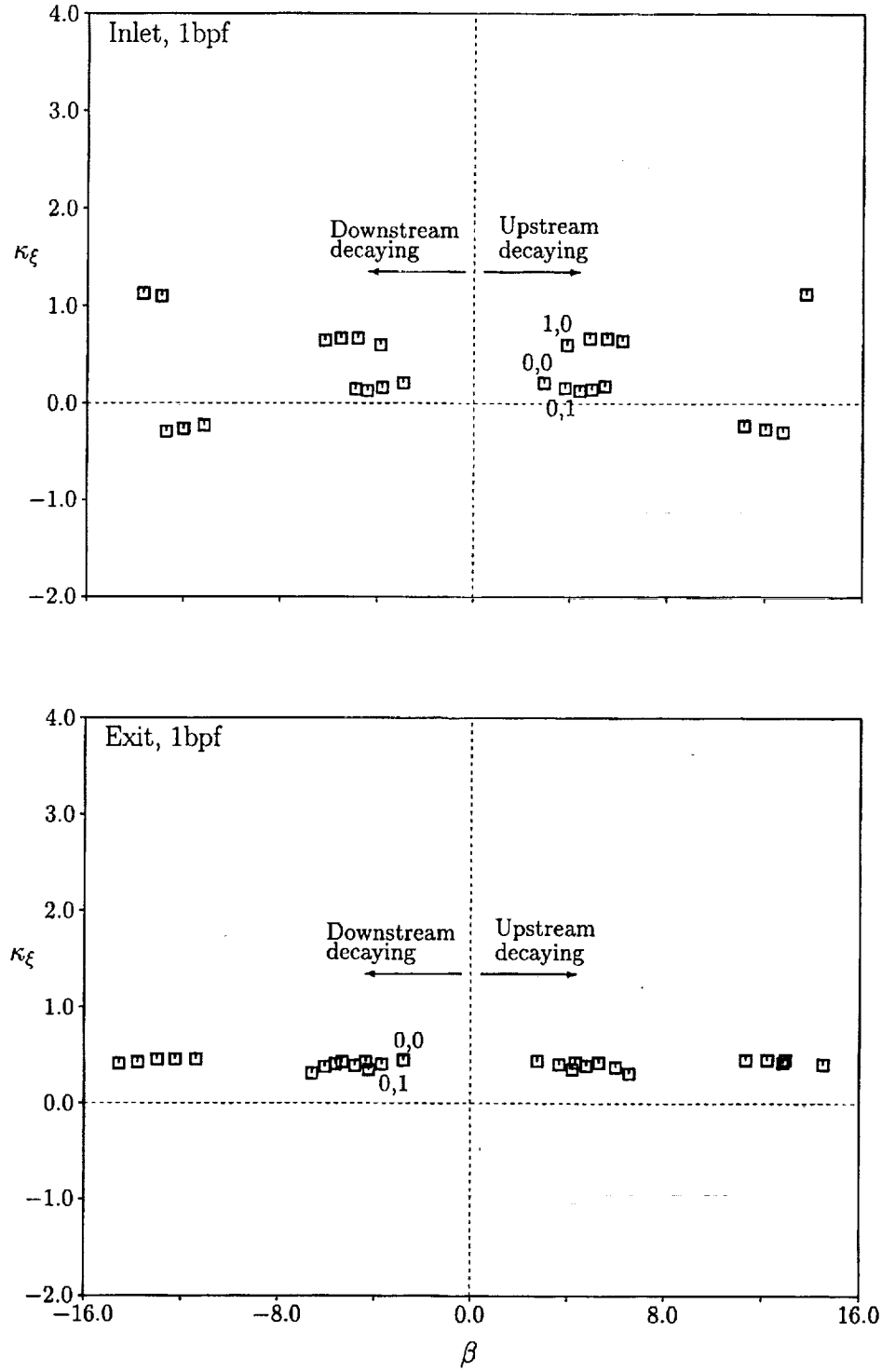

Figure 14: Axial eigenvalues, $\chi = \beta + i\kappa_\xi$, of acoustic disturbances far upstream and far downstream of the FEGV operating at the low power (approach) setting and subjected to an unsteady excitation at 1 BPF ($\omega = 3.703$ and $\sigma = -144.0$ deg).

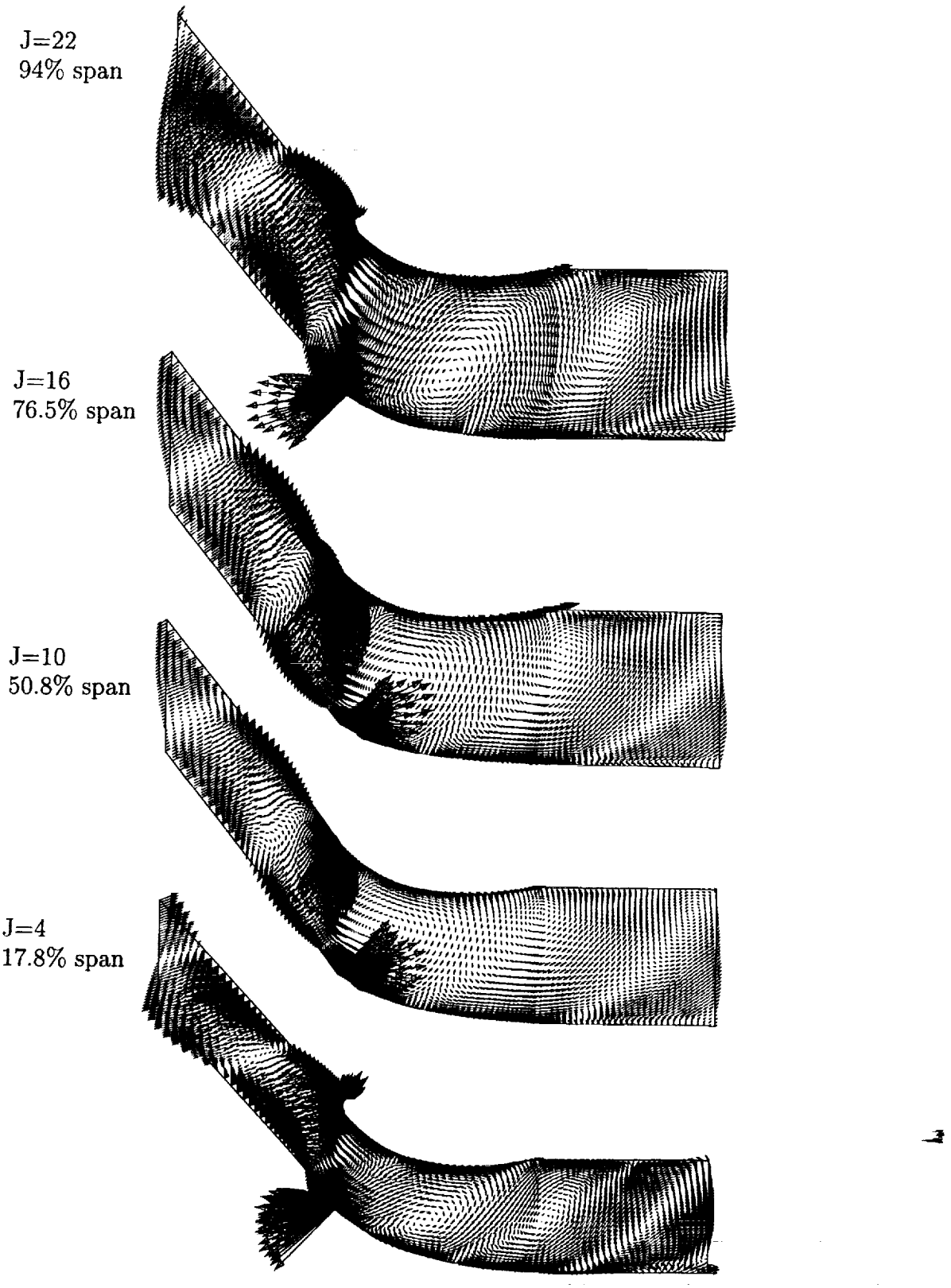

Figure 15: Imaginary component of the unsteady velocity at four radial stations (scale factor = 12) for the FEGV operating at the low power setting and subjected to the 1 BPF wake excitation.

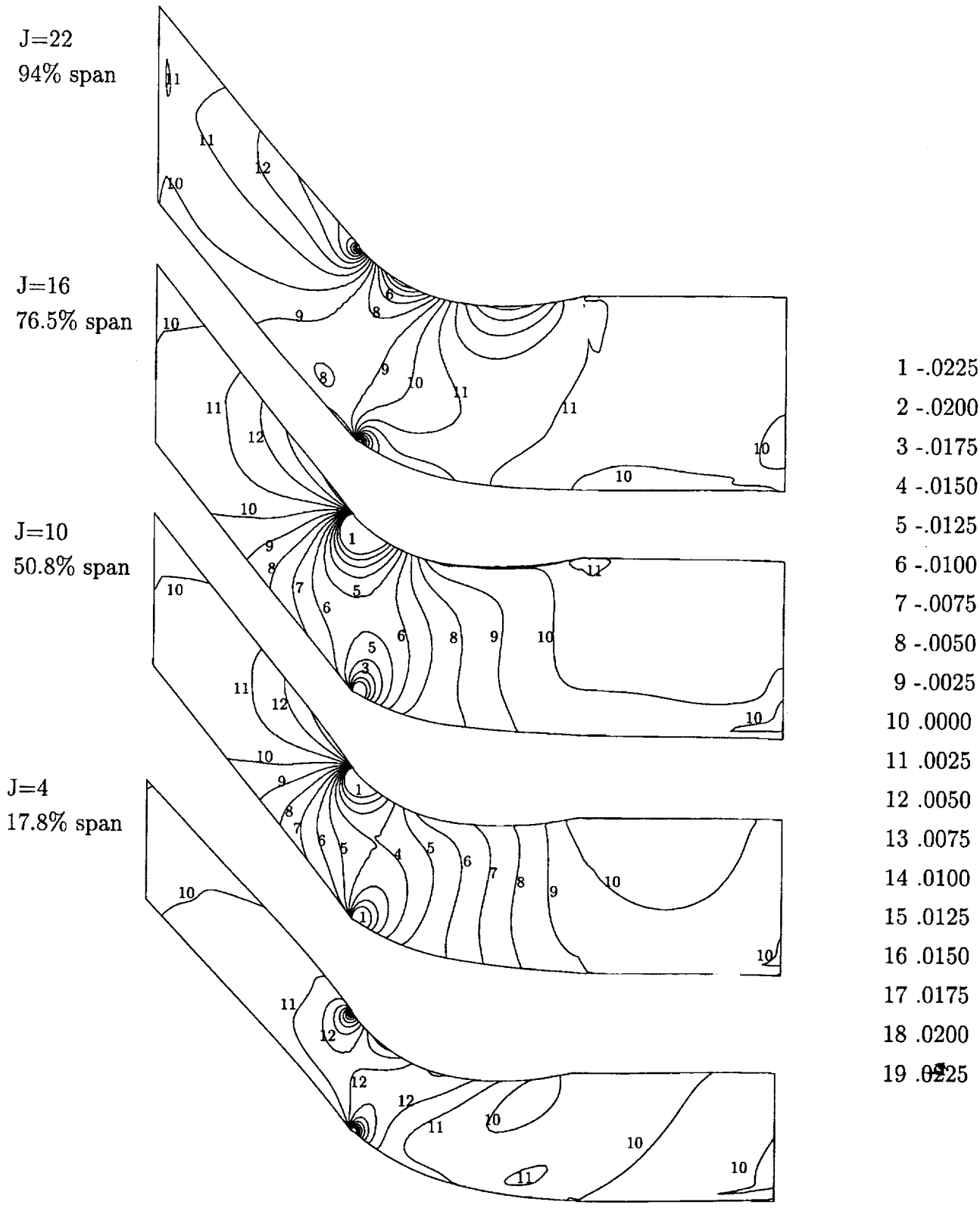

Figure 16: Imaginary component of the unsteady pressure at four radial stations for the FEGV operating at the low power setting and subjected to the 1 BPF wake excitation.

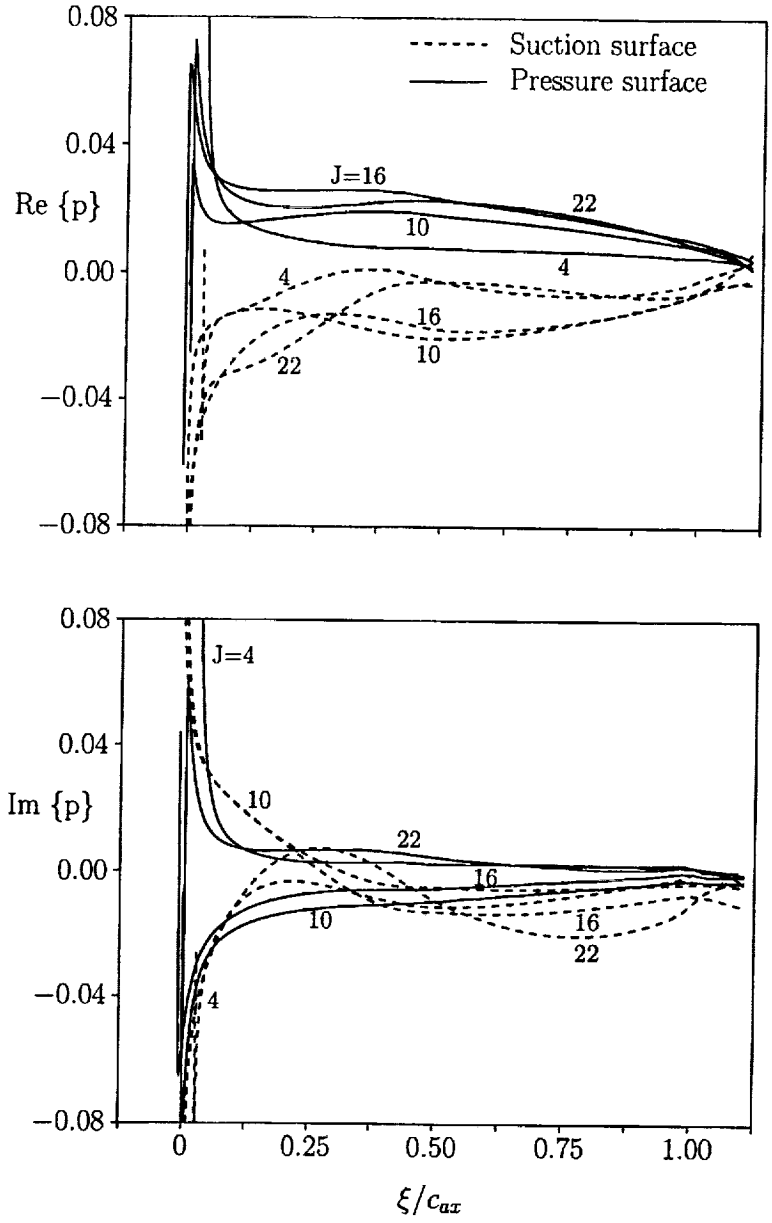

Figure 17: Unsteady surface-pressure distributions at four radial stations for the FEGV operating at the low power setting and subjected to the 1 BPF wake excitation.

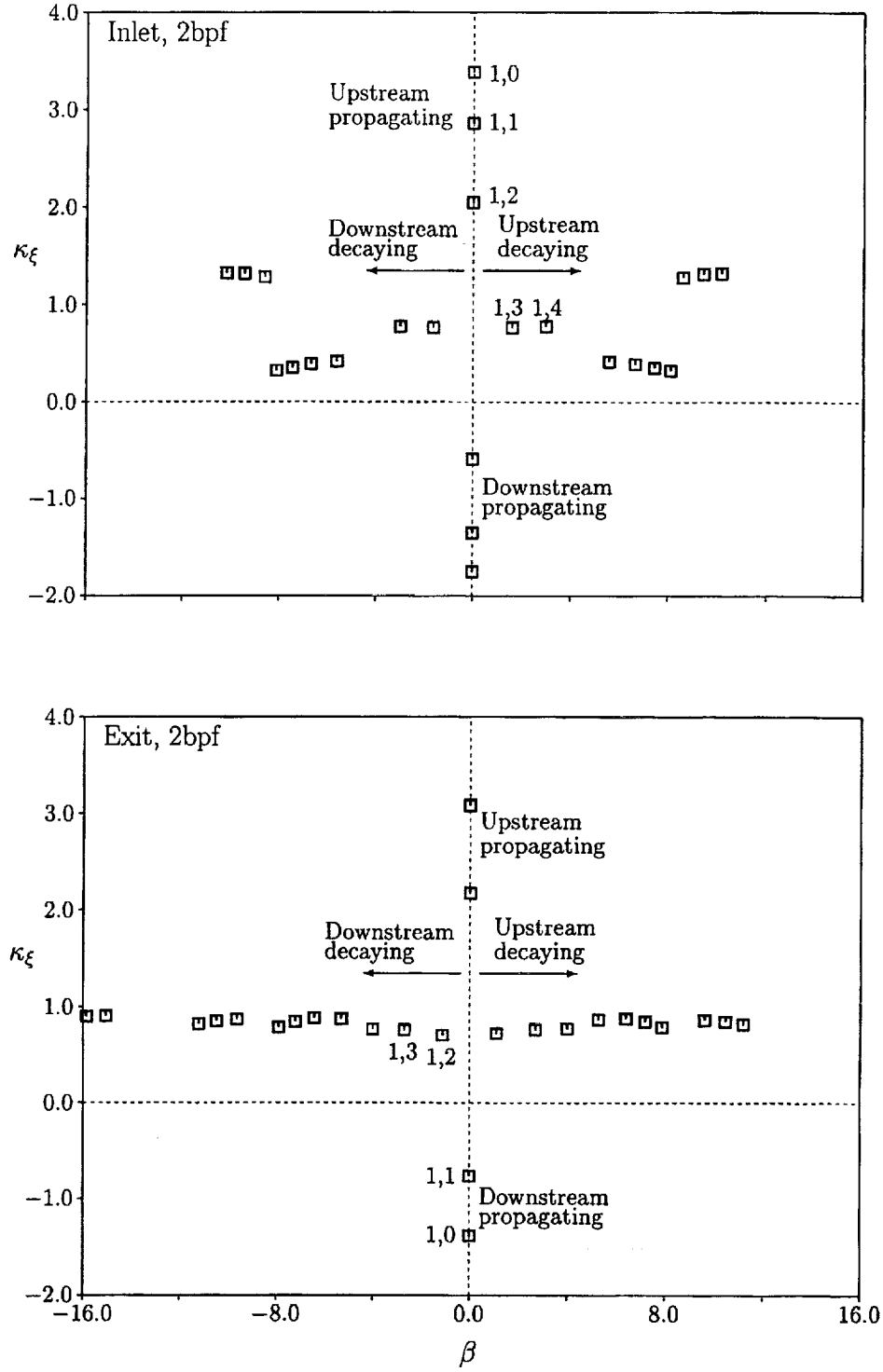

Figure 18: Axial eigenvalues, $\chi = \beta + i\kappa_\xi$, of acoustic disturbances far upstream and far downstream of the FEGV operating at the low power (approach) setting and subjected to an unsteady excitation at 2 BPF ($\omega = 7.406$ and $\sigma = -288.0$ deg).

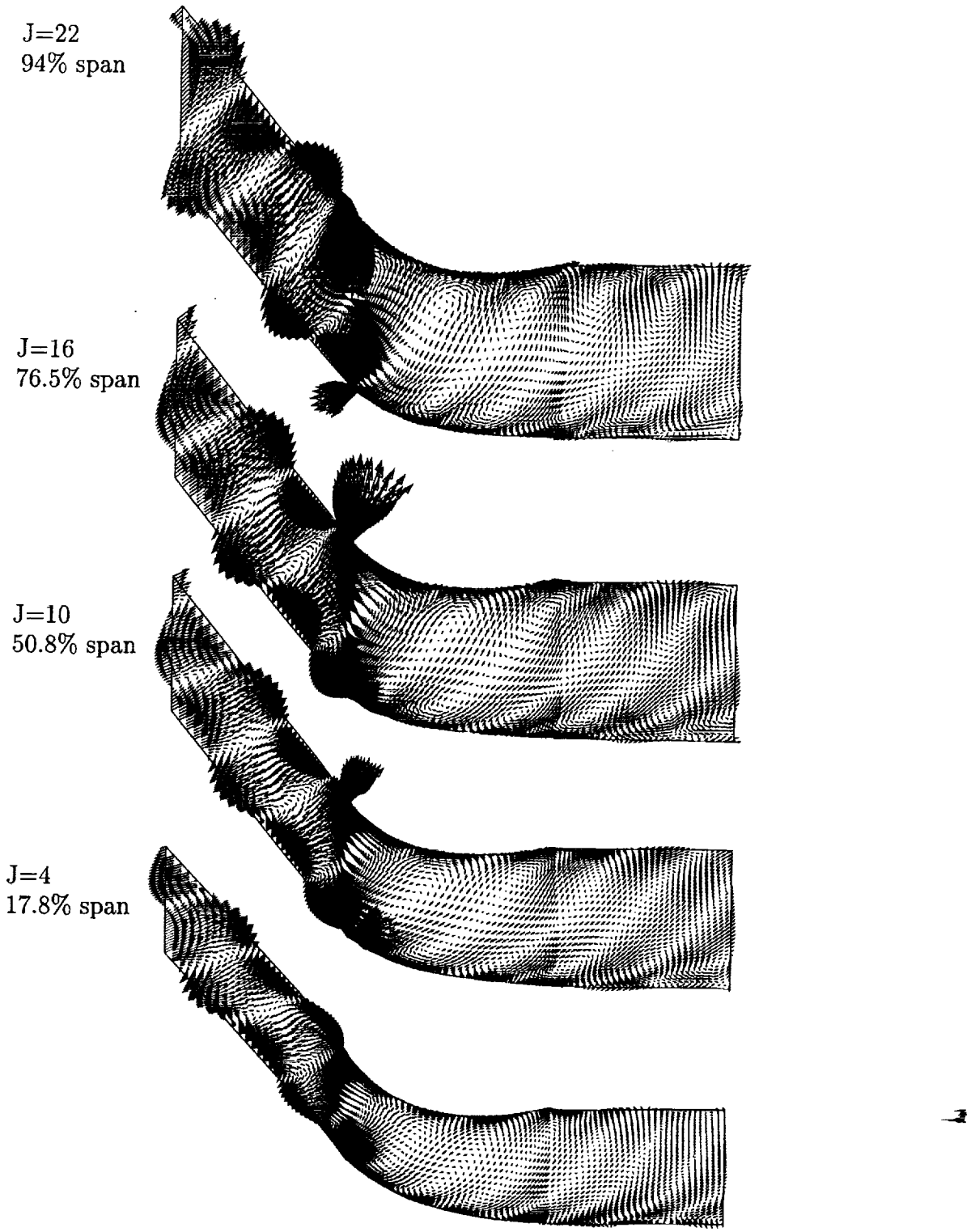

Figure 19: Imaginary component of unsteady velocity field at four radial stations (scale factor = 30) for the FEGV operating at the low power setting and subjected to the 2 BPF wake excitation.

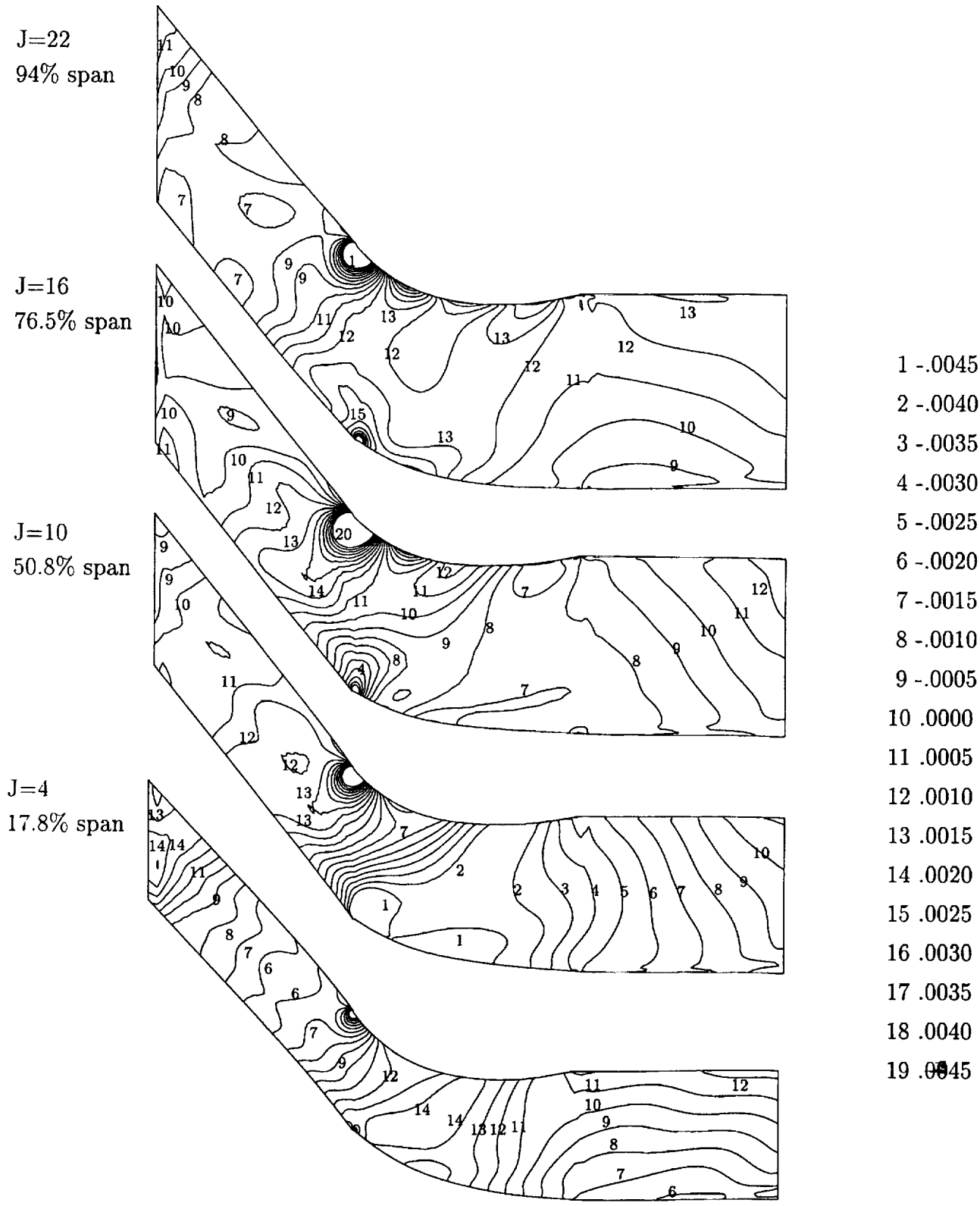

Figure 20: Imaginary component of unsteady pressure field at four radial stations for the FEGV operating at the low power setting and subjected to the 2 BPF wake excitation.

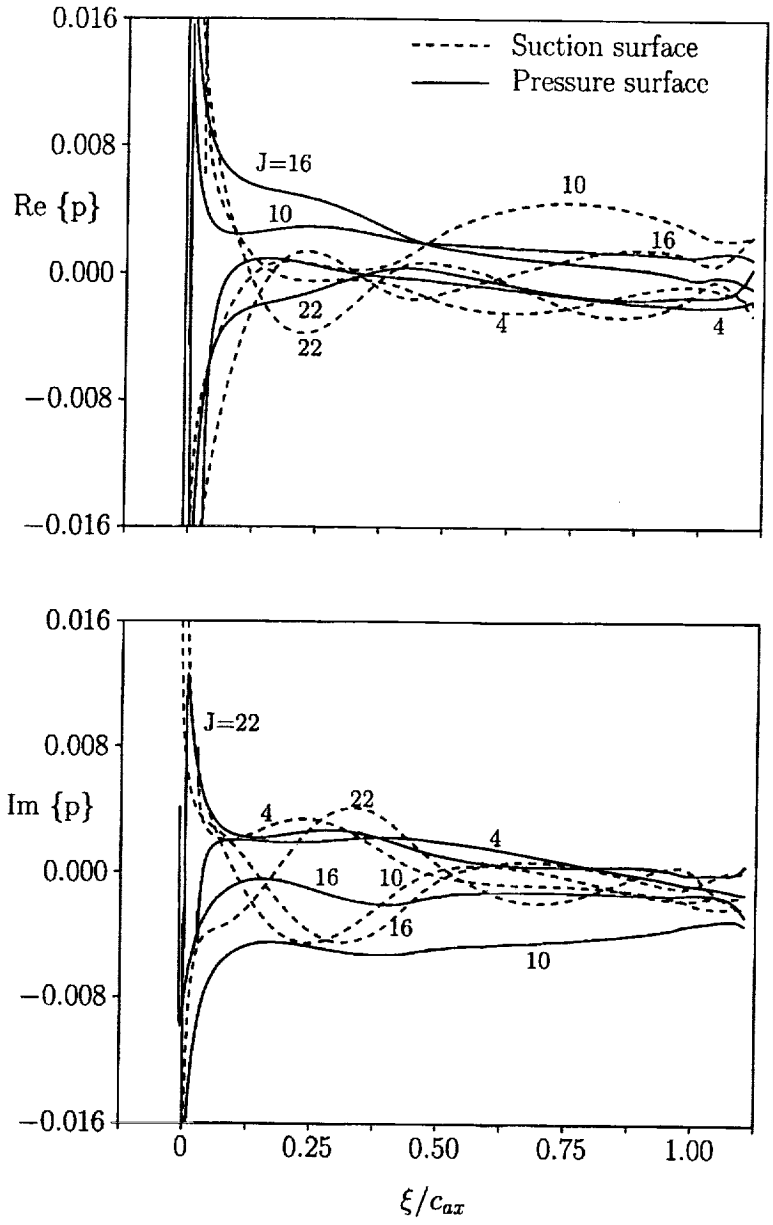

Figure 21: Unsteady surface-pressure distributions at four radial stations for the FEGV operating at the low power setting and subjected to the 2 BPF wake excitation.

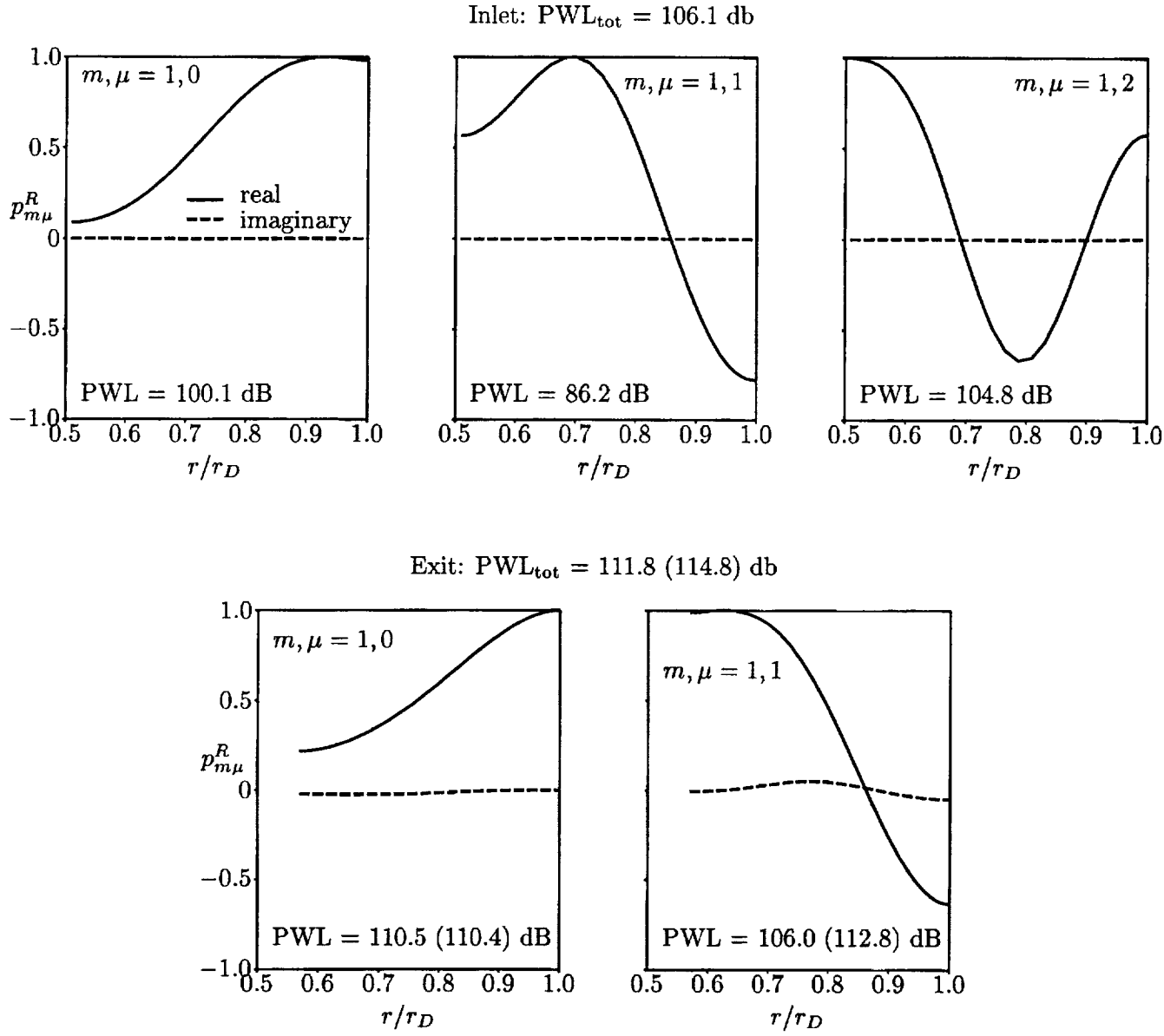

Figure 22: Radial pressure modes and modal and total sound power levels of the propagating acoustic responses in the far field of the FEGV operating at the low power (approach) setting and subjected to the 2 BPF ($\omega = 7.406$ and $\sigma = -288.0$ deg) wake excitation.

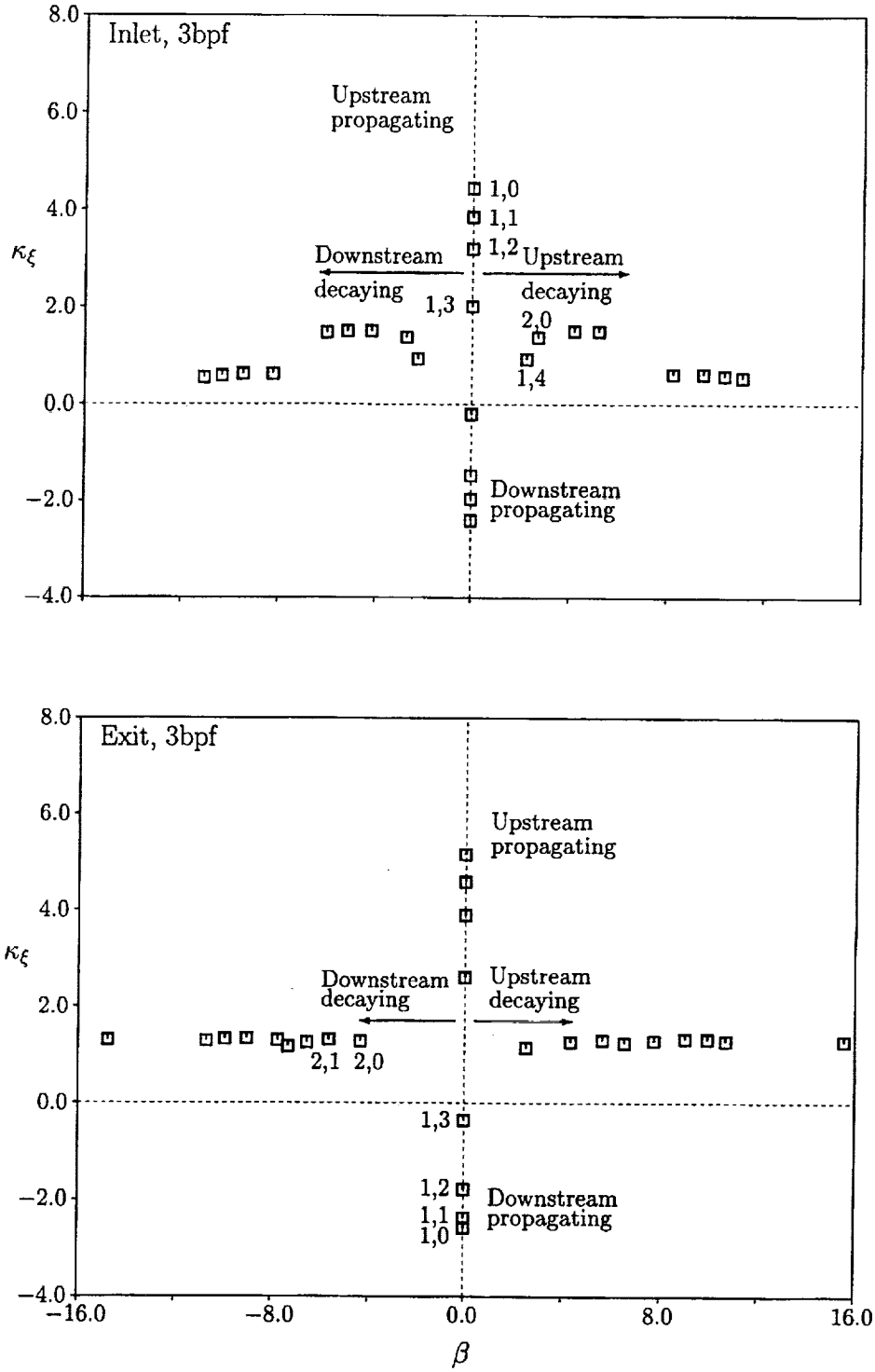

Figure 23: Axial eigenvalues, $\chi = \beta + i\kappa_\xi$, of acoustic disturbances far upstream and far downstream of the FEGV operating at the low power (approach) setting and subjected to an unsteady excitation at 3 BPF ($\omega = 11.109$ and $\sigma = -432.0$ deg).

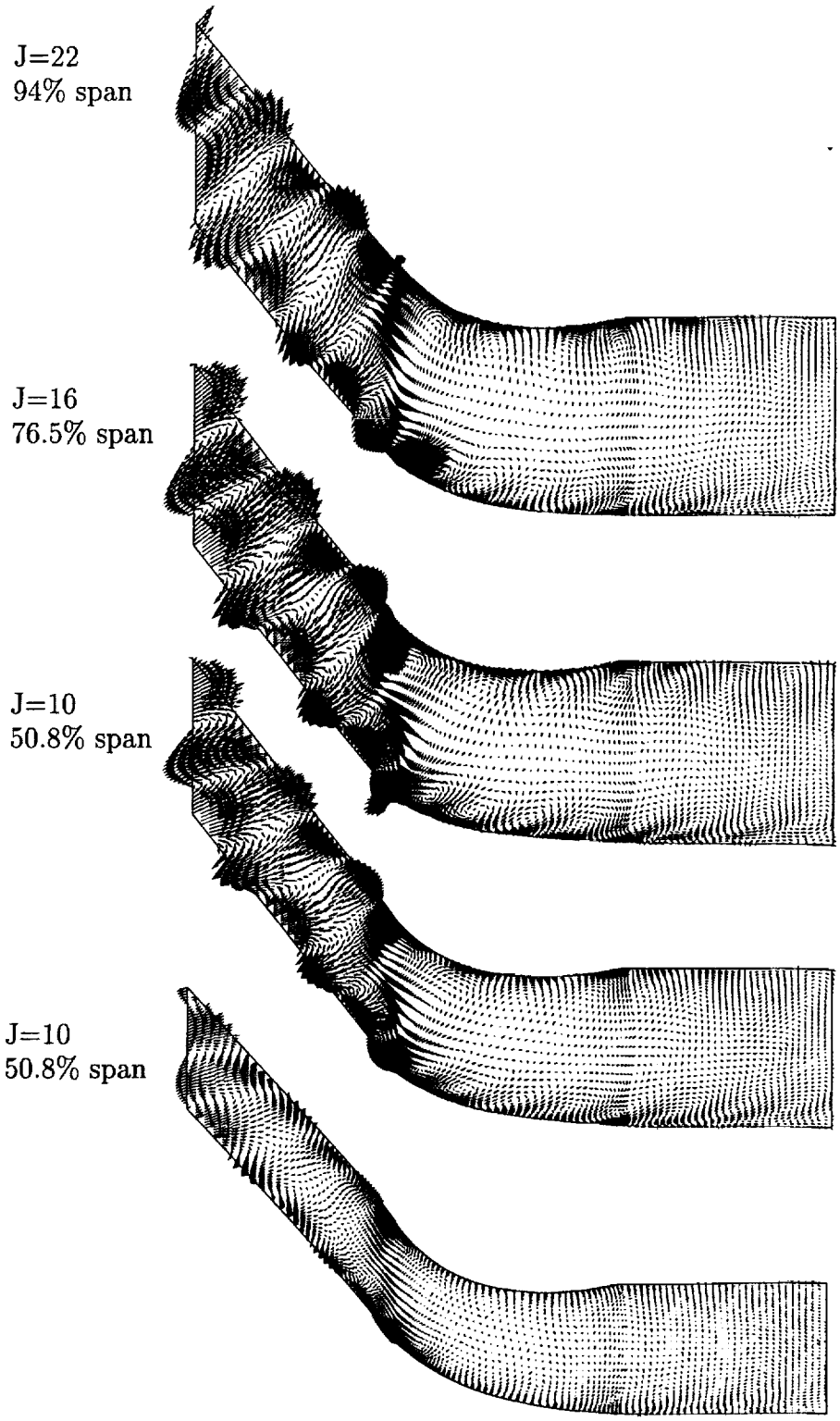

Figure 24: Imaginary component of the unsteady velocity at four radial stations (scale factor = 75) for the FEGV operating at the low power setting and subjected to the 3 BPF wake excitation.

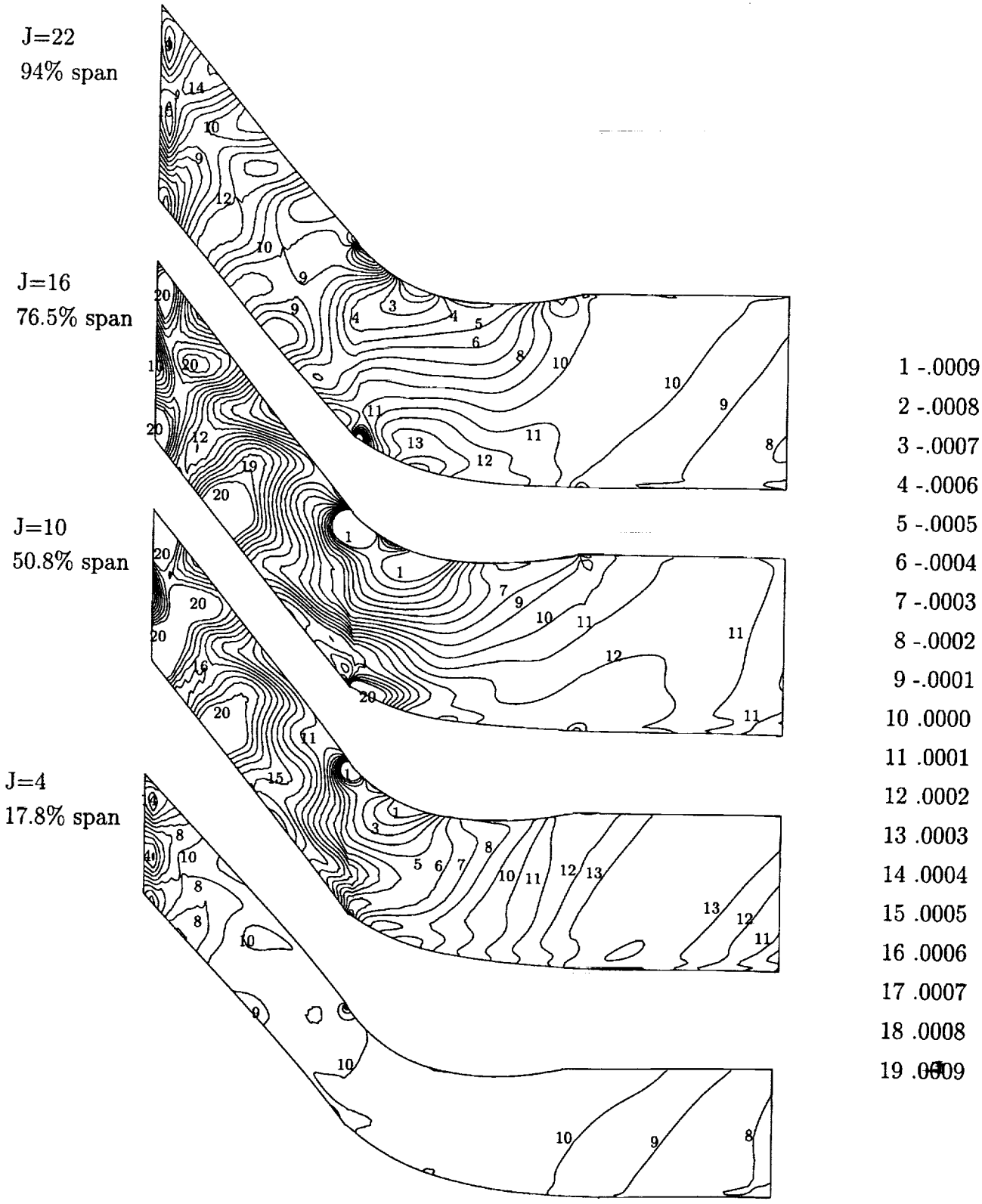

Figure 25: Imaginary component of the unsteady pressure at four radial stations for the FEGV operating at the low power setting and subjected to the 3 BPF wake excitation.

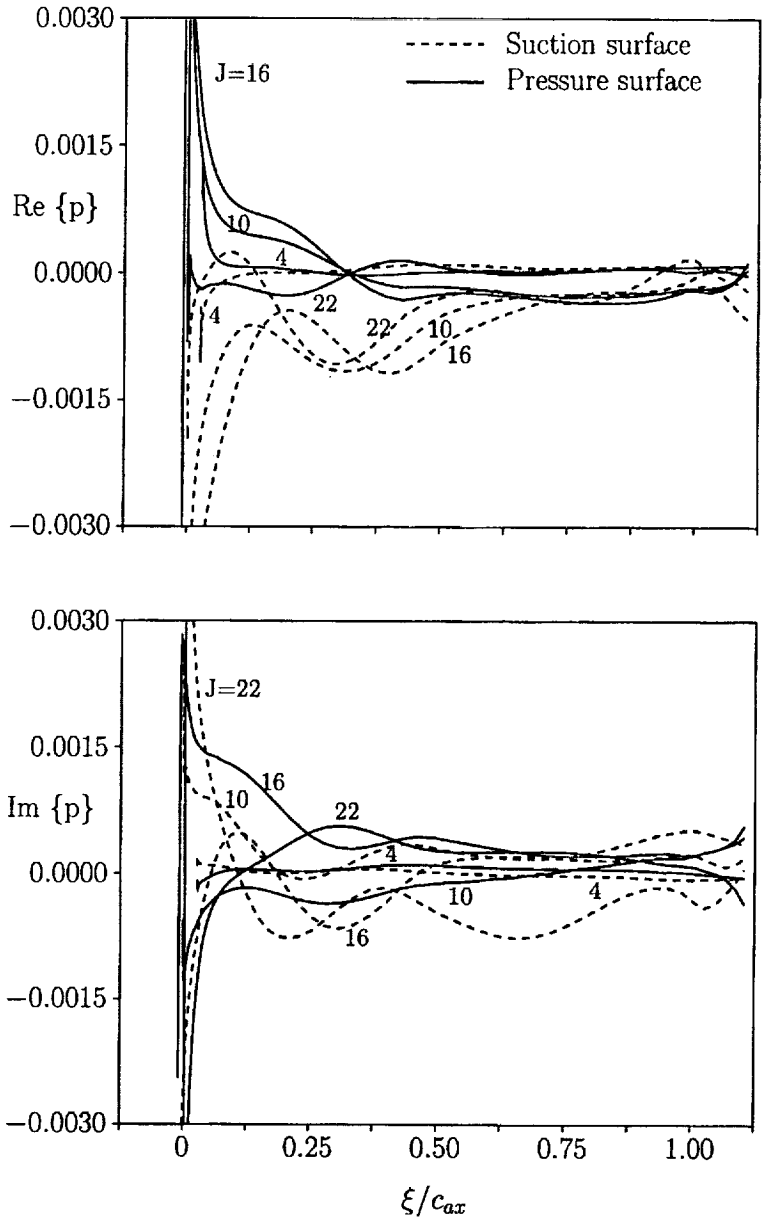

Figure 26: Unsteady surface-pressure distributions at four radial stations for the FEGV operating at the low power setting and subjected to the 3 BPF wake excitation.

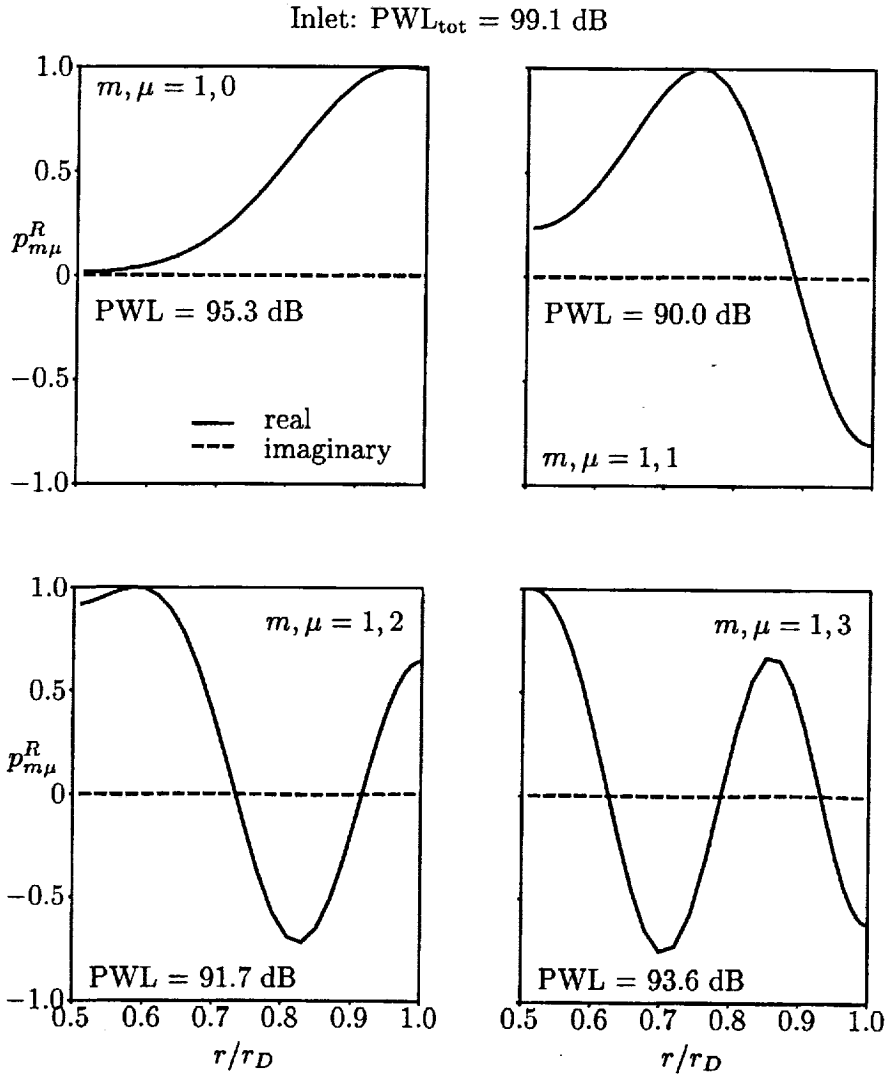

Figure 27: Radial pressure modes and modal and total sound power levels for the propagating acoustic responses far upstream of the FEGV operating at the low power (approach) setting and subjected to the 3 BPF ($\omega = 11.109$ and $\sigma = -432.0$ deg) wake excitation.

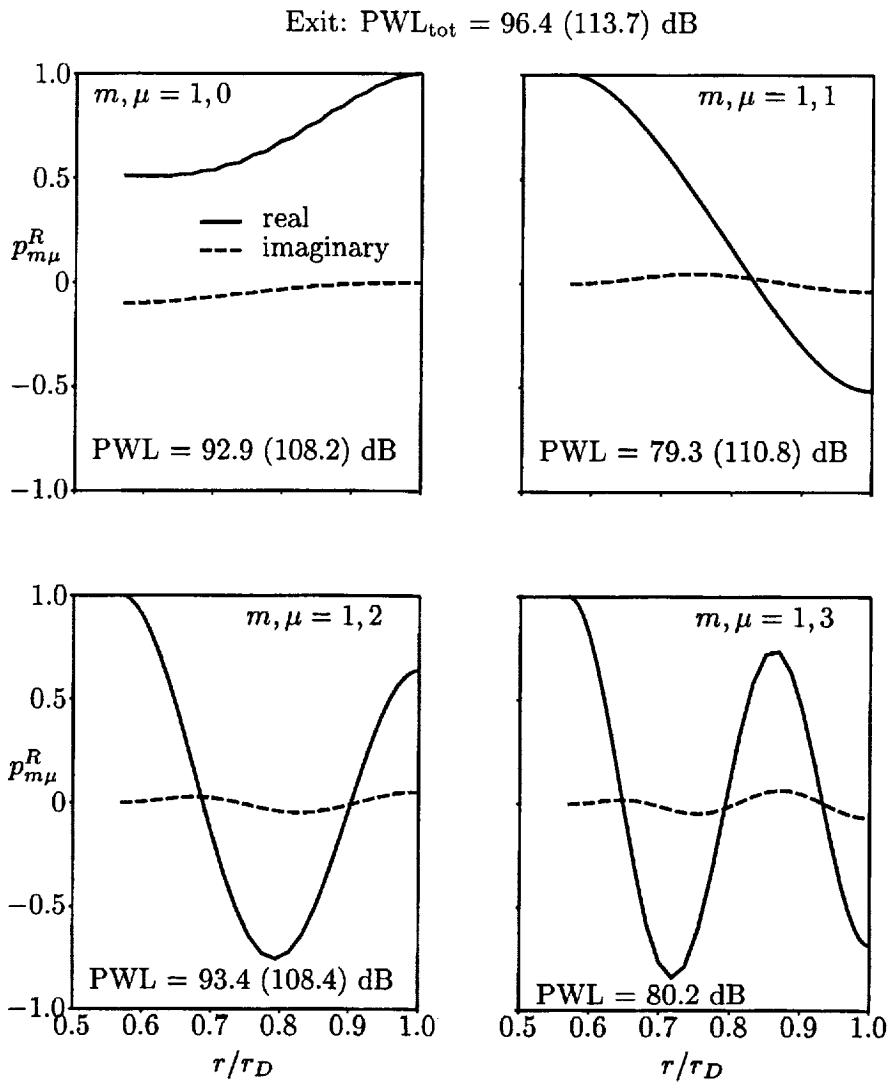

Figure 28: Radial pressure modes and modal and total sound power levels for the propagating acoustic responses far downstream of FEGV operating at the low power (approach) setting and subjected to the 3 BPF ($\omega = 11.109$ and $\sigma = -432.0$ deg) wake excitation.

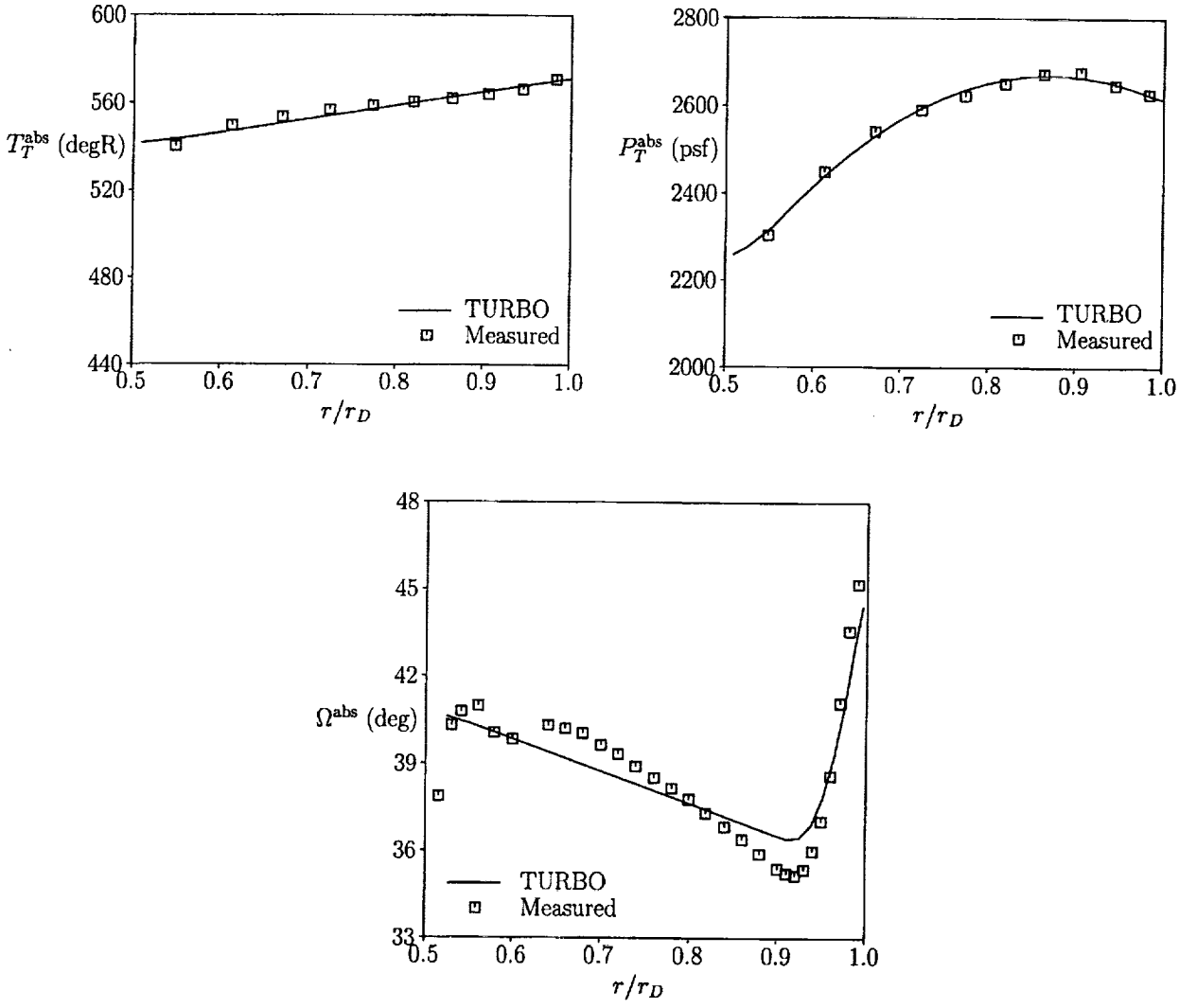

Figure 29: Steady flow properties far upstream of the FEGV operating at the high power (take-off) setting.

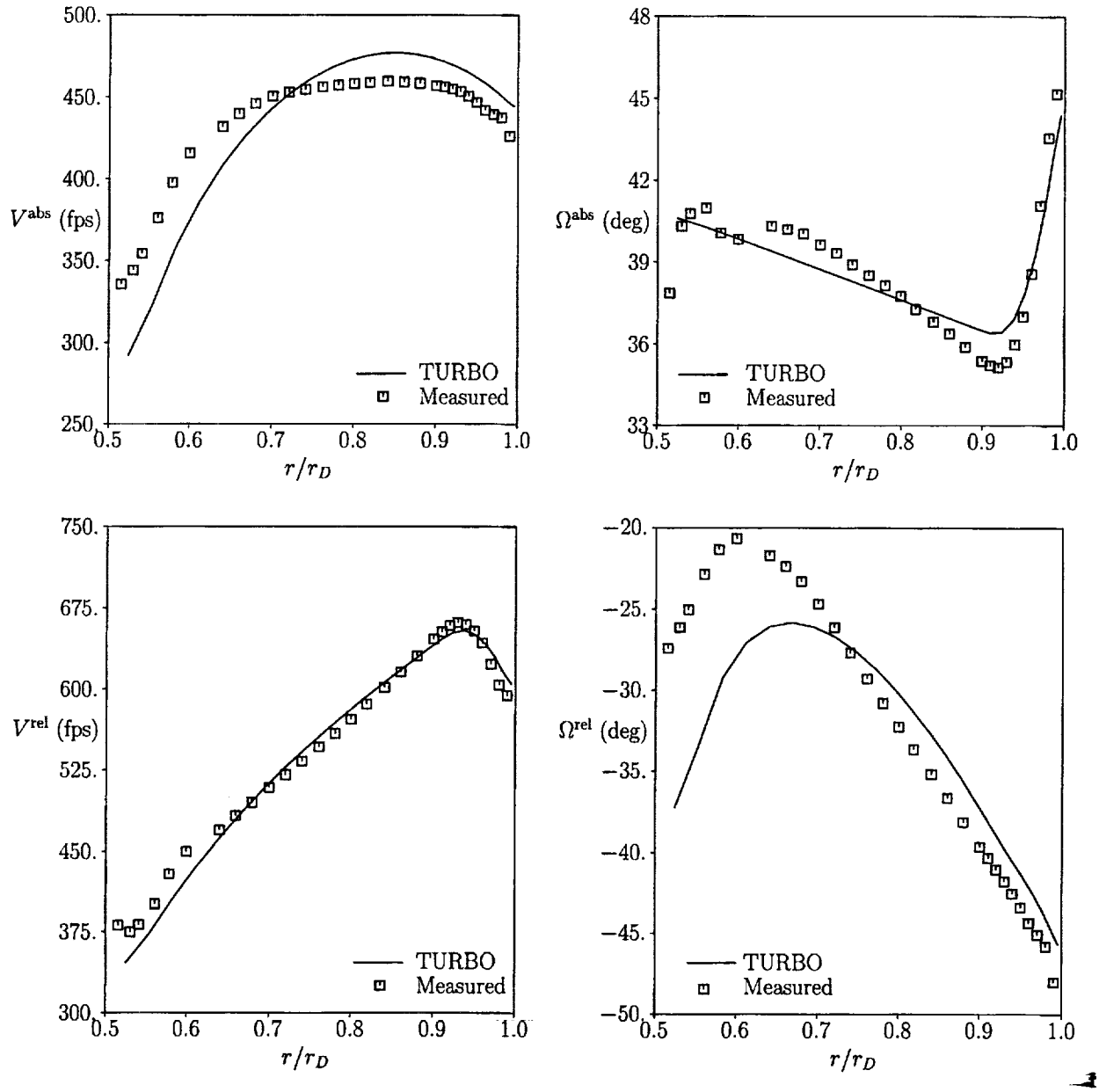

Figure 30: Absolute and relative steady velocities at the rotor exit (FEGV inlet) for the high power setting.

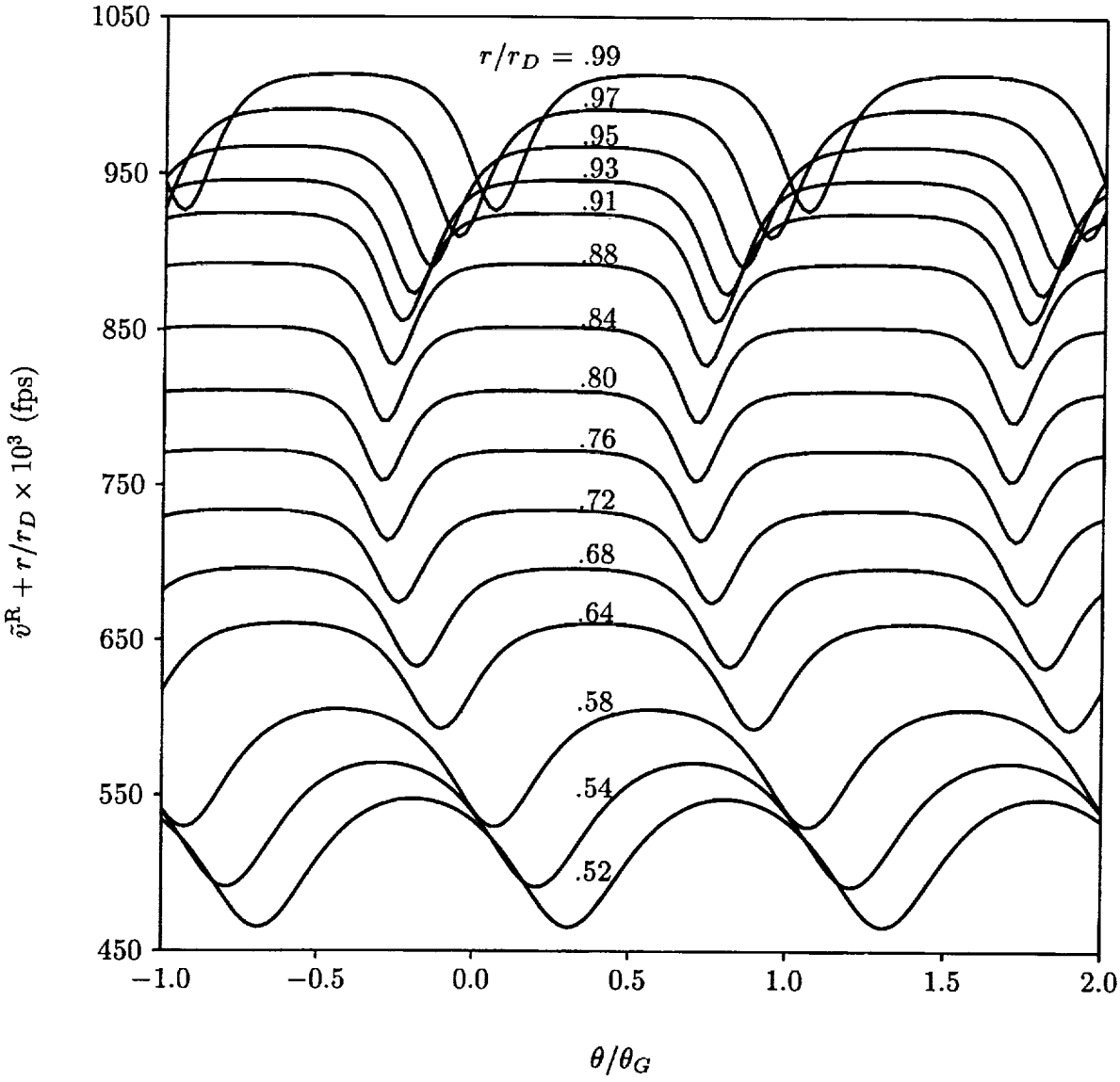

Figure 31: Analytic, rotor-wake, tangential velocity perturbation at the FEGV midspan leading-edge plane ($\xi = 0$) for the high power (take-off) setting.

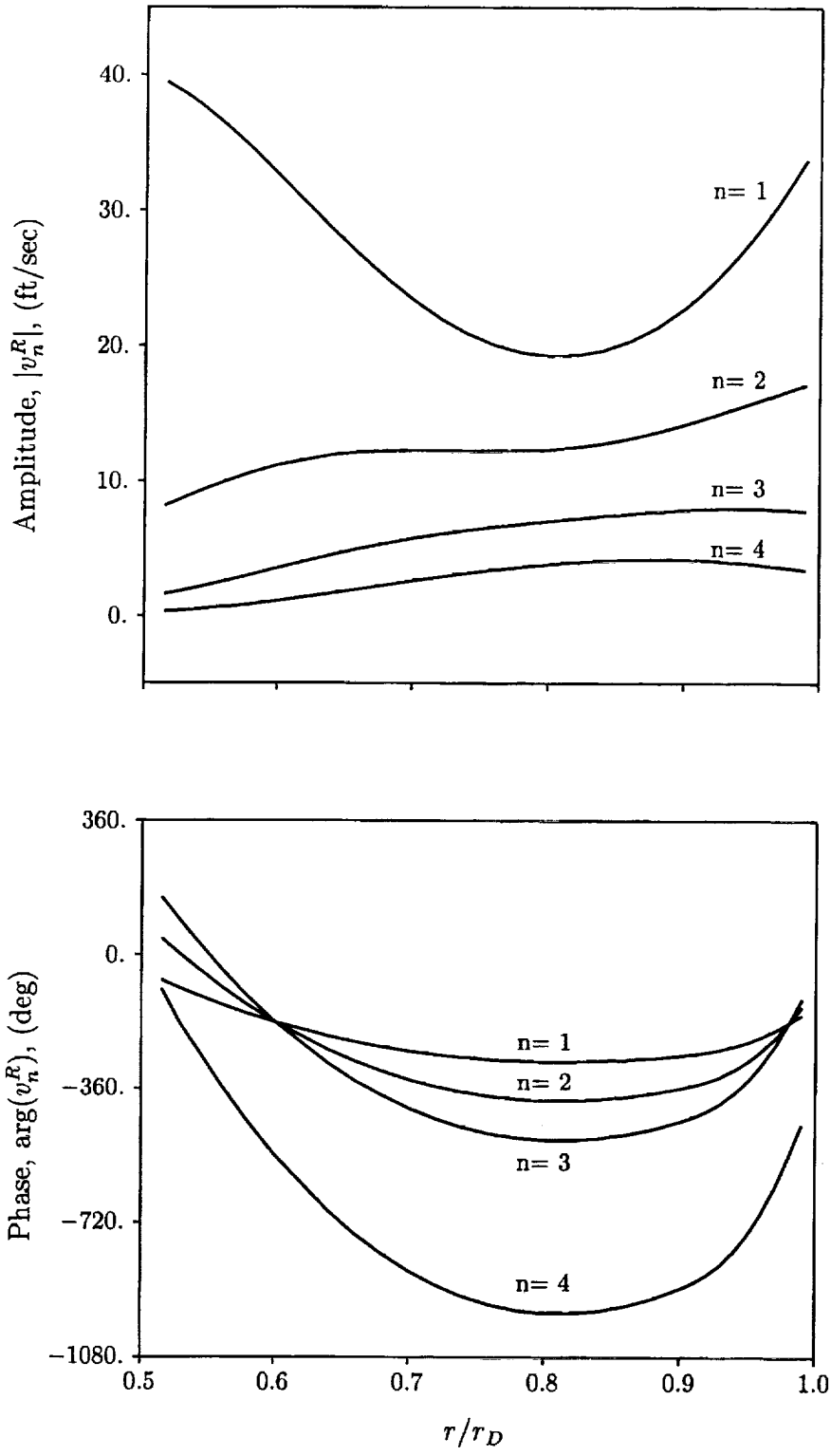

Figure 32: Fourier components of the analytic, rotor-wake excitation velocity, $\tilde{v}^{\mathrm{R}}$, for the high power setting.

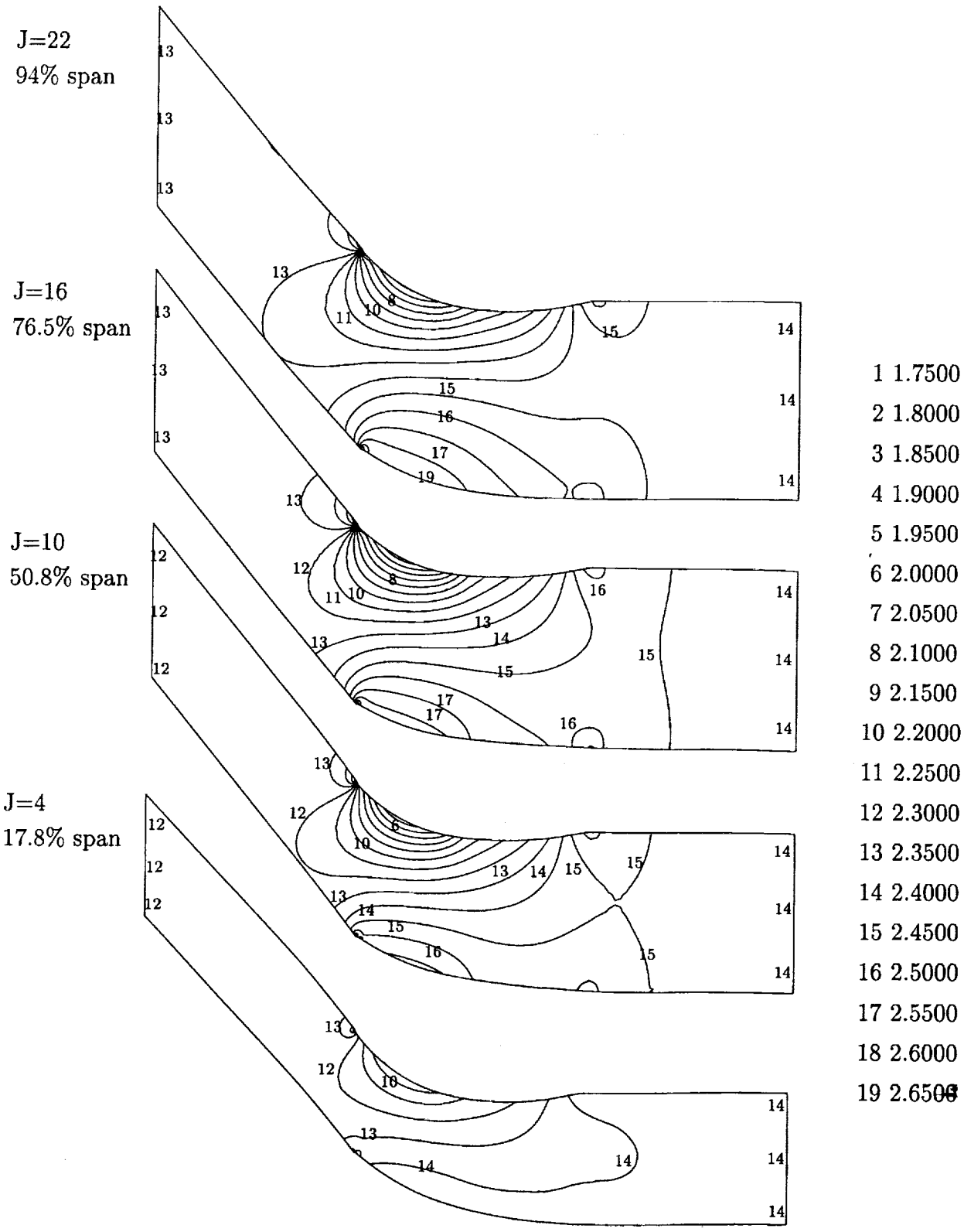

Figure 33: Steady pressure field at four radial stations for the FEGV operating at the high power setting.

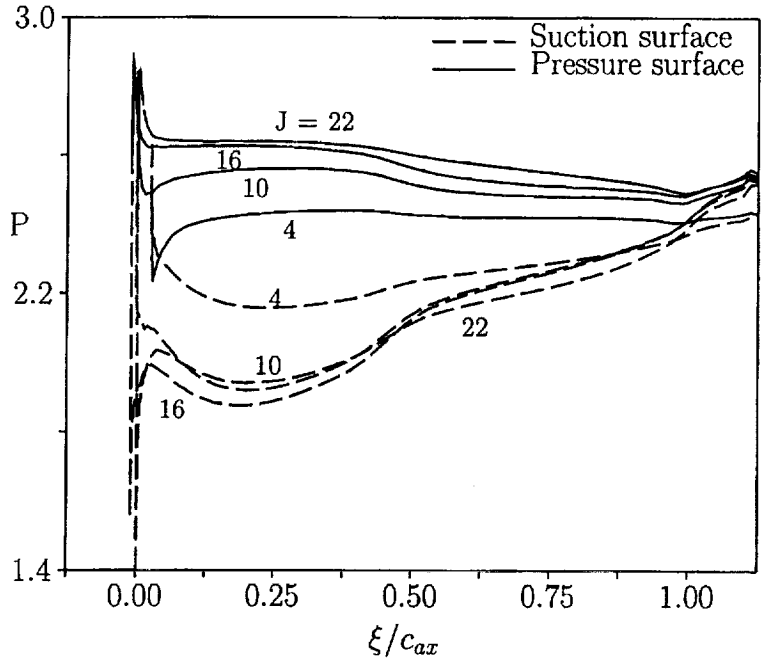

Figure 34: Steady surface-pressure distributions at four radial stations for the FEGV operating at the high power setting.

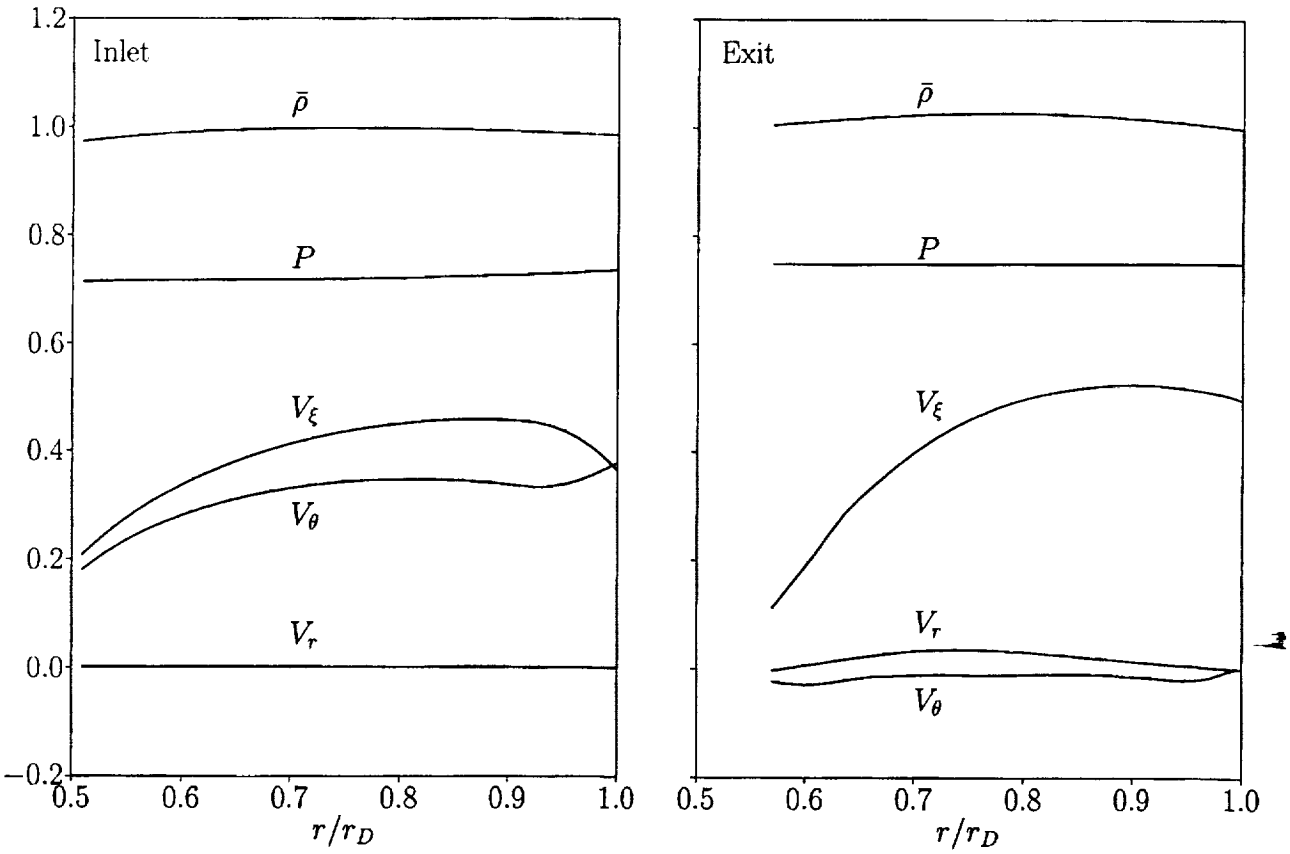

Figure 35: Steady flow properties at the computational inlet and exit planes of the FEGV operating at the high power setting.

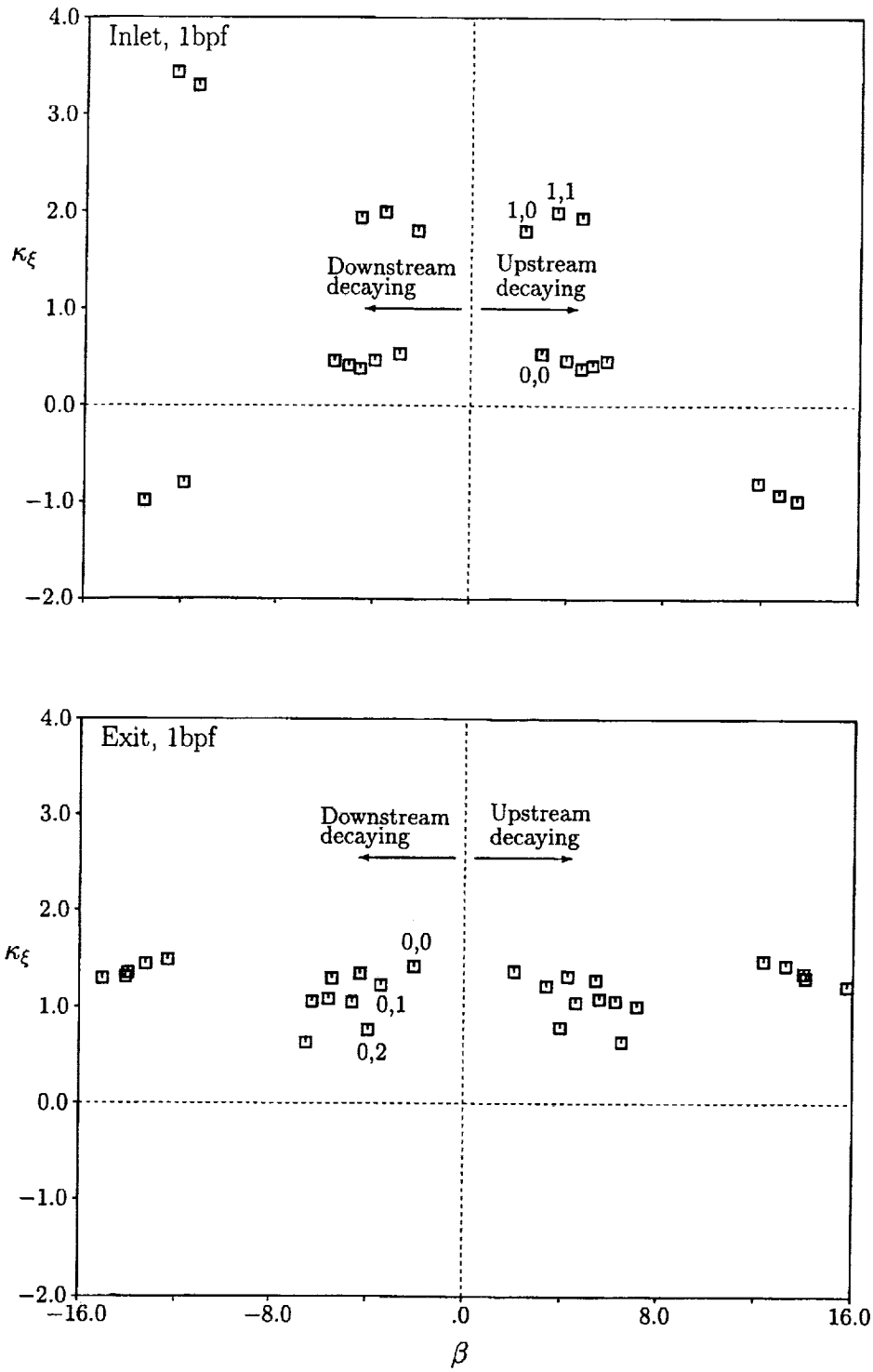

Figure 36: Axial eigenvalues, $\chi = \beta + i\kappa_\xi$, of acoustic disturbances far upstream and far downstream of the FEGV operating at the high power (take-off) setting and subjected to an unsteady excitation at 1 BPF ($\omega = 3.677$ and $\sigma = -144.0$ deg).

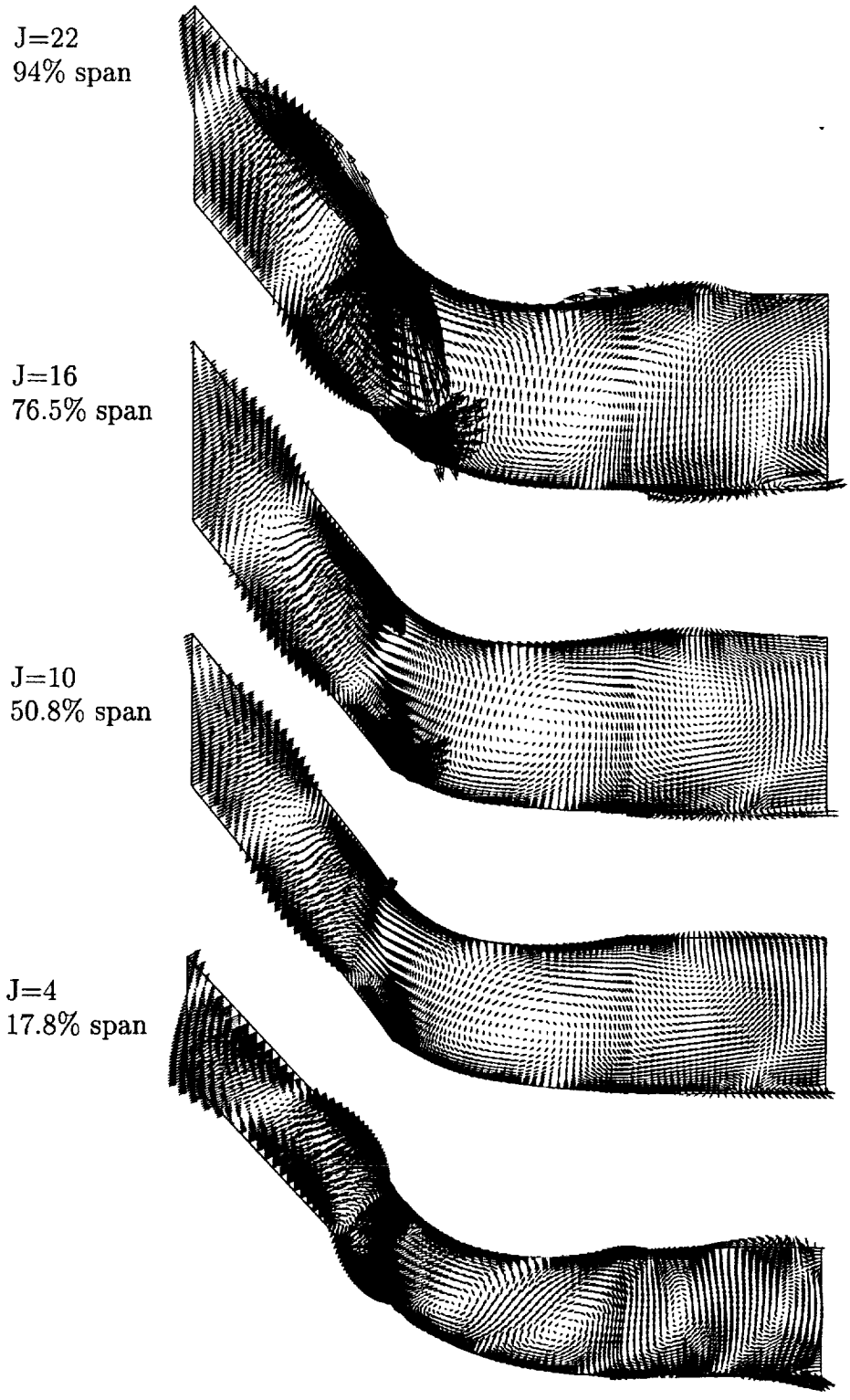

Figure 37: Imaginary component of the unsteady velocity at four radial stations (scale factor = 10) for the FEGV operating at the high power setting and subjected to the 1 BPF wake excitation.

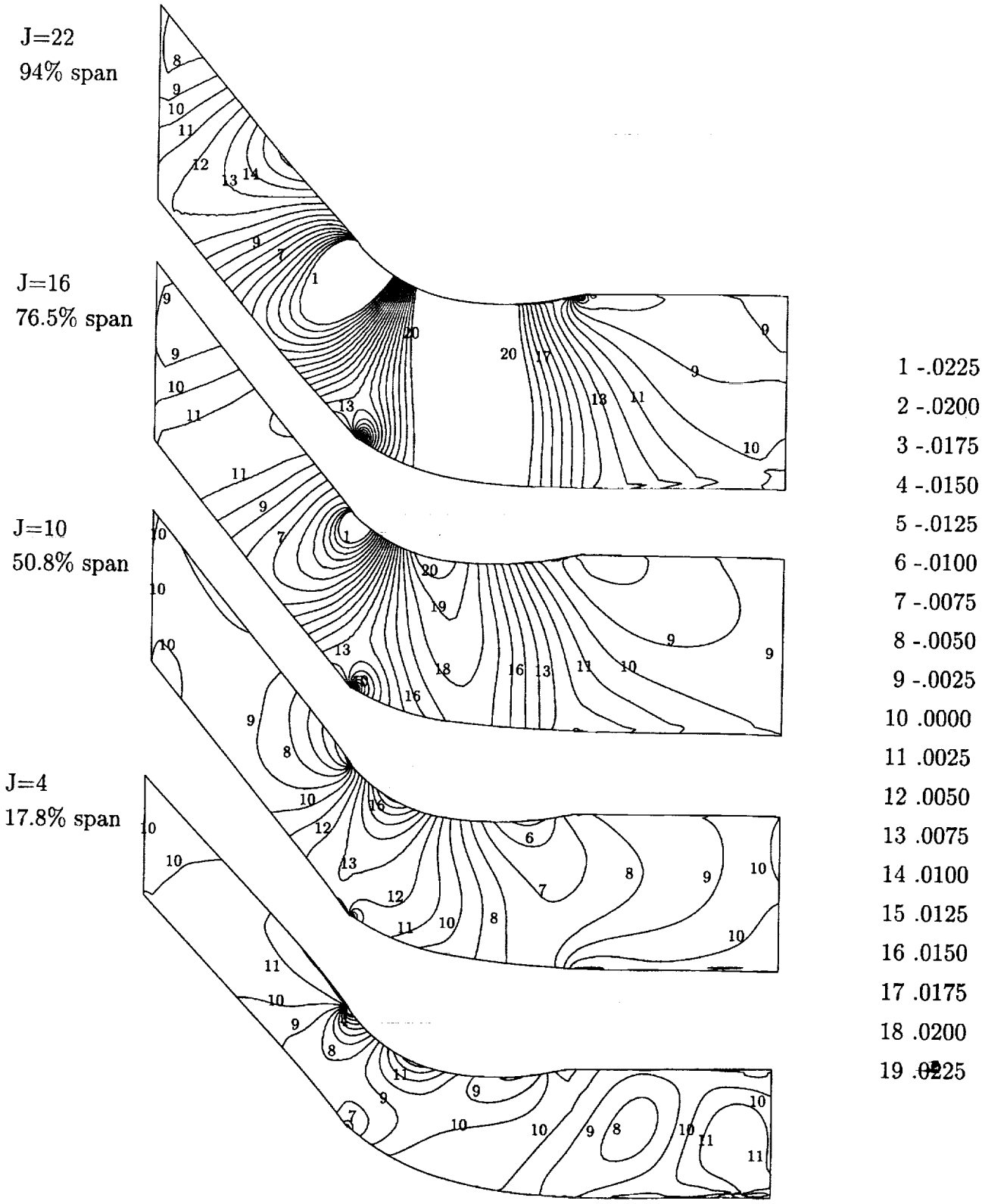

Figure 38: Imaginary component of the unsteady pressure at four radial stations for the FEGV operating at the high power setting and subjected to the 1 BPF wake excitation.

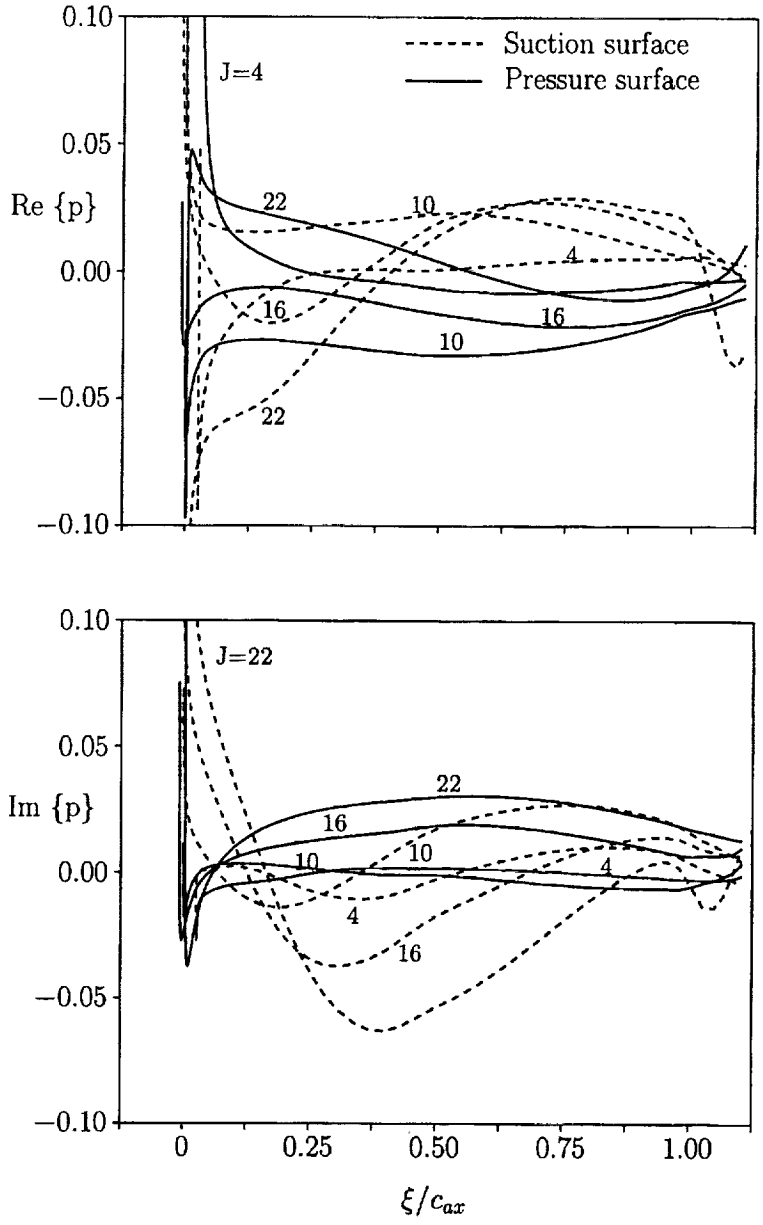

Figure 39: Unsteady surface-pressure distributions at four radial stations for the FEGV operating at the high power setting and subjected to the 1 BPF wake excitation.

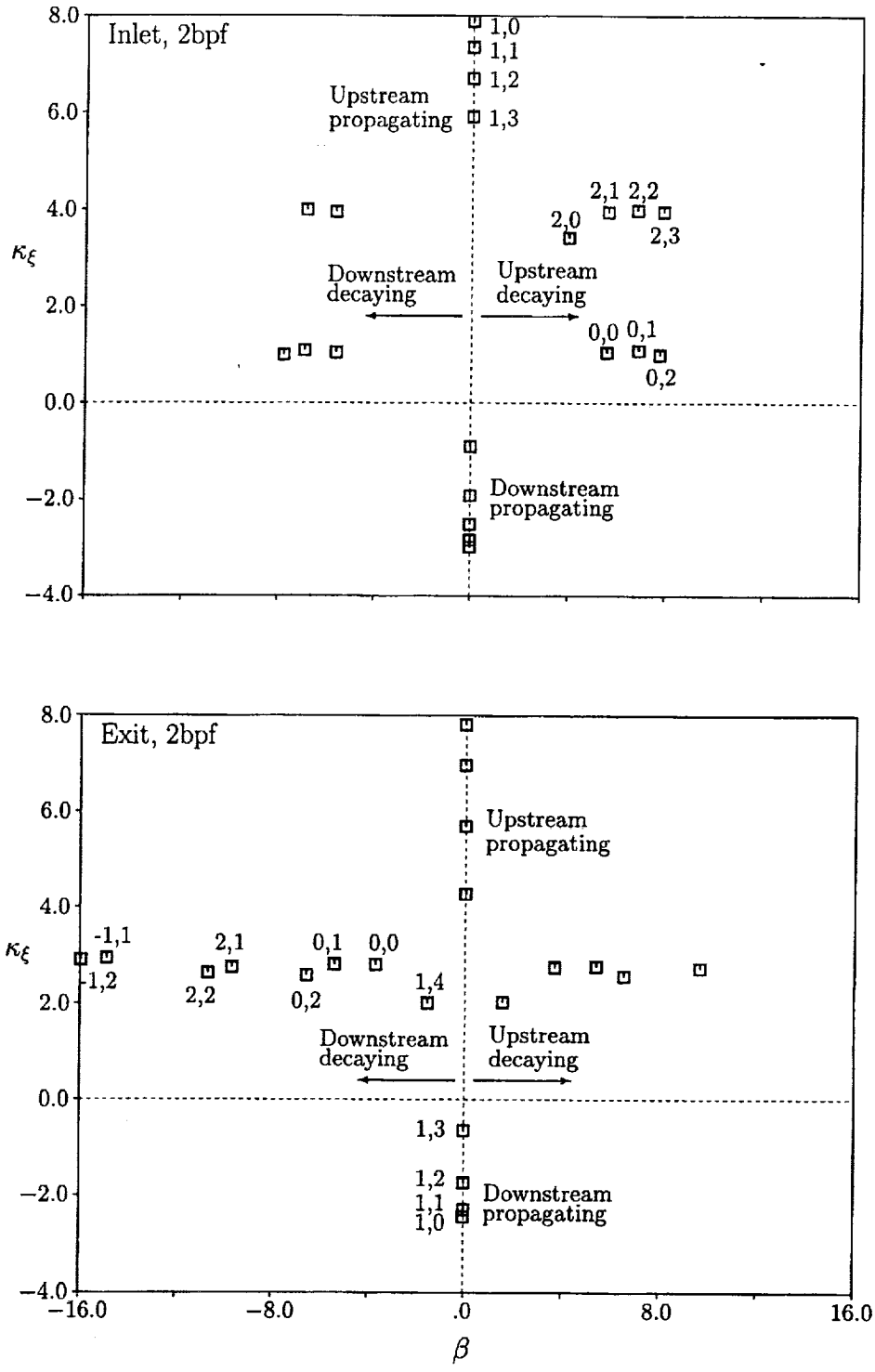

Figure 40: Axial eigenvalues, $\chi = \beta + i\kappa_\xi$, of acoustic disturbances far upstream and far downstream of the FEGV operating at the high power (take-off) setting and subjected to an unsteady excitation at 2 BPF ($\omega = 7.355$ and $\sigma = -288.0$ deg).

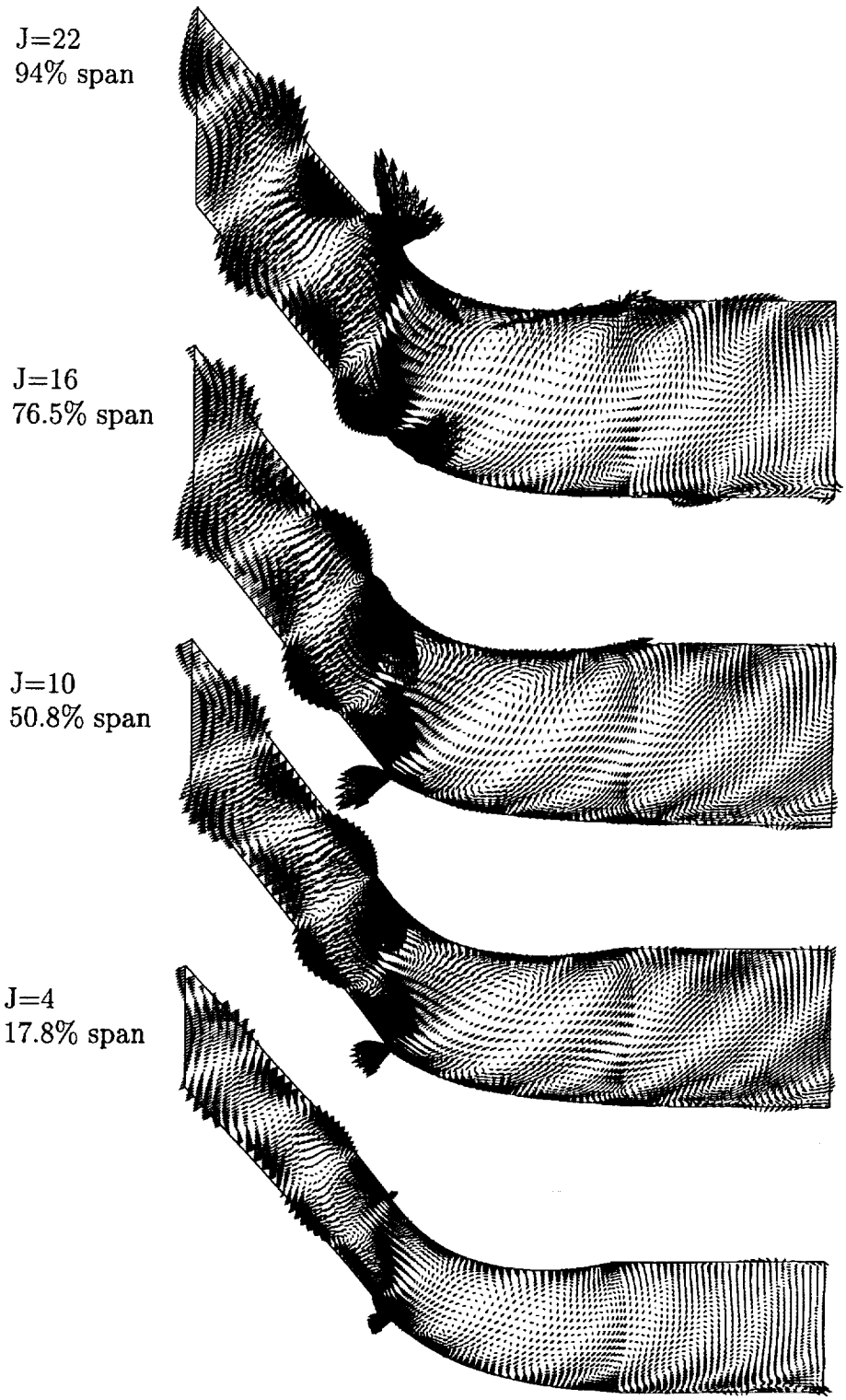

Figure 41: Imaginary component of the unsteady velocity at four radial stations (scale factor = 25) for the FEGV operating at the high power setting and subjected to the 2 BPF wake excitation.

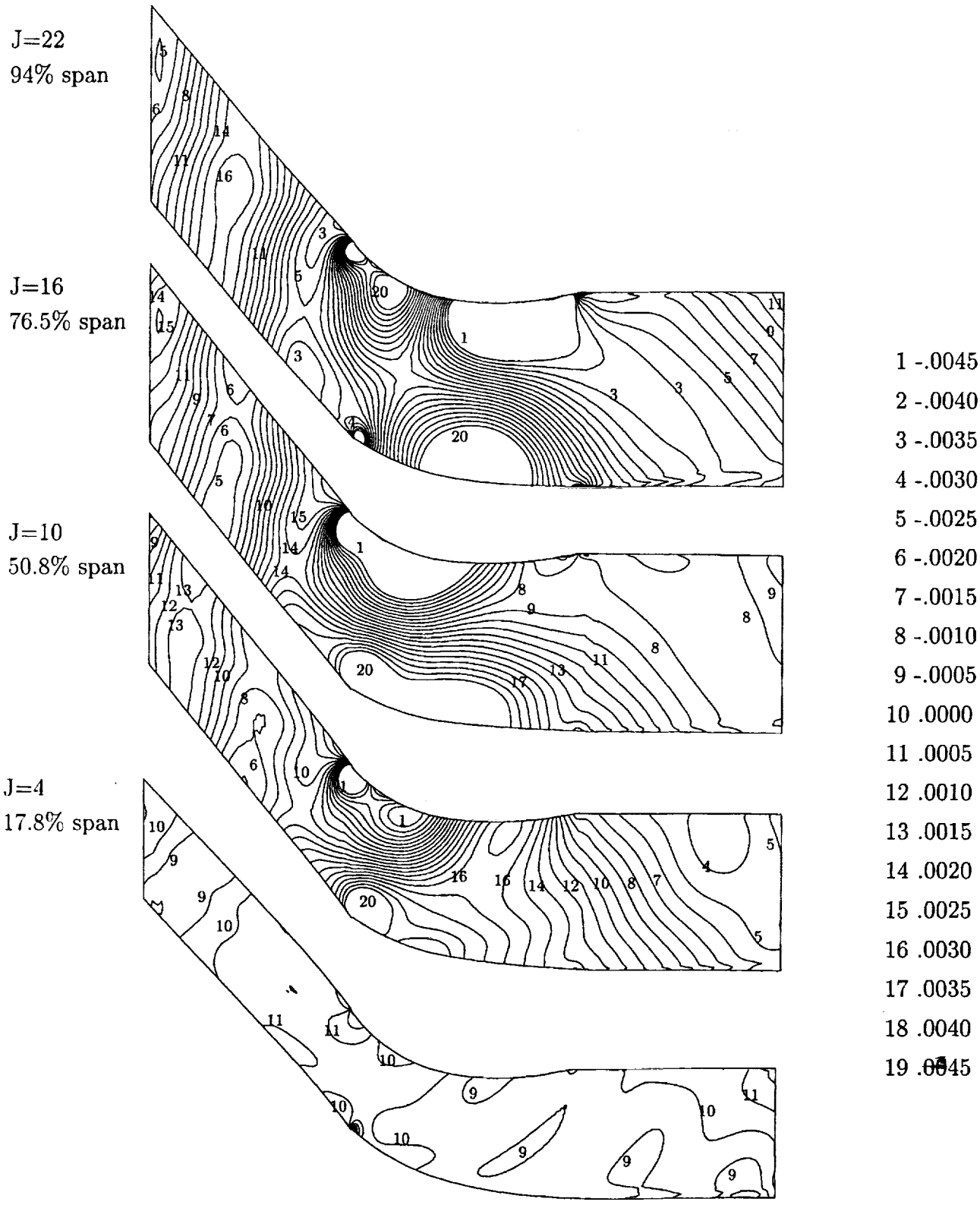

Figure 42: Imaginary component of the unsteady pressure at four radial stations for the FEGV operating at the high power setting and subjected to the 2 BPF wake excitation.

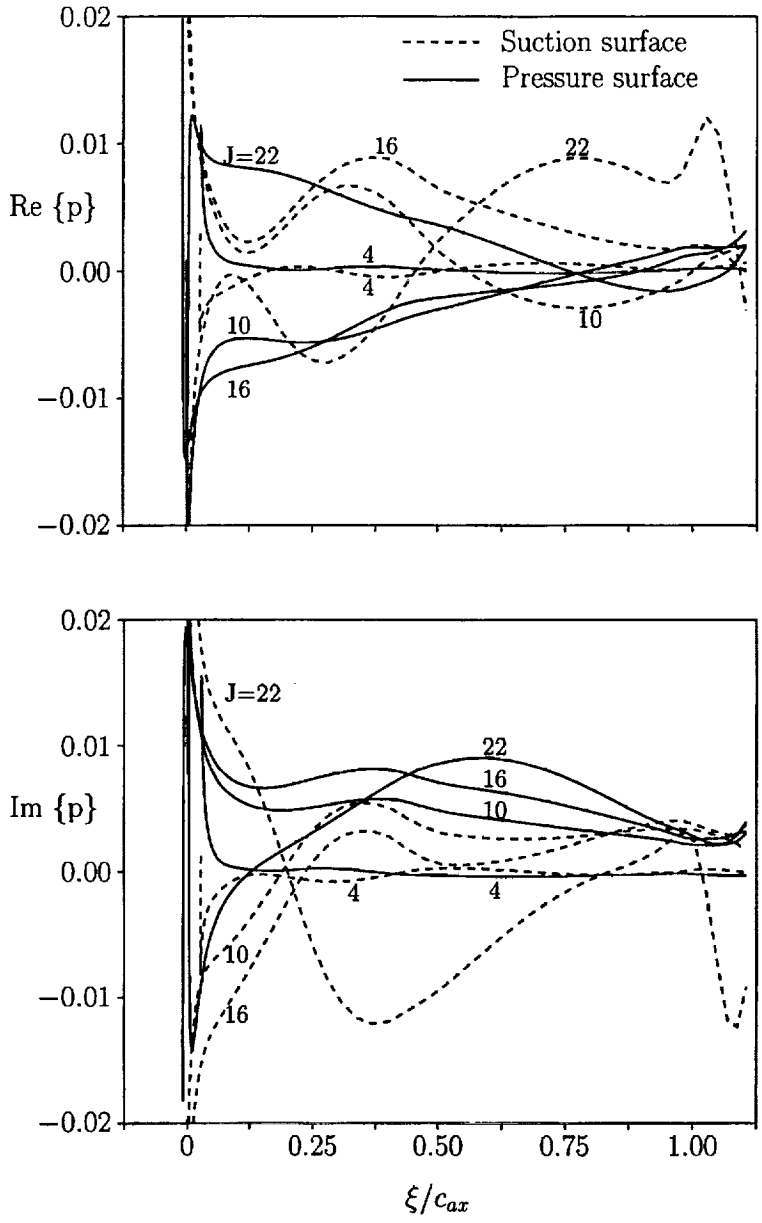

Figure 43: Unsteady surface-pressure distributions at four radial stations for the FEGV operating at the high power setting and subjected to the 2 BPF wake excitation.

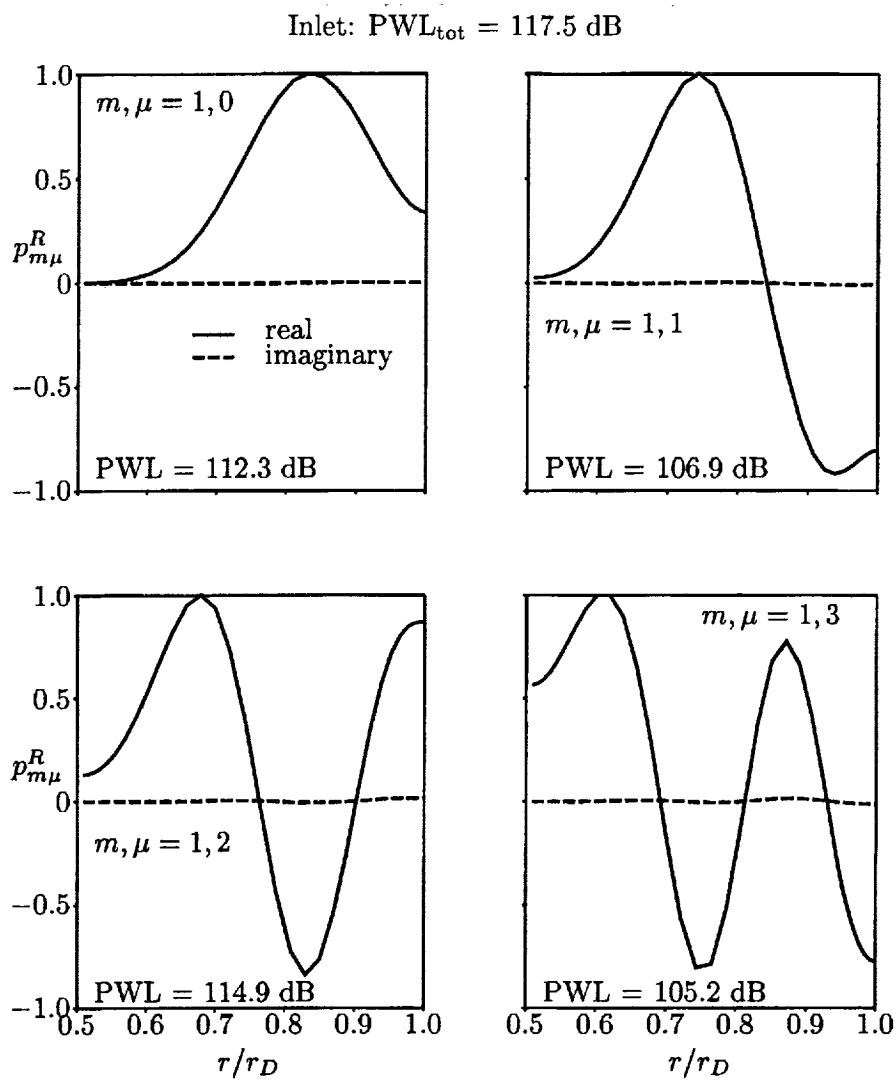

Figure 44: Radial pressure modes and modal and total sound power levels for the propagating acoustic responses far upstream of the FEGV operating at the high power (take-off) setting and subjected to the 2 BPF ($\omega = 7.355$ and $\sigma = -288.0$ deg) wake excitation.

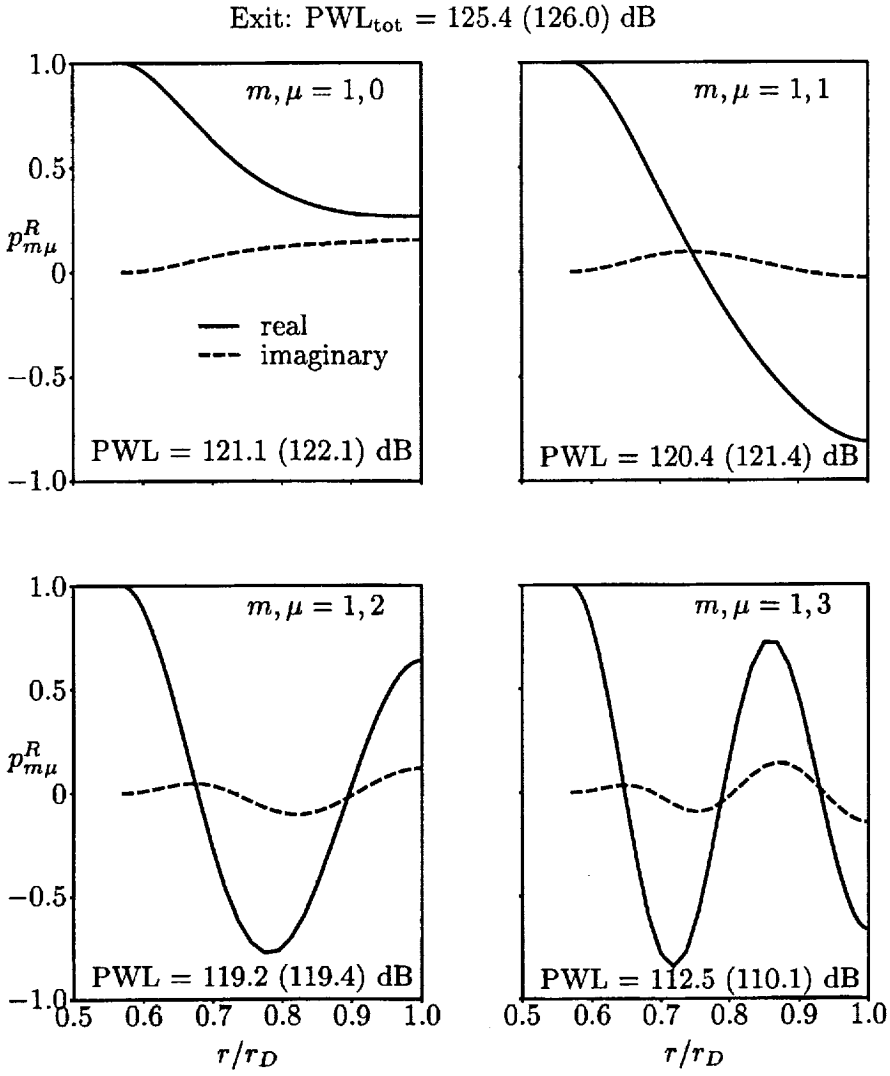

Figure 45: Radial pressure modes and modal and total sound power levels for the propagating acoustic responses far downstream of the FEGV operating at the high power (take-off) setting and subjected to the 2 BPF ($\omega = 7.355$ and $\sigma = -288.0$ deg) wake excitation.

REPORT DOCUMENTATION PAGE

Form Approved
OMB No. 0704-0188

1. AGENCY USE ONLY (*Leave blank*)	2. REPORT DATE	3. REPORT TYPE AND DATES COVERED
	January 2001	Final Contractor Report

4. TITLE AND SUBTITLE

Linearized Unsteady Aerodynamic Analysis of the Acoustic Response to Wake/Blade-Row Interaction

5. FUNDING NUMBERS

WU–706–81–11–00
NAS3–27727
Task Order 13, Subtask 3

6. AUTHOR(S)

Joseph M. Verdon

7. PERFORMING ORGANIZATION NAME(S) AND ADDRESS(ES)

Pratt & Whitney
400 Main Street
East Hartford, Connecticut 06108

8. PERFORMING ORGANIZATION REPORT NUMBER

E–12660

9. SPONSORING/MONITORING AGENCY NAME(S) AND ADDRESS(ES)

National Aeronautics and Space Administration
Washington, DC 20546–0001

10. SPONSORING/MONITORING AGENCY REPORT NUMBER

NASA CR—2001-210713

11. SUPPLEMENTARY NOTES

Project Manager, Dennis L. Huff, Structures and Acoustics Division, NASA Glenn Research Center, organization code 5940, 216–433–3913.

12a. DISTRIBUTION/AVAILABILITY STATEMENT

Unclassified - Unlimited
Subject Category: 71 Distribution: Nonstandard

Available electronically at http://gltrs.grc.nasa.gov/GLTRS

This publication is available from the NASA Center for AeroSpace Information, 301–621–0390.

12b. DISTRIBUTION CODE

13. ABSTRACT ***(Maximum 200 words)***

The three-dimensional, linearized Euler analysis, LINFLUX, is being developed to provide a comprehensive and efficient unsteady aerodynamic scheme for predicting the aeroacoustic and aeroelastic responses of axial-flow turbomachinery blading. LINFLUX couples a near-field, implicit, wave-split, finite-volume solution to far-field acoustic eigensolutions, to predict the aerodynamic responses of a blade row to prescribed structural and aerodynamic excitations. It is applied herein to predict the acoustic responses of a fan exit guide vane (FEGV) to rotor wake excitations. The intent is to demonstrate and assess the LINFLUX analysis via application to realistic wake/blade-row interactions. Numerical results are given for the unsteady pressure responses of the FEGV, including the modal pressure responses at inlet and exit. In addition, predictions for the modal and total acoustic power levels at the FEGV exit are compared with measurements. The present results indicate that the LINFLUX analysis should be useful in the aeroacoustic design process, and for understanding the three-dimensional flow physics relevant to blade-row noise generation and propagation.

14. SUBJECT TERMS

Acoustics; Unsteady aerodynamics; Fan noise; Rotor-stator interaction; Euler analysis

15. NUMBER OF PAGES

94

16. PRICE CODE

A05

17. SECURITY CLASSIFICATION OF REPORT	18. SECURITY CLASSIFICATION OF THIS PAGE	19. SECURITY CLASSIFICATION OF ABSTRACT	20. LIMITATION OF ABSTRACT
Unclassified	Unclassified	Unclassified	